

DISSERTATION

Thermische Effekte im Mikromagnetismus - von ultraschnellen Schaltprozessen zu Langzeitstabilitäten

zur Erlangung des akademischen Grades

Doktor der technischen Wissenschaften

eingereicht von

Dipl.-Ing. Christoph Vogler

Matrikelnummer 0425072

Schulgasse 28, 3950 Gmünd

an der

Fakultät für Physik der Technischen Universität Wien

Betreuung:

Privatdoz. Dipl.-Ing. Dr.techn. Dieter Süss,

Institut für Festkörperphysik – E138

Diese Dissertation haben begutachtet:

(Privatdoz. Dipl.-Ing.
Dr.techn. Dieter Süss)

(Prof. Dr.
Manfred Albrecht)

Wien, 07.01.2015

(Dipl.-Ing.
Christoph Vogler)



TECHNISCHE
UNIVERSITÄT
WIEN
Vienna University of Technology

DISSERTATION

Thermal effects in micromagnetism - from ultrafast magnetization reversal to long term stability

submitted in partial fulfillment of the requirements for the degree of

Doktor der technischen Wissenschaften

by

Dipl.-Ing. Christoph Vogler

Registration Number 0425072

Schulgasse 28, 3950 Gmünd

to the Faculty of Physics
at the Vienna University of Technology

Advisor:

Privatdoz. Dipl.-Ing. Dr.techn. Dieter Süss

Institute of Solid State Physics – E138

The dissertation has been reviewed by:

(Privatdoz. Dipl.-Ing.
Dr.techn. Dieter Süss)

(Prof. Dr.
Manfred Albrecht)

Wien, 07.01.2015

(Dipl.-Ing.
Christoph Vogler)

Erklärung zur Verfassung der Arbeit

Dipl.-Ing. Christoph Vogler
Schulgasse 28, 3950 Gmünd

Hiermit erkläre ich, dass ich diese Arbeit selbstständig verfasst habe, dass ich die verwendeten Quellen und Hilfsmittel vollständig angegeben habe und dass ich die Stellen der Arbeit – einschließlich Tabellen, Karten und Abbildungen –, die anderen Werken oder dem Internet im Wortlaut oder dem Sinn nach entnommen sind, auf jeden Fall unter Angabe der Quelle als Entlehnung kenntlich gemacht habe.

(Ort, Datum)

(Unterschrift Dipl.-Ing.
Christoph Vogler)

Kurzfassung

Magnetische Prozesse umfassen einen großen Bereich von Zeitskalen, welcher von Jahrzehnten, in denen sich typischerweise die thermische Stabilität von magnetischen Speicherkörnern in Festplatten befindet, bis zu wenigen Pikosekunden, in welchen ultraschnelle Ummagnetisierungsprozesse ablaufen, reicht. Ziel der vorliegenden Arbeit ist es, das Verhalten magnetischer Nanostrukturen zu beschreiben. Im Speziellen wird der Einfluss der Temperatur sowohl auf deren Langzeitstabilität als auch auf ihre Dynamik während sehr kurzer Zeiten untersucht.

Festplatten bestehen aus zahlreichen magnetischen Körnern mit Größen im Nanometerbereich. Um Information binär auf eine Festplatte codieren zu können, muss die Magnetisierung jedes Korns entsprechend ausgerichtet werden. Aufgrund von thermischen Fluktuationen kann sich der magnetische Zustand nach genügend langen Zeiten willkürlich ändern. Da jedoch sehr lange Wartezeiten zwischen aufeinanderfolgenden Ummagnetisierungsprozessen liegen, ist eine Abschätzung der Stabilität der gespeicherten Information durch direkte Aufintegration der stochastischen Landau-Lifshitz-Gilbert (LLG) Gleichung, welche die grundlegende Bewegungsgleichung der magnetischen Momente in Rahmen des Mikromagnetismus beschreibt, praktisch nicht realisierbar. Die vorliegende Arbeit adaptiert die statistische Methode des Forward Flux Samplings (FFS) für den Mikromagnetismus. FFS erlaubt es die Raten von seltenen Ereignissen effizient zu berechnen, ohne dabei die langen Wartezeiten zwischen den Übergängen simulieren zu müssen. Daher ist es möglich thermische Stabilitäten von Jahren mit Simulationen im Nanosekundenbereich vorherzusagen. Zur Veranschaulichung wird die Stabilität eines Korns mit abgestufter Anisotropiekonstante mit den entsprechenden Stabilitäten von Körnern mit homogenem Material und unterschiedlichen Eigenschaften verglichen.

Im zweiten Teil der vorliegenden Arbeit wird hitzeunterstütztes magnetisches Schreiben von Daten behandelt. Bei dieser erst kürzlich entwickelten Technik erhitzt ein Laserpuls lokal und im Bruchteil einer Nanosekunde die Körner einer Festplatte nahe an oder über die Curie-Temperatur. Bei der Curie-Temperatur verschwindet die makroskopische Magnetisierung eines ferromagnetischen Teilchens und es wird parama-

gnetisch. Unter diesen Voraussetzungen verliert die mikromagnetische Annahme einer konstanten Magnetisierungslänge ihre Gültigkeit, wodurch das System direkt mit dem Heisenberg Modell beschrieben werden muss. Die stochastische Landau-Lifshitz-Bloch (LLB) Gleichung erweitert den Mikromagnetismus in der Weise, dass es nun auch zu einer longitudinalen Relaxation der Magnetisierung kommen kann, wodurch die Magnetisierungsdynamik auch bei hohen Temperaturen weiterhin korrekt repräsentiert werden kann. In dieser Arbeit wird ein grobkörniges Modell, welches auf der LLB Gleichung basiert, entwickelt, um magnetische Körner mit möglichst wenig Rechenaufwand zu beschreiben. Spezielles Augenmerk wird dabei auf die korrekte Behandlung der Austauschwechselwirkung zwischen Lagen mit unterschiedlichen Materialien eines Korns gelegt. Mit diesem Modell können somit magnetische Körner für den Einsatz im hitzeunterstützten magnetischen Schreiben schnell und zuverlässig optimiert werden.

Abstract

Magnetic processes cover a large range of time scales varying from decades, which is typically the thermal stability of magnetic recording grains, to picoseconds where ultrafast reversal processes take place. This work describes the behavior of magnetic nanostructures in the whole time range. In particular, it investigates the influence of temperature on both, the long-term stability and responses during very short time intervals.

Hard disk drives (HDDs) consist of various magnetic grains on the scale of nanometers. In order to encode binary information on a HDD the magnetization of each grain has to be aligned. Due to thermal fluctuations such a magnetic particle can randomly change its state after some time. Since there exist long waiting times between two magnetization reversals, it is infeasible to predict the stability of the stored information, by directly integrating the stochastic Landau-Lifshitz-Gilbert (LLG) equation, which represents the equation of motion of magnetic moments in the context of micromagnetism. This work adapts the statistical method of forward flux sampling (FFS) to micromagnetism. FFS allows to efficiently calculate the rate constants of rare events, without the necessity of simulating the system during the long waiting times between the transitions. Thus, it is possible to predict thermal stabilities of years with simulations in the nanosecond regime, without any free parameters. As an example, the stability of one graded media grain is compared with those of single phase grains with different properties.

The second part of this work addresses the modelling of heat-assisted recording. This is a recently developed technique, where a laser pulse locally heats the grains of a HDD near to or above the Curie temperature in a fraction of a nanosecond. At the Curie temperature the macroscopic magnetization of a ferromagnetic particle vanishes and it becomes paramagnetic. Under these conditions the micromagnetic assumption of a constant magnetization length fails and the magnetic system has to be described directly by the Heisenberg model. The stochastic Landau-Lifshitz-Bloch (LLB) equation extends micromagnetism, because it also considers the longitudinal relaxation of the magnetization, and thus correctly describes the magnetization dynamics at high temperatures. In this work a coarse-grained model based on the LLB equation is developed

to describe whole magnetic grains with little computational effort. Special emphasis is put on the correct treatment of the exchange coupling between different material layers in a grain. With this model it is possible to optimize magnetic grains for heat-assisted recording fast and reliably.

Contents

1	Introduction	1
2	Stochastic physics	3
2.1	Introduction	3
2.2	Fokker-Planck (FP) equation	4
2.2.1	One dimensional FP equation	4
2.2.2	Multivariate FP equation	5
2.3	Langevin equation and the road to its FP equation	5
2.3.1	One dimension	5
2.3.2	Multivariate case	7
2.4	Integration of stochastic differential equations	8
2.4.1	Numerical integration schema	10
3	Escape rates	12
3.1	Transition state theory (TST)	12
3.2	The Kramers problem	14
3.2.1	Intermediate to high damping (IHD) regime	14
3.2.2	Very low damping (VLD) regime	17
3.2.3	Kramers turnover regime	19
3.2.4	Summary	20
3.3	Escape rates in simple magnetic systems	21
3.3.1	Escape rate of superparamagnetic particles with axial symmetry	22
	Special case $\mathbf{H}_{\text{ext}} = 0$	24
3.3.2	Escape rate of superparamagnetic particles without axial symmetry	24
	Special case with an external field perpendicular to the easy axis	26
4	Thermal stability	28
4.1	Introduction	28
4.2	Magnetization dynamics	30

4.3	Forward Flux Sampling (FFS)	31
4.3.1	Error estimation	34
4.3.2	Optimization	35
4.4	Illustrative Model	37
4.4.1	Interface Definition and Verification	38
	Hyperplane method	40
	Results	41
	Euclidean norm method	45
	Results	46
4.4.2	Comparison of the computational efficiency	47
4.5	Graded media grains	50
5	Heat-assisted recording	56
5.1	Introduction	56
5.2	Dynamic equations	57
5.3	Temperature dependent material functions	60
5.3.1	Calculation of $m_e(T)$	60
5.3.2	Calculation of $\tilde{\chi}_{\parallel}(T)$ and $\tilde{\chi}_{\perp}(T)$	62
5.4	LLB versus VAMPIRE (dynamics comparison)	67
5.5	Intergrain exchange	72
5.6	Intergrain exchange field correction	74
5.7	Results	78
5.7.1	Model verification	78
5.7.2	Phase diagrams	86
5.8	Media design	91
6	Conclusion and outlook	93
6.1	Conclusion	93
6.2	Outlook	94
A	Jump moments	96
B	From LLG to Fokker-Planck	98
C	Thermal field strength in the LLG	102
D	Effective magnetic field	104
D.1	The continuous system	104
D.1.1	Exchange field	106

D.1.2	Anisotropy field	106
D.1.3	Demagnetization field	107
D.2	The discrete system	108
D.2.1	Exchange field	109
	Finite element approach	109
	Finite difference approach	110
D.2.2	Anisotropy field	112
D.2.3	Demagnetization field	112
E	From LLB to Fokker-Planck	113
E.1	Transversal part of the FP	114
E.2	Longitudinal part of the FP	114
F	Thermal field strength in the LLB	116
	Bibliography	118

Introduction

Magnetism plays an important role in many situations of our everyday life, ranging from rather simple tasks, like the navigation with a compass, to high technological applications, like magnetic resonance tomography. The main focus of this thesis lies on magnetic recording of hard disk drives dealing with both, ultrafast processes, which take place within a fraction of a nanosecond and rare events with waiting times of years or even decades between two succeeding transitions. Nevertheless, magnetic reversal processes on both time scales are equally relevant if one aims to design new types of hard disk drives with high storage densities and high stabilities of the stored data at the same time. Temperature is one of the driving forces in all investigated processes. Hence, a major preliminary work consists of the incorporation of temperature in the underlying equations of motion.

In this work the state of the art concepts of micromagnetism are extended to be able to estimate the long-term stability of hard drive disks as well as to describe the ultrafast dynamics of magnetic moments in recording grains in a reasonable amount of computation time.

The thesis is structured as follows: Chapter 2 outlines the basic concepts of stochastic physics in order to correctly treat the influence of temperature in an equation of motion. The calculation of escape rates or thermal stabilities of mechanical point particles, as well as of magnetic single-spin particles, is presented in Chapter 3. Chapter 4 shows how thermal stabilities of arbitrary complex magnetic nanostructures can be computed with forward flux sampling, which is one of the two main achievements of this work. Finally Chapter 5 deals with heat-assisted magnetic recording. In this chapter a computationally cheap model is introduced, which can correctly describe ultrafast magnetization dynamics near or above the Curie temperature and which allows to design advanced recording media with high storage densities. Chapter 6 gives a summary of

the thesis and points out some possibilities to apply or to further develop the presented methods.

Stochastic physics

This chapter mainly follows the books of Risken [1], van Kampen [2], Wio et al. [3] and Kloeden et al. [4].

2.1 Introduction

In physics the influence of temperature can be efficiently treated with stochastic processes. If it is described with uncorrelated Gaussian distributed random numbers, the process is called white noise. According to the central limit theorem, the sum (or arithmetic mean) of a large number of arbitrarily distributed but identical and independent random numbers with well defined variance and expectation value yields (at least approximately) a normal distribution. Since temperature arises in the most physical systems from coupling to a heat bath, the underlying system in general is expected to interact with a large number of independent degrees of freedom. For this reason white noise is the most natural way to deal with temperature in systems, especially if the correlation time of the noise is much shorter than the time scale of interest.

For example, if we consider Brownian motion the movement of a large Brownian particle coupled to a heat bath with a solvent of small particles is investigated. Due to the ongoing impacts of the small solvent particles the Brownian particle is moved. The time scale of the noise, mimicked by impacts of the solvent particles, is much shorter than the time scale over which the motion of the Brownian particle is modeled. Hence, white noise is an appropriate choice to account for temperature in such a case.

In magnetic systems the magnetization of a particle persistently interacts with a heat bath consisting of magnons, phonons, conduction electrons and so forth, which are independent and all have the same stochastic properties. Based on these interactions

the magnetization fluctuates, but on a time scale which is again much shorter than the deterministic precession period of the magnetization.

Mathematically a stochastic process $\xi(t)$ with white noise properties is given by

$$\langle \xi(t) \rangle = 0 \quad (2.1)$$

$$\langle \xi(t)\xi(t') \rangle = 2D\delta(t - t'). \quad (2.2)$$

The process has zero mean and is delta correlated, because at different times the values of the process are statistically independent. The latter property indicates that white noise is Markovian, meaning that the process has no memory, and thus values of $\xi(t)$ in the past do not influence future values.

2.2 Fokker-Planck (FP) equation

The Fokker-Planck (FP) equation is a master equation in terms of a second order differential equation for the time evolution of the probability density function ρ .

2.2.1 One dimensional FP equation

In one dimension the general form of the FP equation is

$$\frac{\partial \rho(x, t)}{\partial t} = -\frac{\partial}{\partial x} \left[a^{(1)}(x)\rho(x, t) \right] + \frac{1}{2} \frac{\partial^2}{\partial x^2} \left[a^{(2)}(x)\rho(x, t) \right] \quad (2.3)$$

The first term on the right-hand side is called drift term with the drift coefficient $a^{(1)}(x)$ and the second term is called diffusion term with the diffusion coefficient $a^{(2)}(x)$. Both coefficients are real differentiable functions, in which $a^{(2)}(x) > 0$ has to be valid. It is possible to derive them by taking the average change $\langle \Delta x \rangle$ of x and its mean squared displacement $\langle (\Delta x)^2 \rangle$ for short times Δt (we will discuss this in detail later). Once the drift and diffusion coefficients are calculated from the short time evolution of the system and inserted in the general FP equation (Eq. 2.3), one can compute the long time evolution of the system. This fact is just possible due to the Markovian nature of the system. Since $a^{(n)}(x)$ describes the behavior of the system for very short times, the coefficients are also called jump moments and are given by

$$a^{(n)}(x) = \int_{-\infty}^{\infty} (x' - x)^n W(x'|x) dx', \quad (2.4)$$

where $W(x'|x)$ is the probability per unit time for a transition from x to x' . The definition of the jump moments arises from the derivation of the FP equation from the master equation, which is not shown here in detail. With some effort the jump moments can be written in an alternative form (see appendix A)

$$a^{(n)}(x) = \lim_{\Delta t \rightarrow 0} \frac{1}{\Delta t} \left\langle [X(t + \Delta t) - X(t)]^n \right\rangle_{X(t)=x}. \quad (2.5)$$

Here $X(t)$ denotes a stochastic process.

2.2.2 Multivariate FP equation

To treat stochastic processes in more dimensions the above one dimensional Fokker-Planck equation (Eq. 2.3) as well as the jump moments (Eq. 2.5) are extendable to multivariate versions as follows

$$\frac{\partial \rho(\mathbf{x}, t)}{\partial t} = - \sum_i \frac{\partial}{\partial x_i} [a_i^{(1)}(\mathbf{x}) \rho(\mathbf{x}, t)] + \frac{1}{2} \sum_{ij} \frac{\partial^2}{\partial x_i \partial x_j} [a_{ij}^{(2)}(\mathbf{x}) \rho(\mathbf{x}, t)] \quad (2.6)$$

$$a_{j_1, \dots, j_n}^{(n)} = \lim_{\Delta t \rightarrow 0} \frac{1}{\Delta t} \left\langle \prod_{k=1}^n [X_{j_k}(t + \Delta t) - X_{j_k}(t)] \right\rangle \Big|_{X_i(t)=x_i}. \quad (2.7)$$

2.3 Langevin equation and the road to its FP equation

The Langevin equation is a stochastic differential equation (SDE) describing the time evolution of a physical quantity, driven by a stochastic influence like temperature.

2.3.1 One dimension

The general Langevin equation in one dimension has the form

$$\frac{dx}{dt} = A(x, t) + B(x, t)\xi(t), \quad (2.8)$$

where $\xi(t)$ is a stochastic process, which has white noise properties according to Eqs. 2.1 and 2.2 in our particular case. Due to the white noise character it follows that the solution of the Langevin equation is Markovian. As in the FP equation (Eq. 2.3) the Langevin equation is split into a drift term $A(x, t)$ and a diffusion term $B(x, t)\xi(t)$. If $B(x, t)$ is constant we call the noise additive, if not we call it multiplicative.

Since the Langevin equation describes a Markov process, we can try to transform it into a FP equation, based on the definition of the jump moments of Eq. 2.5. If it works, many interesting properties of the variable x and its dynamics are directly known, thanks to the mere appearance of the Langevin equation. First of all, Eq. 2.8 is integrated for short times

$$x(t + \Delta t) - x(t) = \int_t^{t+\Delta t} A[x(t'), t'] dt' + \int_t^{t+\Delta t} B[x(t'), t'] \xi(t') dt'. \quad (2.9)$$

We expand the drift and diffusion coefficients in a Taylor series around the initial value $x(t) = x$, because for short times the deviations of $x(t)$ from its initial value are expected

to be small

$$\begin{aligned} A[x(t'), t'] &= A(x, t') + \partial_x A(x, t') \Big|_x [x(t') - x] + \mathcal{O}([x(t') - x]^2) \\ B[x(t'), t'] &= B(x, t') + \partial_x B(x, t') \Big|_x [x(t') - x] + \mathcal{O}([x(t') - x]^2). \end{aligned} \quad (2.10)$$

Using this expansion Eq. 2.9 yields

$$\begin{aligned} x(t + \Delta t) - x(t) &\approx \int_t^{t+\Delta t} A(x, t') dt' \\ &+ \int_t^{t+\Delta t} \partial_x A(x, t') [x(t') - x] dt' \\ &+ \int_t^{t+\Delta t} B(x, t') \xi(t') dt' \\ &+ \int_t^{t+\Delta t} \partial_x B(x, t') [x(t') - x] \xi(t') dt'. \end{aligned} \quad (2.11)$$

Higher order terms are neglected. For the term $[x(t') - x]$ the same expression as Eq. 2.11 is used to iterate the whole equation resulting

$$\begin{aligned} x(t + \Delta t) - x(t) &\approx \int_t^{t+\Delta t} A(x, t') dt' \\ &+ \int_t^{t+\Delta t} \partial_x A(x, t') \int_t^{t'} A(x, t'') dt'' dt' \\ &+ \int_t^{t+\Delta t} \partial_x A(x, t') \int_t^{t'} B(x, t'') \xi(t'') dt'' dt' \\ &+ \int_t^{t+\Delta t} B(x, t') \xi(t') dt' \\ &+ \int_t^{t+\Delta t} \partial_x B(x, t') \xi(t') \int_t^{t'} A(x, t'') dt'' dt' \\ &+ \int_t^{t+\Delta t} \partial_x B(x, t') \xi(t') \int_t^{t'} B(x, t'') \xi(t'') dt'' dt' + \dots \end{aligned} \quad (2.12)$$

In order to derive the first jump moment according to Eq. 2.5, the above equation has to be averaged, taking into account the properties of white noise (Eqs. 2.1 and 2.2)

$$\begin{aligned} \langle x(t + \Delta t) - x(t) \rangle &= \int_t^{t+\Delta t} A(x, t') dt' \\ &+ 2D \int_t^{t+\Delta t} \partial_x B(x, t') \int_t^{t'} B(x, t'') \delta(t'' - t') dt'' dt' \\ &+ \mathcal{O}(\Delta t^2). \end{aligned} \quad (2.13)$$

As indicated with $\mathcal{O}(\Delta t^2)$ all other integrals in the sum are of second order or higher in Δt after the averaging procedure. The last integral in Eq. 2.13 produces

$$\int_t^{t'} B(x, t'') \delta(t'' - t') dt'' = \frac{1}{2} B(x, t'), \quad (2.14)$$

because the upper integration limit coincides with t' . Finally, the first jump moment is easy to write down as

$$\begin{aligned} a^{(1)}(x) &= \lim_{\Delta t \rightarrow 0} \frac{1}{\Delta t} \left\langle x(t + \Delta t) - x(t) \right\rangle \Big|_{x(t)=x} \\ &= \lim_{\Delta t \rightarrow 0} \left[A(x, t) + DB(x, t) \partial_x B(x, t) + \mathcal{O}(\Delta t) \right]. \end{aligned} \quad (2.15)$$

In the limit all higher order terms in Δt vanish. The computation of the second jump moment works similarly and is not shown here in detail. We summarize the first two jump moments to

$$\begin{aligned} a^{(1)}(x) &= A(x, t) + DB(x, t) \frac{\partial B(x, t)}{\partial x} \\ a^{(2)}(x) &= 2DB^2(x, t). \end{aligned} \quad (2.16)$$

With this result it is possible to immediately construct the FP equation of the general Langevin equation in one dimension, just with its coefficients

$$\frac{\partial \rho}{\partial t} = - \frac{\partial}{\partial x} \left\{ \left[A(x, t) + DB(x, t) \frac{\partial B(x, t)}{\partial x} \right] \rho \right\} + D \frac{\partial^2}{\partial x^2} [B^2(x, t) \rho]. \quad (2.17)$$

It has to be pointed out that besides the deterministic drift term $A(x, t)$ there exists an additional noise induced drift term $DB(x, t) \partial_x B(x, t)$.

2.3.2 Multivariate case

The same considerations as for the one dimensional Langevin equation hold for the multivariate case

$$\frac{dx_i}{dt} = A_i(\mathbf{x}, t) + \sum_k B_{ik}(\mathbf{x}, t) \xi_k(t). \quad (2.18)$$

With the first and second jump moments

$$\begin{aligned} a_i^{(1)}(\mathbf{x}) &= A_i(\mathbf{x}, t) + D \sum_{jk} B_{jk}(\mathbf{x}, t) \frac{\partial B_{ik}(\mathbf{x}, t)}{\partial x_j} \\ a_{ij}^{(2)}(\mathbf{x}) &= 2D \sum_k B_{ik}(\mathbf{x}, t) B_{jk}(\mathbf{x}, t), \end{aligned} \quad (2.19)$$

the FP equation becomes

$$\begin{aligned} \frac{\partial \rho}{\partial t} = & - \sum_i \frac{\partial}{\partial x_i} \left\{ \left[A_i(\mathbf{x}, t) + D \sum_{jk} B_{jk}(\mathbf{x}, t) \frac{\partial B_{ik}(\mathbf{x}, t)}{\partial x_j} \right] \rho \right\} \\ & + D \sum_{ij} \frac{\partial^2}{\partial x_i \partial x_j} \left\{ \left[\sum_k B_{ik}(\mathbf{x}, t) B_{jk}(\mathbf{x}, t) \right] \rho \right\}. \end{aligned} \quad (2.20)$$

If we are able to identify the drift and diffusion terms in the equation of motion (Langevin equation) of a system we can immediately write down the corresponding Fokker-Planck equation due to Eq. 2.20. In Sec. 3.3 we will need exactly this relation.

2.4 Integration of stochastic differential equations

In order to describe the evolution of a physical quantity under the influence of stochastic fluctuations one has to integrate the corresponding Langevin equation (Eq. 2.8) resulting in

$$X(t_1) = X(t_0) + \int_{t_0}^{t_1} A(X(t), t)dt + \int_{t_0}^{t_1} B(X(t), t)\xi(t)dt. \quad (2.21)$$

Besides the second term on the right-hand side, which is a deterministic integral, the third term on the right-hand side represents a stochastic integral. The treatment of such an integral is not a priori clear. If $A(x, t) = 0$ and $B(x, t) = 1$, Eq. 2.21 reduces to

$$X(t_1) = X(t_0) + \int_{t_0}^{t_1} \xi(t)dt, \quad (2.22)$$

which represents Brownian motion, and thus $\xi(t)$ should be the derivative of a Wiener process (which mathematically describes Brownian motion).

Definition 1. A Wiener process $W(t)$ is a stochastic process with the following properties:

- $W(t = 0) = 0$
- For increasing times $0 \leq t_1 < t_2 < \dots < t_n$ the increments $W(t_n) - W(t_{n-1})$ are independent random variables.
- For all $0 \leq s < t \leq \infty$ the increment $W(t) - W(s)$ is a Gaussian random variable with zero mean ($\mu = 0$) and a variance of $\sigma^2 = t - s$. In other words the increments are stationary and normal distributed.
- The sample paths $W(t)$ are continuous functions in time.

Although, according to Def. 1, a Wiener process is a continuous function, it is not differentiable at any point. This fact can be shown by investigating its difference quotient and taking into account Def. 1

$$\lim_{\Delta t \rightarrow 0} \frac{W(t + \Delta t) - W(t)}{\Delta t} \sim \lim_{\Delta t \rightarrow 0} \frac{\sqrt{\Delta t}}{\Delta t} \rightarrow \infty. \quad (2.23)$$

The difference quotient diverges, hence the Wiener process is not differentiable. For this reason, white noise is more usually defined indirectly by the the integral

$$W_t = \int_t^{t+\Delta t} \xi(t')dt'. \quad (2.24)$$

The average of W_t^2 evaluates to (with Eqs. 2.1 and 2.2)

$$\begin{aligned} \langle W_t^2 \rangle &= \int_t^{t+\Delta t} \int_t^{t+\Delta t} \langle \xi(t') \xi(t'') \rangle dt'' dt' \\ &= 2D \int_t^{t+\Delta t} \int_t^{t+\Delta t} \delta(t' - t'') dt'' dt' \\ &= 2D\Delta t, \end{aligned} \quad (2.25)$$

illustrating the increment of a Wiener process being proportional to the root of the time increment $\sqrt{\Delta t}$.

Under the above considerations the stochastic integral of an arbitrary integrand is properly defined if we interpret the integrand $f(t)$ as a step wise function $f^{(n)}(t) = f(\xi_j^{(n)})$

$$\int_0^T f(t) dW_t = \lim_{n \rightarrow \infty} \sum_{j=1}^n f(\xi_j^{(n)}) \left[W_{t_{j+1}^{(n)}} - W_{t_j^{(n)}} \right], \quad (2.26)$$

where $\xi_j^{(n)}$ are the evaluation points of the integrand in the interval $t_j^{(n)} \leq \xi_j^{(n)} \leq t_{j+1}^{(n)}$ as long as $0 = t_1^{(n)} < t_2^{(n)} < \dots < t_{n+1}^{(n)} = T$ holds. Here it is assumed that $f^{(n)}(t)$ converges to the true integrand in a mean square sense

$$E \left(\left| f^{(n)}(t) - f(t) \right|^2 \right) \rightarrow 0 \quad \text{for} \quad n \rightarrow \infty, \quad (2.27)$$

with E denoting the expectation value. The most interesting interpretations of the stochastic integral are those with symmetric evaluation points

$$\xi_j^{(n)} = (1 - \lambda)t_j^{(n)} + \lambda t_{j+1}^{(n)}, \quad (2.28)$$

with $0 \leq \lambda \leq 1$. After a Taylor expansion of the integrand $f\left((1 - \lambda)t_j^{(n)} + \lambda t_{j+1}^{(n)}\right)$, Eq. 2.26 becomes

$$\int_0^T f(t) dW_t = \lim_{n \rightarrow \infty} \sum_{j=1}^n \left[(1 - \lambda)f\left(t_j^{(n)}\right) + \lambda f\left(t_{j+1}^{(n)}\right) \right] \left[W_{t_{j+1}^{(n)}} - W_{t_j^{(n)}} \right]. \quad (2.29)$$

For $\lambda = 0$ and $\lambda = \frac{1}{2}$ the famous Itô and Stratonovich interpretations follow

$$\int_0^T f(t) dW_t = \lim_{n \rightarrow \infty} \sum_{j=1}^n \left[W_{t_{j+1}^{(n)}} - W_{t_j^{(n)}} \right] \begin{cases} f\left(t_j^{(n)}\right) & \text{Itô} \\ \frac{1}{2}f\left(t_j^{(n)}\right) + \frac{1}{2}f\left(t_{j+1}^{(n)}\right) & \text{Stratonovich.} \end{cases} \quad (2.30)$$

In the Itô interpretation the integrand is evaluated at the beginning of each partition subinterval $[t_j^{(n)}, t_{j+1}^{(n)}]$, whereas in the Stratonovich interpretation the integrand is evaluated at the midpoint. The result of Eq. 2.30 has to be extended to integrands which

also depend on X_t

$$\int_0^T h(X_t, t) dW_t = \lim_{n \rightarrow \infty} \sum_{j=1}^n \left[W_{t_{j+1}^{(n)}} - W_{t_j^{(n)}} \right] \begin{cases} h \left(t_j^{(n)}, X_{t_j^{(n)}} \right) & \text{It\^o} \\ h \left(t_j^{(n)}, \frac{1}{2} X_{t_j^{(n)}} + \frac{1}{2} X_{t_{j+1}^{(n)}} \right) & \text{Stratonovich.} \end{cases} \quad (2.31)$$

Which interpretation schema has to be used to integrate a stochastic differential equation (SDE) is part of the modeling process. Both presented interpretations are mathematically correct but they may yield quite different dynamic properties. A definite advantage of the Stratonovich stochastic calculus is that it obeys the transformation rules of non-stochastic calculus, like for example the chain rule, in contrast to the It\^o interpretation. Furthermore a theorem of Wong and Zakai [5] states that the Stratonovich interpretation of a differential equation is the correct choice, if the proposed white noise is just an idealization of real colored noise. As a consequence the Stratonovich calculus is preferred in most physical systems. Nevertheless a SDE interpreted according to Stratonovich can still be transformed to the corresponding It\^o SDE. For example, if we have the Langevin equation

$$dX_t = A(X_t, t)dt + B(X_t, t)dW_t \quad (2.32)$$

in Stratonovich calculus, it can be shown [4, 6] that the corresponding It\^o version has the form

$$dX_t = A(X_t, t)dt + \frac{1}{2} B(X_t, t) \frac{\partial B(X_t, t)}{\partial X_t} + B(X_t, t)dW_t, \quad (2.33)$$

where we find an additional noise induced drift term. Both SDE then provide the same dynamics. The transformation of course also works the other way around.

2.4.1 Numerical integration schema

For the numerical integration of a Stratonovich SDE the stochastic Heun schema (or any other explicit midpoint schema) is an appropriate option, because the integrand is naturally evaluated in between the integration nodes. Hence, one does not need to worry about the interpretation of the stochastic integral. The Heun schema converges quadratically to the solution of the underlying SDE. To solve the Langevin equation

$$\Delta x = A(x, t)\Delta t + B(x, t)\Delta W, \quad (2.34)$$

numerically a predictor solution is calculated according to the convenient Euler algorithm

$$x_{j+1}^{[P]} = x_j + A(x_j, t_j)\Delta t + B(x_j, t_j)\Delta W. \quad (2.35)$$

This predictor is then used to obtain the new value x_{j+1} in the next time step

$$x_{j+1} = \frac{1}{2}x_j + \frac{1}{2} \left[x_{j+1}^{[P]} + A(x_{j+1}^{[P]}, t_{j+1})\Delta t + B(x_{j+1}^{[P]}, t_{j+1})\Delta W \right]. \quad (2.36)$$

Escape rates in mechanical and magnetic systems

3.1 Transition state theory (TST)

We consider a mechanical particle trapped in the well a of a one-dimensional potential $U(x)$ (see Fig. 3.1). Transition state theory (TST) [7, 8, 9] allows to calculate the escape rate of the particle out of the well over the energy barrier with height E_{ab} . This energy

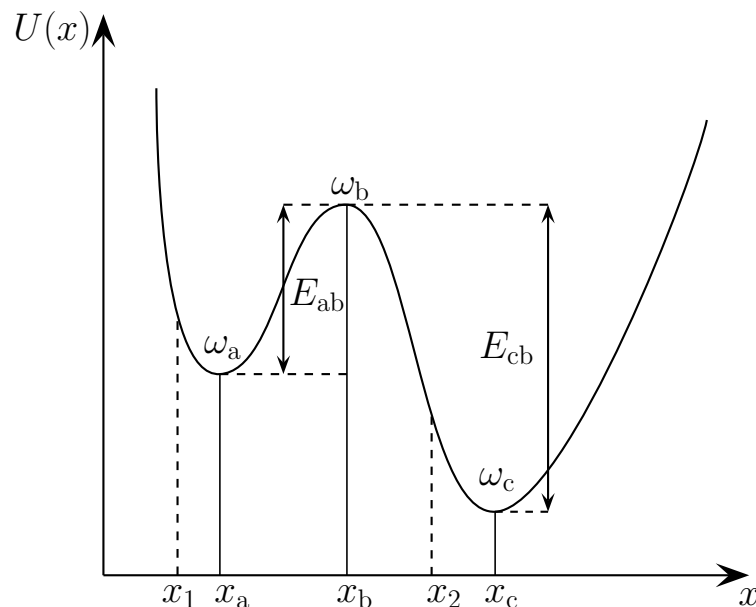


Figure 3.1: Double well potential with energy barriers E_{ab} and E_{cb} . The wells are located around x_a and x_c and the barrier top is at x_b .

barrier identifies the transition state, which serves as a dividing surface separating two metastable states a and c . TST contains two basic assumptions:

- The particle is in thermal equilibrium for all times.
- A particle which crosses the transition state can NOT recross it.

Since true thermodynamic equilibrium during the whole escape process is unrealistic (especially in the transition state), equilibrium is assumed if the thermalization process in the initial well is much faster than the actual crossing of the transition state [10]. For a simple derivation of the TST escape rate it is further assumed that the system is not coupled to a heat bath (but thermal equilibrium still prevails). Under these conditions the escape rate is computed as average of the flux over the energy barrier [11]

$$k_{a \rightarrow c} = \frac{1}{2\pi\hbar Z_0} \int \delta(x = x_b) \theta(p) \frac{p}{m} e^{-\frac{\mathcal{H}(x,p)}{k_B T}} dx dp, \quad (3.1)$$

where $\mathcal{H}(x,p)$ is the Hamiltonian of the particle, $\theta(p)$ is the Heaviside theta function and Z_0 is the canonical partition function in the initial well

$$Z_0 = \frac{1}{2\pi\hbar} \int_a e^{-\frac{\mathcal{H}(x,p)}{k_B T}} dx dp. \quad (3.2)$$

If the transition state is located at $x_b = 0$ the spatial integral in Eq. 3.1 vanishes due to the delta function. Under the condition that the zero-point energy is inside the initial well ($E_a = 0$), the impulse integral can be solved directly

$$k_{a \rightarrow c} = \frac{1}{2\pi\hbar Z_0} \frac{1}{m} \int_0^\infty p e^{-\frac{1}{k_B T} \left(\frac{p^2}{2m} + U(0) \right)} dp = \frac{k_B T}{2\pi\hbar Z_0} e^{-\frac{E_{ab}}{k_B T}}. \quad (3.3)$$

To compute the partition function one has to perform a transformation from phase-space variables (x,p) to energy-phase variables (E,φ) . With $dx dp = \frac{1}{\omega(E)} dE d\varphi$ the partition function becomes

$$Z_0 = \frac{1}{2\pi\hbar} \int_0^\infty \int_0^{2\pi} e^{-\frac{E}{k_B T}} \frac{dE d\varphi}{\omega(E)} = \frac{1}{\hbar} \int_0^\infty e^{-\frac{E}{k_B T}} \frac{dE}{\omega(E)}. \quad (3.4)$$

$\omega(E)$ is the angular frequency at the energy E and can be expressed with the action as

$$\frac{\omega(E)}{2\pi} = \frac{\partial E}{\partial I}. \quad (3.5)$$

Since the integrand in Eq. 3.4 vanishes for high energies and the main contributions originate from energies in the a -well, $\omega(E)$ is approximated with the angular frequency at the initial well bottom

$$Z_0 = \frac{1}{\hbar\omega_a} \int_0^\infty e^{-\frac{E}{k_B T}} dE = \frac{k_B T}{\hbar\omega_a}. \quad (3.6)$$

Inserting Eq. 3.6 into Eq. 3.3 yields the final TST escape rate

$$k_{a \rightarrow c}^{\text{TST}} = \frac{\omega_a}{2\pi} e^{-\frac{E_{ab}}{k_B T}}. \quad (3.7)$$

This result is an upper limit for all escape rates, because recrossing of the transition state and friction are neglected, which both lower the rate. Hence, TST always overestimates the true escape rate.

3.2 The Kramers problem

As in the previous section, we consider a Brownian particle trapped in a one-dimensional asymmetric double-well potential $U(x)$ (see Fig. 3.1), and thus subject to the external force $F(x) = -U'(x)$. In contrast to the TST derivation the system is coupled to a surrounding heat bath. Hence, an additional frictional force $-\alpha \frac{dx}{dt}$ acts on the particle. The resulting equation of motion is

$$m \frac{d^2 x}{dt^2} = F(x) - \alpha \frac{dx}{dt} + \xi(t), \quad (3.8)$$

where m is the mass of the Brownian particle and $\xi(t)$ is a random force represented by Gaussian white noise, which accounts for the temperature. The white noise has zero mean and its strength can be obtained by the fluctuation-dissipation theorem to

$$\begin{aligned} \langle \xi(t) \rangle &= 0 \\ \langle \xi(t) \xi(t') \rangle &= 2\alpha k_B T \delta(t - t'). \end{aligned} \quad (3.9)$$

From the Langevin equation (Eq. 3.8) one can construct the corresponding Fokker-Planck (FP) equation, which is also known as Kramers or Klein-Kramers equation

$$\frac{\partial \rho}{\partial t} = -v \frac{\partial \rho}{\partial x} - \frac{F(x)}{m} \frac{\partial \rho}{\partial v} + \frac{\alpha}{m} \frac{\partial (v\rho)}{\partial v} + \frac{\alpha k_B T}{m^2} \frac{\partial^2 \rho}{\partial v^2}. \quad (3.10)$$

This differential equation describes the time evolution of the probability density $\rho(x, v, t)$ of the Brownian particle in a potential and depends on its position x , on its velocity v as well as on time t . Solving the Kramers equation for the probability density enables us to calculate the rate at which the particles escape over the barrier.

3.2.1 Intermediate to high damping (IHD) regime

Depending on the friction two regimes have to be distinguished. First the case of high friction is investigated. Thermalization is fast, and hence it is assumed that thermal equilibrium is maintained for all times inside the initial well. Further the existence of a particle source in the initial well at $x_1 < x_a$ and a sink of particles beyond the barrier

at $x_2 > x_b$ (see Fig. 3.1) are supposed. Particles in the initial well can escape over the barrier after a finite time yielding a flux J_0 in the steady state. The escape rate constant then equals the flux over population

$$k_{a \rightarrow c} = \frac{J_0}{n_0}, \quad (3.11)$$

where n_0 is the number of particles in the initial well

$$n_0 = \int_a \rho_0(x, v) dx dv. \quad (3.12)$$

The final goal is to derive the steady state distribution function $\rho_0(x, v)$, which in turn allows to calculate n_0 as well as J_0 and finally yields the rate constant

$$k_{a \rightarrow c} = \frac{\int_{-\infty}^{\infty} v \rho_0(x = x_b, v) dv}{\int_a \rho_0(x, v) dx dv}. \quad (3.13)$$

Since the particles are assumed to be in thermal equilibrium in the initial well, $\rho_0(x, v)$ should equal the Boltzmann distribution in this region

$$\bar{\rho}(x, v) = \frac{1}{Z} e^{-\beta [U(x) + \frac{mv^2}{2}]}. \quad (3.14)$$

In this equation Z is a normalization constant and $\beta = (k_B T)^{-1}$. Near the bottom of the c -well all particles are removed because of the sinks at x_2 , and thus the steady state probability density should become zero ($\rho(x, v) = 0$ for $x > x_2$). Consequently Kramers [12] constructed $\rho_0(x, v)$ as

$$\rho_0(x, v) = \zeta(x, v) \bar{\rho}(x, v), \quad (3.15)$$

with $\zeta(x, v) = 1$ in the initial well and $\zeta(x, v) = 0$ around x_2 . The introduced function $\zeta(x, v)$ just changes significantly in the barrier region where the potential $U(x)$ is approximated with a parabola

$$U(x) = U(x_b) - \frac{1}{2} m \omega_b^2 (x - x_b)^2. \quad (3.16)$$

Inserting Eqs. 3.15 and 3.16 in the Kramers equation (Eq. 3.10) and using $\frac{\partial \rho_0(x, v)}{\partial t} = 0$ results an equation for the so far unknown function $\zeta(x, v)$

$$-v \frac{\partial \zeta}{\partial x} - \omega_b^2 (x - x_b) \frac{\partial \zeta}{\partial v} - v \frac{\alpha}{m} \frac{\partial \zeta}{\partial v} + \frac{\alpha}{\beta m^2} \frac{\partial^2 \zeta}{\partial v^2} = 0. \quad (3.17)$$

To solve this differential equation Kramers proposed that $\zeta(x, v)$ just depends on a linear combination of x and v

$$\zeta(x, v) = \zeta(\eta) = \zeta[v - c(x - x_b)]. \quad (3.18)$$

This assumption implies that the deviation of the steady state probability density from the Boltzmann distribution just depends on η . With the substitution of Eq. 3.18, Eq. 3.17 reduces to an ordinary differential equation for $\zeta(\eta)$

$$\frac{d\zeta(\eta)}{d\eta} \left[v \left(c - \frac{\alpha}{m} \right) - \omega_b^2 (x - x_b) \right] + \frac{\alpha}{\beta m^2} \frac{d^2\zeta(\eta)}{d\eta^2} = 0. \quad (3.19)$$

With

$$\omega_b^2 = c \left(c - \frac{\alpha}{m} \right) \quad (3.20)$$

Eq. 3.19 simply depends on η

$$\left(c - \frac{\alpha}{m} \right) \eta \frac{d\zeta(\eta)}{d\eta} + \frac{\alpha}{\beta m^2} \frac{d^2\zeta(\eta)}{d\eta^2} = 0, \quad (3.21)$$

which can be directly solved. Finally $\zeta(\eta)$ becomes

$$\zeta(\eta) = \sqrt{\frac{(c - \frac{\alpha}{m}) \beta m^2}{2\pi\alpha}} \int_{-\infty}^{\eta} e^{-\frac{(c - \frac{\alpha}{m}) \beta m^2}{2\alpha} \eta'^2} d\eta'. \quad (3.22)$$

Using Eq. 3.22 one can now construct $\rho_0(x, v)$ with Eqs. 3.15 and 3.18 and then evaluate J_0 to

$$J_0 = \frac{e^{-\beta U(x_b)}}{Z \beta m \omega_b} \left(\sqrt{\frac{\alpha^2}{4m^2} + \omega_b^2} - \frac{\alpha}{2m} \right), \quad (3.23)$$

according to Eq. 3.13. For the computation of the number of particles in the initial well $\rho_0(x, v)$ reduces to the Boltzmann distribution, because $\zeta(\eta) = 1$ is valid

$$n_0 = \frac{1}{Z} \int e^{-\beta [U(x) + \frac{mv^2}{2}]} dx dv. \quad (3.24)$$

Since the potential in the initial well is again approximated by a parabola n_0 yields

$$n_0 = \frac{2\pi}{\beta m Z \omega_a} e^{-\beta U(x_a)} \quad (3.25)$$

and the rate constant is

$$\begin{aligned} k_{a \rightarrow c}^{\text{IHD}} &= \frac{\omega_a}{2\pi\omega_b} \left(\sqrt{\frac{\alpha^2}{4m^2} + \omega_b^2} - \frac{\alpha}{2m} \right) e^{-\beta E_{ab}} \\ &= \left(\sqrt{\frac{\alpha^2}{4m^2\omega_b^2} + 1} - \frac{\alpha}{2m\omega_b} \right) k_{a \rightarrow c}^{\text{TST}}. \end{aligned} \quad (3.26)$$

This result illustrates the spatial-diffusion-controlled rate of escape at moderate to strong friction α . Since coupling to a heat bath, and thus friction is considered in Kramers derivation $k_{a \rightarrow c}^{\text{IHD}}$ corrects the TST rate (Eq. 3.7), which is independent of α . In the overdamped regime ($\alpha \gg \omega_b$) Eq. 3.26 further simplifies to

$$k_{a \rightarrow c}^{\text{overdamped}} = \frac{\omega_b m}{\alpha} k_{a \rightarrow c}^{\text{TST}}. \quad (3.27)$$

3.2.2 Very low damping (VLD) regime

In the low frictional regime the energy of a particle is almost conserved during an oscillation in the initial potential well. It can not be assumed any more that the particles in the initial well are in thermal equilibrium before escaping over the barrier. To solve the escape rate problem a change of coordinates is required $(x, v) \rightarrow (I, \varphi)$. Energy and action

$$I(E) = m \oint v dx \quad (3.28)$$

can be equivalently used in this context. Since the change in the angle variable φ is very fast compared with the variation of the energy Eq. 3.10 can be averaged over φ . The first two terms on the right-hand side vanish after the averaging procedure, because without Brownian forces (friction) the distribution in energy is preserved, and thus terms without friction cancel out. The averaging of the last two terms in Eq. 3.10 leads to a diffusion equation for the probability density of the action

$$\begin{aligned} \frac{\partial \bar{\rho}}{\partial t} &= \overline{\frac{\alpha}{m} \frac{\partial}{\partial v} \left(v \rho + \frac{1}{\beta m} \frac{\partial \rho}{\partial v} \right)} \\ &= \frac{\alpha}{m} \frac{\partial}{\partial I} \left(I + \frac{2\pi I}{\beta \omega(I)} \frac{\partial}{\partial I} \right) \bar{\rho}(I, t). \end{aligned} \quad (3.29)$$

$\omega(I)$ is the angular frequency at the energy E (action I)

$$\frac{\omega(I)}{2\pi} = \frac{\partial E}{\partial I}. \quad (3.30)$$

With this identity Eq. 3.29 can be written equivalently as

$$\frac{\partial \bar{\rho}(I, t)}{\partial t} = \frac{\alpha}{m} \frac{\partial}{\partial I} \left(I + \frac{I}{\beta} \frac{\partial}{\partial E} \right) \bar{\rho}(I, t). \quad (3.31)$$

Our goal is again to obtain a stationary solution of the probability density $\bar{\rho}(I)$ to consequently derive an expression for the escape rate constant according to

$$k_{a \rightarrow c} = \frac{J_0}{n_0} = \frac{J_0}{\int_0^{I_{ab}} \bar{\rho}(I) dI}. \quad (3.32)$$

The stationary probability flux in action space J_0 is defined that Eq. 3.31 has the form of a continuity equation

$$\begin{aligned} J_0 &= -\frac{\alpha}{m} \left(I \bar{\rho} + \frac{I}{\beta} \frac{\partial \bar{\rho}}{\partial E} \right) \\ &= -\frac{\alpha}{m\beta} I e^{-\beta E} \frac{\partial}{\partial E} \left(\bar{\rho} e^{\beta E} \right). \end{aligned} \quad (3.33)$$

Equation 3.33 can now be solved for the steady state probability density

$$\bar{\rho}(I) = -\frac{e^{-\beta E} m \beta}{\alpha} \int_E^{E_{ab}} J_0 \frac{e^{\beta E'}}{I(E')} dE'. \quad (3.34)$$

In case of stationarity $\frac{\partial J_0}{\partial I} = \frac{\partial J_0}{\partial E} = 0$ has to be valid to fulfill the continuity relation

$$\frac{\partial \bar{\rho}(I)}{\partial t} = -\frac{\partial}{\partial I} J_0 = 0. \quad (3.35)$$

Hence, J_0 can be written in front of the energy integral in Eq. 3.34. Inserting Eq. 3.34 in Eq. 3.32 yields

$$k_{a \rightarrow c}^{-1} = -\frac{m\beta}{\alpha} \int_0^{I_{ab}} e^{-\beta E(I)} \int_E^{E_{ab}} \frac{e^{\beta E'}}{I(E')} dE' dI. \quad (3.36)$$

The first integral in Eq. 3.36 can be transformed to an energy integral using Eq. 3.30. After performing an integration by parts the inverse rate constant becomes

$$k_{a \rightarrow c}^{-1} = \frac{m\beta}{\alpha} \int_0^{E_{ab}} \frac{e^{\beta E'}}{I(E')} \int_0^{E'} 2\pi \frac{e^{-\beta E}}{\omega(E)} dE dE'. \quad (3.37)$$

Due to the negative exponent just low energies contribute to the second integral in Eq. 3.37 and the angular frequency can be approximated with $\omega(E) \sim \omega_a$. For the same reason the upper integration limit can be extended to infinity, which leads to

$$\int_0^{E'} 2\pi \frac{e^{-\beta E}}{\omega(E)} dE = \frac{2\pi}{\omega_a} \int_0^\infty e^{-\beta E} dE = \frac{2\pi}{\beta\omega_a}. \quad (3.38)$$

For large energy barriers $\beta E_{ab} \gg 1$ the integrand of the remaining integral in Eq. 3.37 has its main contribution for energies near the barrier. The action $I(E')$ can thus be approximated with the action at E_{ab}

$$\int_0^{E_{ab}} \frac{e^{\beta E'}}{I(E')} dE' = \frac{1}{I(E_{ab})} \int_0^{E_{ab}} e^{\beta E'} dE' = \frac{e^{\beta E_{ab}} - 1}{\beta I(E_{ab})} \approx \frac{e^{\beta E_{ab}}}{\beta I(E_{ab})}. \quad (3.39)$$

Finally the rate simplifies to

$$k_{a \rightarrow c}^{-1} = \frac{m\beta}{\alpha} \frac{e^{\beta E_{ab}}}{\beta I(E_{ab})} \frac{2\pi}{\beta\omega_a}. \quad (3.40)$$

$$\begin{aligned} \Rightarrow k_{a \rightarrow c}^{\text{VLD}} &= \frac{\alpha\beta}{m} I(E_{ab}) \frac{\omega_a}{2\pi} e^{-\beta E_{ab}} \\ &= \frac{\alpha\beta}{m} I(E_{ab}) k_{a \rightarrow c}^{\text{TST}}. \end{aligned} \quad (3.41)$$

This result illustrates the energy-diffusion-controlled rate of escape at small friction α . In contrast to the high frictional regime the escape rate increases for increasing friction. The system can just change its energy via the coupling to the heat bath, and thus the change of energy is low for weak coupling (low friction). So the system needs more time to gain enough energy to overcome the barrier for decreasing friction.

Strictly speaking the previous derivation is just valid for a single-well potential. For a true double-well potential the possibility of a particle to bounce between the metastable wells is not vanishing, because the energy is almost conserved in the system. For example, a symmetric double-well potential leads to a correction factor of $\frac{1}{2}$ in the escape rate of Eq. 3.41 [13], because a particle with enough energy to overcome the barrier has a 50:50 chance to finally end up in the c -well.

3.2.3 Kramers turnover regime

As illustrated, Kramers derived escape rate formulas for the IHD (Eq. 3.26) and VLD (Eq. 3.41) regime. To quantify the validity of the escape rate equations one can use the product of the action at the energy barrier and the friction $\alpha I(E_{ab})$. This expression can be interpreted as the energy loss during one cycle of the oscillatory movement of a particle with energy E_{ab} . If the so dissipated energy is larger than the thermal energy the IHD formula can be safely applied and if the energy loss per cycle is much smaller than the thermal energy the VLD limit is valid.

$$k_{a \rightarrow c} = k_{a \rightarrow c}^{\text{TST}} \begin{cases} \frac{\alpha \beta}{m} I(E_{ab}) & , \frac{\alpha I(E_{ab})}{m} \ll k_B T \\ \left(\sqrt{\frac{\alpha^2}{4m^2 \omega_b^2} + 1} - \frac{\alpha}{2m\omega_b} \right) & , \frac{\alpha I(E_{ab})}{m} > k_B T \end{cases} \quad (3.42)$$

Kramers did not find an expression for the turnover region $\frac{\alpha I(E_{ab})}{m} \approx k_B T$. It took almost 50 years till Mel'nikov and Mehskov [14] solved the so called Kramers turnover problem and derived an interpolation formula, which is approximately valid for all damping regimes. They constructed a FP equation in energy and action as independent variables in order to express the energy distribution function at a given action. This is justified because the total energy is the slowest varying quantity. The potential energy is much larger than both, the thermal energy and the dissipated energy during one oscillatory cycle of a particle, and thus damping and thermal force just perturb the deterministic part of the escape process. According to Kramers VLD result, it is further assumed that just particles with energies around E_{ab} produce the flux over the energy barrier. Mel'nikov and Mehskov then constructed a Green function of the FP equation in the vicinity of the barrier energy. With this Green function one can write down an integral equation for the energy distribution function. The so obtained equation is solved by the Wiener-Hopf method [15], yielding a correction factor for Kramers IHD escape rate expression, which is independent of the friction. The detailed derivation is not shown here, but can be looked up in Ref. [14]. The final escape rate for a single-well potential is

$$k_{a \rightarrow c} = A \left(\frac{\beta \alpha I(E_{ab})}{m} \right) k_{a \rightarrow c}^{\text{IHD}}, \quad (3.43)$$

with the so called depopulation factor $A(\Delta)$

$$A(\Delta) = \exp \left(\frac{1}{2\pi} \int_{-\infty}^{\infty} \ln \left[1 - e^{-\Delta(\lambda^2 + \frac{1}{4})} \right] \right) \frac{d\lambda}{\lambda^2 + \frac{1}{4}}. \quad (3.44)$$

For an asymmetric double-well potential according to Fig. 3.1 the escape rate out of the a -well becomes

$$k_{a \rightarrow c} = \frac{A \left(\frac{\alpha \beta I_{ab}}{m} \right) A \left(\frac{\alpha \beta I_{cb}}{m} \right)}{A \left(\frac{\alpha \beta (I_{ab} + I_{cb})}{m} \right)} k_{a \rightarrow c}^{\text{IHD}}, \quad (3.45)$$

where I_{ab} and I_{cb} are the action integrals at the different barrier heights from both wells of the potential. For completeness it is mentioned that in Ref. [16, 17] the approach of Mel'nikov and Mehskov is extended and their results are confirmed. In the latter work even memory friction instead of white noise is successfully treated.

3.2.4 Summary

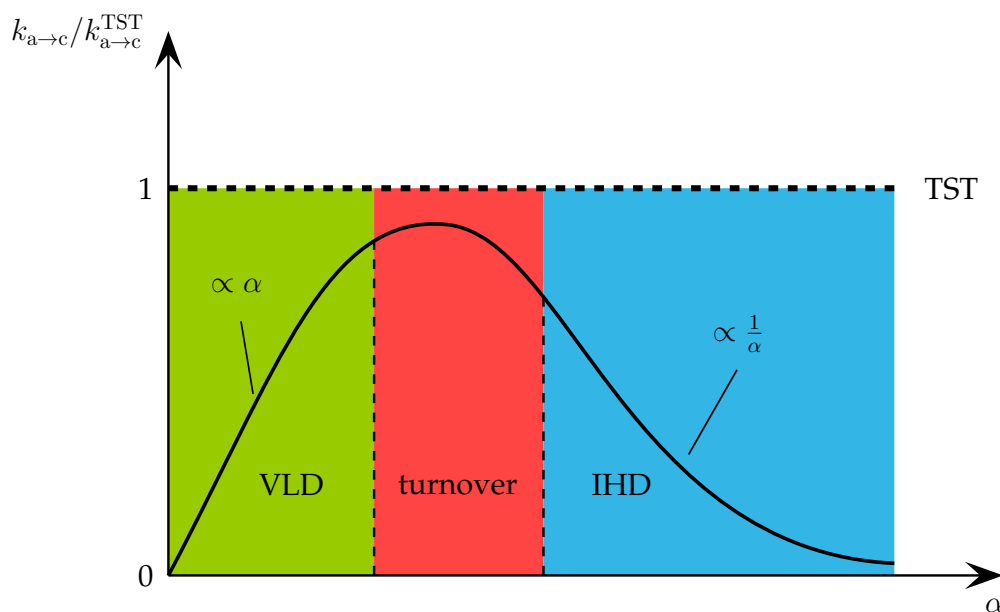


Figure 3.2: Sketch of the escape rate behavior of a mechanical particle in the various damping regimes. For low damping (VLD) the rate is proportional to the friction α , in the IHD regime it is inverse proportional to α . In the turnover region exists a maximum. The upper limit is given with the TST rate (Eq. 3.7), which is marked with a dashed horizontal line.

The qualitative behavior of the escape rate in all damping regimes is schematically summarized in Fig. 3.2. In the low friction limit (VLD) the escape rate increases proportionally with the damping α (Eq. 3.41). In contrast, the rate is inverse proportional to the friction in the intermediate to high damping limit (IHD) (Eq. 3.26). The escape rate reaches a maximum in the turnover region. This maximum is still smaller than the TST result (Eq. 3.7), which represents the upper limit for the escape rate of a mechanical particle out of a potential well, because friction as well as recrossing of the particle over the transition state (energy barrier) are neglected.

3.3 Escape rates in simple magnetic systems

Kramers calculated the escape rate of mechanical particles coupled to a heat bath in an external potential. In case of magnetic systems we are interested in the rate of change of a particle's magnetic configuration. The dynamics of the magnetization \mathbf{M} of a particle follows the Landau-Lifshiz-Gilbert (LLG) equation

$$\begin{aligned} \frac{d\mathbf{M}}{dt} = & - \frac{\gamma}{1 + \alpha^2} \left[\mathbf{M} \times \left(-\frac{\partial V(\mathbf{M})}{\partial \mathbf{M}} + \boldsymbol{\xi}(t, \mathbf{r}) \right) \right] \\ & - \frac{\alpha\gamma}{(1 + \alpha^2) M_S} \left\{ \mathbf{M} \times \left[\mathbf{M} \times \left(-\frac{\partial V(\mathbf{M})}{\partial \mathbf{M}} + \boldsymbol{\xi}(t, \mathbf{r}) \right) \right] \right\}, \end{aligned} \quad (3.46)$$

where γ is the absolute value of the electron gyromagnetic ratio, α is the dimensionless Gilbert damping parameter describing the friction of the system, M_S is the saturation magnetization and $V(\mathbf{M})$ denotes the Gibbs free energy density of the particle. As for the mechanical particle a random force in terms of a random thermal field $\boldsymbol{\xi}(t, \mathbf{r})$, accounting for thermal fluctuations, drives the magnetization. We assume all components of $\boldsymbol{\xi}(t, \mathbf{r})$ to have white noise properties with zero mean and a variance of

$$\langle \xi_i(t, \mathbf{r}) \xi_j(t', \mathbf{r}') \rangle = 2D \delta_{ij} \delta(\mathbf{r} - \mathbf{r}') \delta(t - t') \quad (3.47)$$

$$D = \frac{\alpha}{\gamma \mu_0^2 M_S \beta v}. \quad (3.48)$$

The strength of the thermal field D is given in Eq. 3.48 with the temperature T , the Boltzmann constant k_B , the magnetostatic constant μ_0 and the volume v of the particle. The detailed derivation of the diffusion constant D is illustrated in Appendix C. From the equation of motion (Eq. 3.46) the corresponding FP equation can be deduced to (details can be found in Appendix B)

$$\begin{aligned} \frac{\partial \rho}{\partial t} = & - \frac{\gamma}{1 + \alpha^2} \frac{\partial}{\partial \mathbf{M}} \cdot \left\{ \left[\mathbf{M} \times \frac{\partial V(\mathbf{M})}{\partial \mathbf{M}} + \frac{\alpha}{M_S} \mathbf{M} \times \left(\mathbf{M} \times \frac{\partial V(\mathbf{M})}{\partial \mathbf{M}} \right) \right. \right. \\ & \left. \left. + D \gamma \mu_0^2 \mathbf{M} \times \left(\mathbf{M} \times \frac{\partial}{\partial \mathbf{M}} \right) \right] \rho \right\}. \end{aligned} \quad (3.49)$$

Since the reduced magnetization is always unity in the LLG formulation ($\mathbf{m} = \frac{\mathbf{M}}{M_S} = 1$), the time evolution of the probability density of the magnetization on the unit sphere $\rho(t, \mathbf{m})$ becomes

$$\begin{aligned} \frac{\partial \rho}{\partial t} = & - \frac{\gamma'}{M_S} \frac{\partial}{\partial \mathbf{m}} \cdot \left\{ \left[\mathbf{m} \times \frac{\partial V}{\partial \mathbf{m}} + \alpha \mathbf{m} \times \left(\mathbf{m} \times \frac{\partial V}{\partial \mathbf{m}} \right) \right. \right. \\ & \left. \left. + \frac{\alpha}{\beta v} \mathbf{m} \times \left(\mathbf{m} \times \frac{\partial}{\partial \mathbf{m}} \right) \right] \rho \right\}, \end{aligned} \quad (3.50)$$

with $\gamma' = \frac{\gamma}{1+\alpha^2}$. Due to the symmetry of the problem Eq. 3.50 can be transformed to spherical coordinates

$$\begin{aligned} \frac{\partial \rho}{\partial t} = \frac{\alpha \gamma'}{\beta M_S v} \Lambda^2 \rho &+ \frac{\alpha \gamma'}{M_S \sin \theta} \frac{\partial}{\partial \theta} \left[\sin \theta \frac{\partial V}{\partial \theta} \rho + \frac{1}{\alpha} \frac{\partial V}{\partial \varphi} \rho \right] \\ &+ \frac{\alpha \gamma'}{M_S \sin \theta} \frac{\partial}{\partial \varphi} \left[\frac{1}{\sin \theta} \frac{\partial V}{\partial \varphi} \rho - \frac{1}{\alpha} \frac{\partial V}{\partial \theta} \rho \right], \end{aligned} \quad (3.51)$$

with

$$\Lambda^2 = \frac{1}{\sin \theta} \frac{\partial}{\partial \theta} \left(\sin \theta \frac{\partial}{\partial \theta} \right) + \frac{1}{\sin^2 \theta} \frac{\partial^2}{\partial \varphi^2}. \quad (3.52)$$

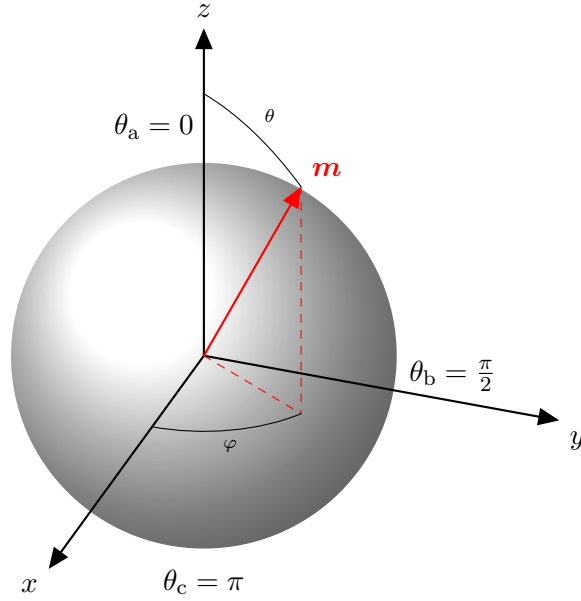


Figure 3.3: Reduced magnetization m in spherical coordinates. The energy minima θ_a and θ_c for an axially symmetric potential and the saddle point θ_b in case of a Gibbs free energy according to Eq. 3.61 are labeled.

3.3.1 Escape rate of superparamagnetic particles with axial symmetry

Brown [18] was the first to solve the escape rate problem for an axially symmetric Gibbs free energy density $V(\theta, \varphi) = V(\theta)$. Assuming a symmetry axis in the z -direction, the magnetization of a magnetic particle has two metastable states at $\theta_a = 0$ and $\theta_c = \pi$ (see Fig. 3.3), separated by an energy barrier. Hence, Eq. 3.51 reduces to

$$\frac{\partial \rho(\theta)}{\partial t} = \frac{\alpha \gamma'}{\beta M_S v \sin \theta} \frac{\partial}{\partial \theta} \left[\sin \theta \left(\frac{\partial \rho(\theta)}{\partial \theta} + \beta v \frac{\partial V(\theta)}{\partial \theta} \rho(\theta) \right) \right]. \quad (3.53)$$

This FP equation just depends on one variable, and thus can be solved independent of the friction of the system in contrast to the Kramers problem for mechanical particles. The azimuthal angle φ merely causes a steady precession of the magnetization

around the symmetry axis and does not influence the obtained escape rates. One can solve Eq. 3.53 very similarly to the low friction limit of the Kramers problem (see section 3.2.2), where the FP equation as well reduces to a differential equation in one variable, namely the energy or rather the action.

In the stationary case $\dot{\rho} = 0$ holds, and thus we can define the stationary probability flux over the energy barrier as

$$\begin{aligned} J_0 &= -\frac{2\pi\alpha\gamma'}{\beta M_S v} \sin \theta \left(\frac{\partial \rho}{\partial \theta} + \beta v \frac{\partial V}{\partial \theta} \rho \right) \\ &= -\frac{2\pi\alpha\gamma'}{\beta M_S v} \sin \theta \left[e^{-\beta v V} \frac{\partial}{\partial \theta} \left(e^{\beta v V} \rho \right) \right]. \end{aligned} \quad (3.54)$$

For the sake of clarity the total Gibbs free energy in units of the thermal energy is abbreviated with $\beta v V(\theta) = \eta(\theta)$ in the following. If there exists a sink for the magnetization after the barrier so that $\rho(\theta_b) = 0$ is valid, Eq. 3.54 can be integrated yielding the stationary probability density

$$\rho(\theta) = -\frac{J_0 M_S \beta v}{2\pi\alpha\gamma'} e^{-\eta(\theta)} \int_{\theta}^{\theta_b} \frac{e^{\eta(\theta')}}{\sin \theta'} d\theta'. \quad (3.55)$$

The number of particles in the metastable state a at $\theta_a = 0$ is

$$n_0 = 2\pi \int_0^{\theta_b} \rho(\theta) \sin \theta d\theta = -\frac{J_0 M_S \beta v}{\alpha\gamma'} \int_0^{\theta_b} e^{-\eta(\theta)} \sin \theta \int_{\theta}^{\theta_b} \frac{e^{\eta(\theta')}}{\sin \theta'} d\theta' d\theta. \quad (3.56)$$

Based on the flux over population method (Eq. 3.11) the inverse escape rate of the magnetic particle out of its metastable state becomes

$$k_{a \rightarrow c}^{-1} = \frac{n_0}{J_0} = \frac{M_S \beta v}{\alpha\gamma'} \int_0^{\theta_b} \frac{e^{\eta(\theta')}}{\sin \theta'} \int_0^{\theta'} e^{-\eta(\theta)} \sin \theta d\theta d\theta'. \quad (3.57)$$

In the last step additionally an integration by parts was performed. For high energy barriers ($\eta(\theta_b) - \eta(0) \gg 1$) the integrand of the second integral in Eq. 3.57 is only non-vanishing for small angles near the energy minimum at $\theta_a = 0$. The integral can be approximately extended to infinity and the Gibbs free energy is expanded in a Taylor series around $\theta_a = 0$

$$\int_0^{\theta'} e^{-\eta(\theta)} \sin \theta d\theta \approx \int_0^{\infty} e^{-\left(\eta(0) + \eta''(0) \frac{\theta^2}{2}\right)} \theta d\theta = \frac{e^{-\eta(0)}}{\eta''(0)}. \quad (3.58)$$

Likewise the remaining integral has its main contributions for large angles around the energy barrier, and thus it can be evaluated as

$$\int_0^{\theta_b} \frac{e^{\eta(\theta')}}{\sin \theta'} \approx \int_{-\infty}^{\theta_b} \frac{e^{\left(\eta(\theta_b) - |\eta''(\theta_b)| \frac{(\theta' - \theta_b)^2}{2}\right)}}{\sin \theta_b} d\theta' = \frac{e^{\eta(\theta_b)}}{\sin \theta_b} \sqrt{\frac{\pi}{2 |\eta''(\theta_b)|}}. \quad (3.59)$$

After inserting Eqs. 3.58 and 3.59 in Eq. 3.57 we obtain the escape rate to

$$k_{a \rightarrow c} = \frac{\alpha\gamma}{M_S \beta v (1 + \alpha^2)} \sqrt{\frac{2 |\eta''(\theta_b)|}{\pi}} \eta''(0) \sin \theta_b e^{-(\eta(\theta_b) - \eta(0))}. \quad (3.60)$$

Special case $H_{\text{ext}} = 0$

As a special case we consider a superparamagnetic single-spin particle with uniaxial anisotropy but without shape anisotropy and without external applied fields. The Gibbs free energy then has the simple form

$$\eta(\theta) = K_1 \beta v \sin^2 \theta, \quad (3.61)$$

with the uniaxial anisotropy constant K_1 . The saddle point of the energy landscape is located at $\theta_b = \frac{\pi}{2}$ yielding Brown's [18] asymptotic equation for the rate of magnetization reversal in a superparamagnetic particle

$$k_{a \rightarrow c} = \frac{1}{2} \frac{4\alpha\gamma}{M_S (1 + \alpha^2)} \sqrt{\frac{K_1^3 \beta v}{\pi}} e^{-K_1 \beta v}. \quad (3.62)$$

The leading factor $\frac{1}{2}$ arises from the fact that the magnetization vector has a 50% chance to cross the energy barrier in a real double-well potential as already pointed out in Sec. 3.2.2.

We have seen that under the restriction of an axial symmetric potential the switching rate of a particle's magnetization has a closed form for all values of the damping (friction) α , because the corresponding FP equation reduces to a differential equation in just one variable (Eq. 3.53). Brown already derived that fact in 1963 [18].

3.3.2 Escape rate of superparamagnetic particles without axial symmetry

In the more general case, where the Gibbs free energy density depends on both, the polar angle θ and the azimuthal angle φ , we have to solve the full FP equation (Eq. 3.51). Since the Hamiltonian of such a magnetic system is nonseparable, the longitudinal modes of motion dynamically couple to the transverse modes. As a consequence different damping regimes exist as for the mechanical particle (see Kramers problem Sec. 3.2):

- IHD regime for $\alpha \gtrsim 1$
- VLD regime for $\alpha \ll 1$
- turnover regime for $0.01 < \alpha \lesssim 1$

The IHD escape rate was first obtained by Brown [19] and Smith and de Rozario [20]. Assuming a Gibbs free energy in the form of a double-well potential with the shape of an elliptic paraboloid in the minima and a saddle point with the shape of a hyperbolic paraboloid, the free energy density can be expanded in a Taylor series around the stationary points

$$V = V_p + \frac{1}{2} [c_{1,p} u_{1,p}^2 + c_{2,p} u_{2,p}^2]. \quad (3.63)$$

In Eq. 3.63 $u_{i,p}$ are the direction cosines of the magnetization near the stationary points $\mathbf{m}_{p=a,b,c}$. Inserting the expanded potential into Eq. 3.51 allows to linearize the FP equation around the stationary points. The resulting equation can be solved, yielding the escape rate of the magnetization of a superparamagnetic particle from the a -well over the barrier with height $E_{ab} = v(V_b - V_a)$

$$k_{a \rightarrow c}^{\text{IHD}} = \frac{\Omega_b \omega_a}{\omega_b 2\pi} e^{-\beta E_{ab}}, \quad (3.64)$$

with the angular oscillation frequencies in the well a and at the saddle point b

$$\omega_a = \frac{\gamma}{\beta v M_S} \sqrt{c_{1,a} c_{2,a}}, \quad \omega_b = \frac{\gamma}{\beta v M_S} \sqrt{-c_{1,b} c_{2,b}}, \quad (3.65)$$

and the damped saddle angular frequency

$$\Omega_b = \frac{\gamma}{2\beta v M_S} \frac{\alpha}{1 + \alpha^2} \left[-c_{1,b} - c_{2,b} + \sqrt{(c_{2,b} - c_{1,b})^2 - \frac{4}{\alpha^2} c_{1,b} c_{2,b}} \right]. \quad (3.66)$$

For vanishing damping $\Omega_b \xrightarrow{\alpha=0} \omega_b$ is valid, and thus the escape rate becomes independent of the friction, which is obviously not correct analogous to Kramers solution for mechanical particles in the VLD regime.

Like in the case of mechanical particles the diffusion of the probability density in Eq. 3.51 is controlled by the energy at low damping. The magnetization dynamics are dominated by the first term on the right-hand side of the LLG equation (Eq. 3.46), which is the gyromagnetic equation causing a steady precession of the magnetization vector at constant energy in the absence of thermal forces. After a transformation to spherical coordinates the corresponding Hamiltonian still is nonseparable, and thus the magnetic problem still has a two dimensional state space. Nevertheless, it can be shown [21] that the VLD escape rate of superparamagnetic particles has the same form as for mechanical particles (Eq. 3.41)

$$k_{a \rightarrow c}^{\text{VLD}} = \alpha S_{ab} \frac{\omega_a}{2\pi} e^{-\beta E_{ab}}, \quad (3.67)$$

with

$$S_{ab} = \beta v \oint_{V_b} (1 - \cos^2 \theta) \frac{\partial V}{\partial \cos \theta} d\varphi - \frac{1}{1 - \cos^2 \theta} \frac{\partial V}{\partial \varphi} d(\cos \theta), \quad (3.68)$$

which is the action at the energy of the saddle point.

However, the most interesting damping regime for realistic magnetic systems is the turnover regime $0.01 < \alpha \lesssim 1$ connecting the VLD and IHD limits. Coffey et al. [22, 23] derived a turnover escape rate equation for superparamagnetic particles following the approach of Mel'nikov and Mehskov [14] for mechanical particles. One has to separate the full FP equation (Eq. 3.51) into a dissipative part and a part describing the undamped precessional motion of the magnetization. The dissipative FP equation is then

transformed from (θ, φ) to energy and azimuthal angle $(\beta E, \varphi)$ as variables. Assuming that the dissipation process just changes the energy of the system for a small amount in the barrier region, and hence the energy is a slow variable in contrast to φ , the dissipative FP equation can be simplified to the same form as Mel'nikov and Mehskov's energy action-diffusion equation for mechanical particles. It has to be pointed out that the so derived equation still depends on the azimuthal angle φ , ensuring a coupling between diffusion and dissipation terms even at low damping. Consequently the result of Eq. 3.45 can be adapted to express the escape rate of the magnetization of a superparamagnetic particle out of a double-well potential in the whole damping range

$$k_{a \rightarrow c} = \frac{A(\alpha S_{ab}) A(\alpha S_{cb})}{A(\alpha S_{ab} + \alpha S_{cb})} k_{a \rightarrow c}^{\text{IHD}}, \quad (3.69)$$

with the escape rate in the IHD regime of Eq. 3.64 and the depopulation factor $A(\Delta)$ of Eq. 3.44. S_{ab} and S_{cb} are again the action integrals at the different barrier heights from both wells of the potential. The IHD and VLD rates are perfectly reproduced because of the asymptotic behavior of the depopulation factor

$$A(\alpha S_i) \rightarrow \begin{cases} 1 & , \alpha \rightarrow \infty \\ \alpha S_i & , \alpha \rightarrow 0. \end{cases} \quad (3.70)$$

Special case with an external field perpendicular to the easy axis

The Gibbs free energy density of a superparamagnetic particle with uniaxial anisotropy subject to an homogeneous magnetic field with strength H perpendicular to the easy axis is

$$V(\theta, \varphi) = K_1 \sin^2 \theta - \mu_0 M_S H \sin \theta \cos \varphi. \quad (3.71)$$

In reduced energy and field units

$$\sigma = \beta K_1 v, \quad h = \frac{H}{H_{\text{ani}}} = \frac{\mu_0 M_S H}{2K_1}, \quad (3.72)$$

the dimensionless Gibbs free energy can be rewritten as

$$\beta v V(\theta, \varphi) = \sigma [\sin^2 \theta - 2h \sin \theta \cos \varphi]. \quad (3.73)$$

According to Kalmykov [24] this symmetric double-well potential allows some simplifications of Eq. 3.69 yielding

$$k_{a \rightarrow c} = \frac{A^2(\alpha S_{ab})}{A(2\alpha S_{ab})} \frac{\alpha}{1 + \alpha^2} \frac{\gamma K_1}{2M_S \pi} \left(1 - 2h + \sqrt{1 + \frac{4h(1-h)}{\alpha^2}} \right) \sqrt{\frac{1+h}{h}} e^{-\sigma(1-h)^2}, \quad (3.74)$$

with a Taylor series of S_{ab} around h

$$S_{ab} = \sigma \sqrt{h} \left(16 - \frac{104}{3}h + 22h^2 - 3h^3 + \frac{7}{24}h^4 + \frac{1}{16}h^5 + O(h^6) \right). \quad (3.75)$$

In the high barrier approximation $\sigma \gg 1$ (which is of course used for all derivations in this chapter so far) Eq. 3.74 holds for external fields obeying the condition $\frac{1}{4\sigma} < h < 1$. For reduced field parameters smaller than $\frac{1}{4\sigma}$ the Gibbs free energy only depends weakly on φ and the problem becomes almost axially symmetric. If $h > 1$ the potential loses its bistable character and the concept of an escape rate is not valid any more.

For further information about escape rates of mechanical particles the excellent review article by Hänggi et al. [13] is recommended. The detailed review by Coffey and Kalmykov [25] reveals further insight into the escape rate mechanisms of superparamagnetic particles.

Thermal stability of arbitrary magnetic microstructures

Portions of this chapter were previously published as [26, 27] and have been reproduced with permission of the coauthors and in accordance with the publisher's policy. Content which was not generated by the author of this thesis is explicitly denoted. Copyright of [26] is held by the American Physical Society.

4.1 Introduction

The prediction of the thermal stability of magnetic structures is important for numerous technological applications ranging from the design of magnetic recording structures and spin torque devices to the thermal decay of bulk permanent magnets [28, 29]. A detailed knowledge of thermally activated reversal processes in magnetic structures is also crucial for the understanding of coercivity as function of temperature and sweep rates [30]. In Sec. 3.3 we treated escape rates of simple superparamagnetic particles, which just consisted of one magnetic moment, and thus exchange interactions did not play a role. All so far derived escape equations in all damping regimes have in common the following basic form

$$k_{A \rightarrow B} = f_0 e^{-\frac{E_b}{k_B T}}. \quad (4.1)$$

This equation is known as Arrhenius-Nèel law. It identifies the escape rate constant $k_{A \rightarrow B}$ as product of a prefactor f_0 and an exponential function with the lowest energy barrier E_b separating the initial (meta)stable state from other long-lived states. In magnetism the prefactor is called attempt frequency, because the characteristic time

$\tau_0 = f_0^{-1}$ depends on the dynamics of the system and may be viewed as an attempt time to overcome the energy barrier.

While the thermally activated switching of single-domain particles has been studied exhaustively as documented in the literature [25] (see Sec. 3.3), there exists less work on the reversal of inhomogeneous magnetic structures. The thermal activation of domain walls was treated analytically for nanowires by Braun [31], for soft/hard nanowires by Loxely et al. [32] and for nanowires with graded anisotropy by Visscher et al. [33]. For more complicated structures, however, the activation energy cannot be computed analytically and one has to rely on numerical methods to determine the rate constant according to Eq. 4.1. Such a numerical computation can be performed in two steps. First, one determines the energy barrier E_b separating the long-lived states, for instance using the nudged elastic band method (NEB) or the string method [34, 35, 36, 37]. Then, one computes the prefactor f_0 , a calculation that is numerically very challenging and has been performed only recently for arbitrary magnetic microstructures [38].

Another strategy to calculate the thermal stability of magnetic nanostructures relies on the integration of the stochastic version of the Landau-Lifshitz-Gilbert equation. Such simulations, however, are restricted to several nanoseconds since small time steps are required to resolve the precessional motion [39, 40]. Simulations of this type can be extended to longer times using temperature accelerated dynamics [41, 42], which exploits the larger rate constant at higher temperatures, but reproduces the correct low-temperature behavior under the assumption that transition state theory holds. If this method is applied to the calculation of the switching rate of structures that are stable on the time scale of years, however temperatures well above the Curie temperature are required to obtain the necessary acceleration. While such high temperatures pose no difficulty for single-domain particles, this approach fails for spin systems, which are discretized in order to resolve domain walls. Also the bounce algorithm, in which the system is forced to stay in the high energy regions of configuration space, works best for single-domain particles [43].

In this work we apply the forward flux sampling method [44, 45], originally developed for the simulation of rare events in biochemical networks, to the simulation of switching processes in magnetic microstructures. This method, which has been successfully applied to study a variety of rare events ranging from crystal nucleation to protein folding, is based on a staging procedure that selectively generates transition pathways without the necessity to simulate the system during the long waiting time between the transitions. In contrast to other path based rare event simulation methods such as transition path sampling [46, 47, 48], forward flux sampling does not require knowledge of the stationary phase space density, such that it can be easily applied to non-equilibrium

systems. This feature makes the forward flux sampling methods also particularly suitable for the simulation of rare magnetic switching events in non-equilibrium situations, for instance in the presence of time varying external fields. Here, we use this approach to determine lifetimes of advanced recording media, demonstrating that a small coercive field can be combined with high thermal stability.

4.2 Magnetization dynamics

For the sake of clarity, we briefly recall the equation of motion of an arbitrary complex magnetic system, before addressing the forward flux sampling method. The magnetization dynamics of a magnetic particle at finite temperature can be described with the stochastic version of the Landau-Lifshitz-Gilbert (LLG) equation,

$$\begin{aligned} \frac{d\hat{\mathbf{m}}}{dt} = & - \frac{\gamma\mu_0}{1+\alpha^2} \{\hat{\mathbf{m}} \times (\mathbf{H}_{\text{eff}} + \boldsymbol{\xi})\} \\ & - \frac{\alpha\gamma\mu_0}{1+\alpha^2} \{\hat{\mathbf{m}} \times [\hat{\mathbf{m}} \times (\mathbf{H}_{\text{eff}} + \boldsymbol{\xi})]\}. \end{aligned} \quad (4.2)$$

Here, $\hat{\mathbf{m}}$ is the magnetization of the magnetic particle normalized by its saturation magnetization M_S , γ is the absolute value of the electron gyromagnetic ratio, μ_0 is the vacuum permeability and α is the damping parameter. In contrast to Eq. 3.46 we use the effective magnetic field in the above equation, which is calculated as the functional derivative of the total energy with respect to the magnetization

$$\mathbf{H}_{\text{eff}} = -\frac{1}{\mu_0 M_S} \frac{\delta E_{\text{tot}}}{\delta \hat{\mathbf{m}}}. \quad (4.3)$$

Since this equation is not a priori clear, the detailed derivation in continuous as well as in discrete systems is shown in Appendix D.

The thermal field $\boldsymbol{\xi}$ is an uncorrelated Gaussian random variable with zero mean and a variance of (see Appendix C)

$$\langle \xi_i(t, \mathbf{r}) \xi_j(t', \mathbf{r}') \rangle = \frac{2\alpha}{\gamma\mu_0^2 M_S \beta v} \delta_{ij} \delta(\mathbf{r} - \mathbf{r}') \delta(t - t'). \quad (4.4)$$

The total energy of the magnetic system is the sum of four contributions,

$$\begin{aligned} E_{\text{tot}} &= E_{\text{exc}} + E_{\text{ani}} + E_{\text{demag}} + E_{\text{zee}} \\ &= \frac{\mathcal{J}S^2c}{a} \int [(\nabla m_x)^2 + (\nabla m_y)^2 + (\nabla m_z)^2] dV \\ &\quad + \int K_1 [1 - (\hat{\mathbf{e}}_{\text{easy}} \cdot \hat{\mathbf{m}})^2] dV \\ &\quad - \frac{\mu_0 M_S}{2} \int \hat{\mathbf{m}} \cdot \mathbf{H}_{\text{demag}} dV \\ &\quad - \mu_0 M_S \int \hat{\mathbf{m}} \cdot \mathbf{H}_{\text{ext}} dV. \end{aligned} \quad (4.5)$$

The first term E_{exc} is the exchange energy, which arises from the exchange interactions between magnetic moments. If only nearest neighbor interactions are taken into account, the exchange integrals \mathcal{J} can be assumed as constant. In this simplification a is the lattice constant and $c = 1, 2$ and 4 for a simple cubic, bcc and fcc lattice, respectively. The anisotropy energy E_{ani} originates from the crystal structure of the particle, which gives the magnetic moments a preferred direction. Such directions are called “easy directions” and are described by the unit vector \hat{e}_{easy} . The constant K_1 in the second term is the anisotropy constant of the material. The third term E_{demag} represents the demagnetization energy, which arises because the demagnetization field $\mathbf{H}_{\text{demag}}$ of a magnetized structure tries to reduce its total magnetic moment by forming magnetic domains. The last term, the Zeeman energy E_{zee} , comes from the interaction of the magnetic moments of the system with an external magnetic field \mathbf{H}_{ext} .

Using a typical finite-element approach [6] with a semi-implicit time-integration schema [49], Eq. 4.2 can only be solved in the nanosecond time regime such that switching processes occurring on time scales of up to years are clearly out of reach of these simulations. But while such switching events, which determine the thermal stability of magnetic systems, are rare, they proceed rapidly once they are initiated through a rare but important fluctuation. This fact is exploited in forward flux sampling, which concentrates on dynamical trajectories that include the switching event as described in the next section.

4.3 Forward Flux Sampling (FFS)

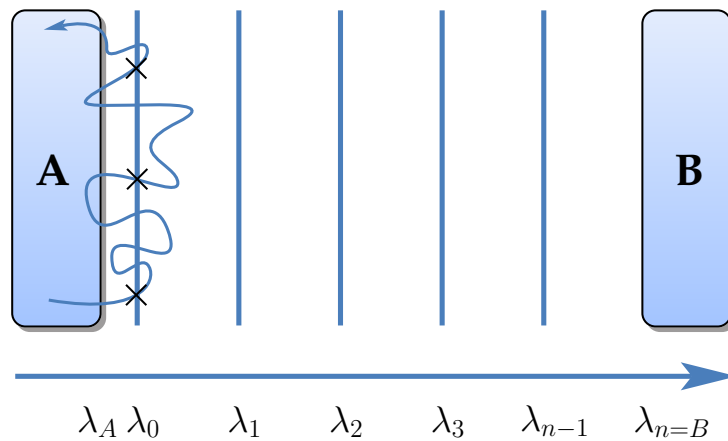


Figure 4.1: Schematic illustration of the stable states A and B and the interfaces λ_i , which partition the configuration space between A and B into adjacent regions. In the first stage of a forward flux sampling simulation one runs a trajectory starting in the stable state A . Each time the trajectory exits region A and successively crosses interface λ_0 , the system configuration is stored, as indicated by the crosses along λ_0 .

The forward flux sampling (FFS) method [44] is a computational method for calculating rate constants of rare events both, in equilibrium and non-equilibrium systems. In this method one considers rare transitions between long-lived states A and B , defined as regions in configuration space using an appropriate criterion. In between the states A and B one then arranges a sequence of non-overlapping interfaces defined as iso-surfaces of an order parameter, $\lambda(x) = \lambda_i$, as illustrated schematically in Fig. 4.1. The value of the order parameter has to increase at each subsequent interface in comparison to the previous one, $\lambda_{i+1} > \lambda_i$. Furthermore, the interfaces need to be defined such that a trajectory evolving from A to B crosses each interface at least once. Multiple recrossings of an interface are allowed.

Based on this setup the rate $k_{A \rightarrow B}$ for transitions from A to B can be computed from the following expression:

$$k_{A \rightarrow B} = \Phi_{A,0} P(\lambda_{n=B} | \lambda_0) = \Phi_{A,0} \prod_{i=0}^{n-1} P(\lambda_{i+1} | \lambda_i). \quad (4.6)$$

The first factor on the right-hand side of the equation $\Phi_{A,0}$ is the rate at which trajectories coming from region A cross interface λ_0 . The product following $\Phi_{A,0}$ is the probability that a trajectory crossing interface λ_0 reaches the final region B rather than returning to A first. Since this probability is small, it is written as product of conditional probabilities that are easier to calculate. In Eq. 4.6 $P(\lambda_{i+1} | \lambda_i)$ denotes the probability that a trajectory that has crossed interface λ_i will cross interface λ_{i+1} before returning to A .

The rate $k_{A \rightarrow B}$ is the escape rate of the system for leaving the metastable state A and ending up in the metastable state B . The relaxation rate $k_R = k_{A \rightarrow B} + k_{B \rightarrow A}$ is the sum of the escape rate $k_{A \rightarrow B}$ and the corresponding escape rate $k_{B \rightarrow A}$ of the reversed transition from state B to state A . All examples in this work are symmetric in the sense that both escape rates are the same, because transitions from A to B and vice versa are equally probable. In this case the relaxation rate k_R is simply twice the escape rate $k_R = 2k_{A \rightarrow B}$. If the free energy of state A is not equal to the energy of state B both escapes rates have to be determined with independent FFS simulations.

In the FFS method the factors appearing in Eq. 4.6 are computed as explained in the following. First, a Langevin simulation is carried out in the stable state A (see Fig. 4.1). Each time the Langevin trajectory exits region A and successively crosses interface λ_0 the system configuration is stored. This initial simulation ends after a given number N_0 of crossings is stored. Then, one of these sampled configurations is selected at random and serves as starting point for a new Langevin simulation (see Fig. 4.2). This simulation is terminated after the system either reaches the next interface λ_1 or returns to region A by crossing λ_A . If λ_1 has been reached, the system configuration at the cross-

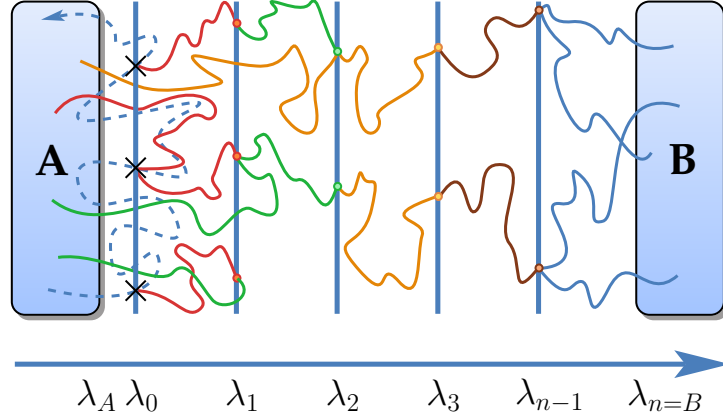


Figure 4.2: FFS algorithm: M_0 Langevin simulations are started from randomly chosen (previously stored) configurations at λ_0 . Each simulation is terminated when the trajectory crosses the next interface, λ_1 , or returns to A . This procedure is repeated at each interface until λ_n is reached.

ing point is again stored. To collect a set of configurations at interface λ_1 , this procedure is repeated M_0 times. From these configurations new Langevin trajectories are started and propagated until they cross the next interface λ_2 or return to A (not just to the previous interface!). For the subsequent interfaces one proceeds analogously. The whole procedure terminates successfully if at least one trajectory reaches the stable state B (crosses λ_n), or it terminates unsuccessfully if all trajectories coming from one of the interfaces return to A . In the first case a rare switching event has occurred, in the second case the choice of the interfaces has to be improved.

From the stored number of trajectories and the number of interface crossings the rate constant of the rare switching event is calculated using Eq. 4.6. The first factor on the right-hand side of Eq. 4.6 $\Phi_{A,0}$ is estimated as the number of stored configurations at interface λ_0 divided by the total time of the Langevin simulation in region A . The transition probabilities $P(\lambda_{i+1} | \lambda_i)$ appearing in the product are computed as the number of trajectories that cross interface λ_{i+1} divided by the total number of trial runs started at interface λ_i . Multiplication of these factors finally yields the transition rate constant $k_{A \rightarrow B}$.

The most important and also the most challenging part of a FFS simulation is the suitable definition of the interfaces between the two stable states. If the interfaces are not chosen appropriately, no single trajectory will reach the final state B within the given simulation time and the FFS method will not yield any result. Here, we propose to place the interfaces along the minimum energy path of the magnetization reversal process obtained using the nudged elastic band (NEB) method [34, 35, 36], as described in detail in Sec. 4.4.1. It has to be pointed out that the FFS algorithm is completely in-

dependent of the method used for placing the interfaces. Although the NEB method uses high damping to find energy minima and saddle points, the FFS method includes all dynamical effects of the system. The NEB method is just one very efficient way to arrange the interfaces between A and B . In principle, the results of forward flux sampling do not depend on the particular choice of the interfaces. However, not suitably chosen interfaces lead to a very poor efficiency of the method.

4.3.1 Error estimation

Despite the high efficiency of a forward flux sampling (FFS) simulation, compared to brute force calculations, it can still be computationally very expensive. Especially if a large amount of interfaces or many trial runs per interface are required to successfully obtain the rate constant of a rare event, an estimation of the expected error of the result is desirable. In addition, after a FFS simulation one is interested in the standard deviation of the computed rate. Hence, an analytical formula for the statistical error of $k_{A \rightarrow B}$ would be beneficial. We define \mathcal{V} as the relative variance in $k_{A \rightarrow B}$ per starting point at λ_0 . Relative variance means in this sense the total variance normalized by the square of the expectation value of the rate. It is assumed that the variance in $k_{A \rightarrow B}$ does not depend on $\Phi_{A,0}$ (see Eq. 4.6), which is the flux of trajectories out of the stable state A . This assumption usually holds for an appropriate definition of region A and sufficiently long simulation times in A to estimate $\Phi_{A,0}$ with high enough accuracy. Furthermore, the number of successful trial runs at different interfaces is supposed to be uncorrelated. In other words the chance to generate a successful trial run at interface λ_i does not influence the chance of a trial run to succeed at interface λ_{i+1} .

To simplify the notation in the following we define $P_B \equiv P(\lambda_n | \lambda_0)$, $p_i \equiv P(\lambda_{i+1} | \lambda_i)$ and $q_i \equiv 1 - p_i$ as well as $k_i \equiv M_i/N_0$ (ratio of the number of trial runs starting at interface λ_i and the number of configurations stored at λ_0). The relative variance of the transition rate constant is then given by

$$\mathcal{V} = N_0 \frac{V[P_B]}{P_B^2}. \quad (4.7)$$

The variance of P_B can be expressed in terms of the variance of the single transition probabilities p_i as follows

$$V[P_B] = V \left[\prod_{i=0}^{n-1} p_i \right] = \sum_{j=0}^{n-1} \left\{ \frac{\partial}{\partial p_j} \left(\prod_{i=0}^{n-1} p_i \right) \right\}^2 V[p_j]. \quad (4.8)$$

Here the error propagation formula

$$V[f(x_1, x_2, \dots, x_n)] = \sum_{i=1}^n \left(\frac{\partial f}{\partial x_i} \right)^2 V[x_i] \quad (4.9)$$

is used with $f(p_i) = \prod_{i=0}^{n-1} p_i$. $f(x_i)$ has to be a function of multiple uncorrelated variables and the partial derivatives are evaluated with all other variables at their mean values. Equation 4.8 simplifies to

$$V[P_B] = \sum_{j=0}^{n-1} \left(\frac{P_B}{p_j} \right)^2 V[p_j] = P_B^2 \sum_{j=0}^{n-1} \frac{V[p_j]}{p_j^2}. \quad (4.10)$$

The probability for a trial run to reach interface λ_{i+1} if started at interface λ_i is $p_i = \frac{N_s^{(i)}}{M_i}$, where $N_s^{(i)}$ is the number of successful trial runs. Since the number of started trajectories M_i is a constant, the variance of p_i becomes

$$V[p_i] = V \left[\frac{N_s^{(i)}}{M_i} \right] = \frac{V[N_s^{(i)}]}{M_i^2}. \quad (4.11)$$

In the last step again Eq. 4.9 is again used. According to Allen et al. [50] $N_s^{(i)}$ follows a binomial distribution, because it is the result of M_i discrete trials runs fired from interface λ_i , and thus

$$V[N_s^{(i)}] = M_i p_i q_i \quad (4.12)$$

is valid. Inserting Eqs. 4.12 and 4.11 in Eq. 4.10 yields

$$V[P_B] = P_B^2 \sum_{i=0}^{n-1} \frac{q_i}{M_i p_i}, \quad (4.13)$$

and the relative variance in $k_{A \rightarrow B}$ follows to

$$\mathcal{V} = N_0 \sum_{i=0}^{n-1} \frac{q_i}{M_i p_i} = \sum_{i=0}^{n-1} \frac{q_i}{k_i p_i}. \quad (4.14)$$

This equation holds as long as M_i is large enough that there exists at least one trajectory which is able to reach the next interface. Equation 4.14 is very helpful, because it allows to estimate the statistical error of a FFS simulation in advance just because of the predefined number of interfaces n , the number of trial runs at each interface M_i , the collection of N_0 stored states at λ_0 and the estimated transition probabilities p_i . After a successful simulation the p_i are known and the standard deviation of the transition rate, due to the statistical properties of a single FFS simulations, can simply be expressed as

$$\sigma = k_{A \rightarrow B} \sqrt{\frac{\mathcal{V}}{N_0}} = k_{A \rightarrow B} \sqrt{\sum_{i=0}^{n-1} \frac{q_i}{M_i p_i}}. \quad (4.15)$$

4.3.2 Optimization

Based on the relative variance \mathcal{V} Borrero and Escobedo [51] proposed an optimization method to increase the efficiency of the FFS algorithm. In this approach the variance

$V[P_B]$ is minimized under the constraint that the total transition probability P_B remains constant. This is done by varying Eq. 4.13 with an additional Lagrange multiplier α , which takes account for the constraint

$$\begin{aligned} \frac{\partial}{\partial p_j} \left\{ V[P_B] + \alpha \prod_{i=0}^{n-1} p_i \right\} &= \frac{\partial}{\partial p_j} \left\{ P_B^2 \sum_{i=0}^{n-1} \frac{1-p_i}{M_i p_i} + \alpha \prod_{i=0}^{n-1} p_i \right\} \\ &= -P_B^2 \frac{1}{M_j p_j^2} + \alpha \frac{P_B}{p_j} = 0, \end{aligned} \quad (4.16)$$

yielding the condition

$$M_j p_j = \frac{P_B}{\alpha} = \text{const.} \quad (4.17)$$

Equation 4.17 states that a constant flux of partial trajectories between the interfaces is optimal to minimize the variance in $k_{A \rightarrow B}$. Since merely the product of $M_i p_i$ has to be constant, the p_i are not fully specified, and thus one could postulate an arbitrary function. Without loss of generality we will choose a fixed value of M_i at all interfaces and a uniform distribution of the transition probabilities according to

$$p_i = (P_B)^{\frac{1}{n}}. \quad (4.18)$$

The only way to control the transition probabilities p_i after a FFS simulation is the replacement of the interfaces λ_i . To optimize the FFS calculation (minimize the variance in the resulting rate if the total computational effort remains unchanged) we need a function which interpolates between the old set of p_i and λ_i and a new set, where the interfaces are optimally placed, that $p_i = \text{const}$ holds. As proposed by Borrero and Escobedo [51] a possible choice for such a function is

$$f(\lambda_i) = \frac{\sum_{j=0}^{i-1} \ln p_j}{\sum_{j=0}^{n-1} \ln p_j}, \quad (4.19)$$

which reduces to

$$f(\lambda_i) = \frac{i}{n}, \quad (4.20)$$

for $p_i = \text{const}$. The function values at the interfaces should be equally spaced between $f(\lambda_0) = 0$ and $f(\lambda_n) = 1$. Figure 4.3 schematically illustrates the optimization procedure, which is summarized in the following:

- Perform a FFS simulation with not optimized interface positions and calculate the transition probabilities p_i .
- Construct an interpolation function $f(\lambda_i)$ with the p_i at each interface according to Eq. 4.19.
- Compute the new constant transition probabilities $p_i = (P_B)^{1/n}$, with the constraint that P_B remains constant.

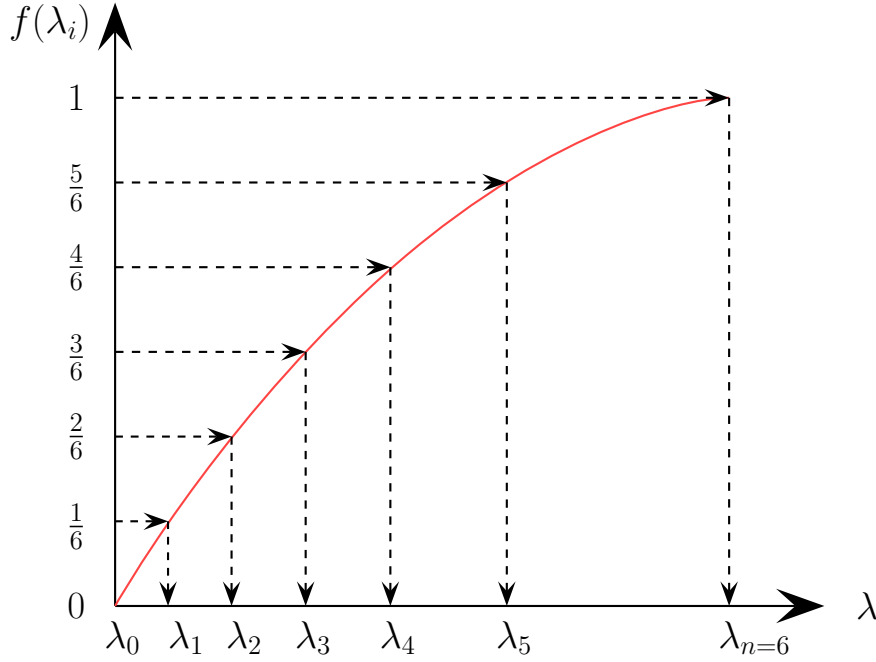


Figure 4.3: Schematic illustration of the optimization procedure to obtain a minimal variance in the FFS rate constant for a set of 7 interfaces. First, the interpolation curve (red) is evaluated according to Eq. 4.19 with the not optimized transition probabilities p_i . Under the constraint that the total transition probability P_B remains constant, the new interface positions are then determined for equally spaced function values $f(\lambda_i)$ according to Eq. 4.20 (dashed arrows).

- Use the interpolation function to determine an optimized set of interface positions λ_i , which corresponds to the values $f(\lambda_i) = \frac{i}{n}$.

This procedure can be iterated as often as necessary to finally obtain a FFS simulation with a constant flux of partial trajectories between all interfaces, and thus a rate constant $k_{A \rightarrow B}$ with minimal relative variance \mathcal{V} for a given computational effort.

In addition Ref. [51] presents another algorithm to optimize the number of trial runs at each interface M_i , which is not described here in detail, because it is not used within this work.

4.4 Illustrative Model

To demonstrate the application of the FFS approach in magnetic systems we compute the average lifetime of a single-macrospin particle with dimensions of $1 \times 1 \times 1 \text{ nm}^3$, which is described with one single spin. The particle has an anisotropy constant of $K_1 = 3 \text{ MJ/m}^3$, a saturation polarization of $\mu_0 M_S = 0.5 \text{ T}$ and its easy axis points in the z -direction. In addition, a homogeneous external magnetic field is applied along the

negative y -direction, which we will call the perpendicular external field in the following. The strength of the external field is given in reduced units

$$h = \frac{H_{\text{ext}}}{H_{\text{ani}}} = H_{\text{ext}} \frac{\mu_0 M_S}{2K_1}. \quad (4.21)$$

The magnetic dynamics of such a particle is fully specified by the vector magnetization $\hat{\mathbf{m}}(t)$ on the surface of the unit sphere in three dimensions as a function of time t . There are three reasons for using this simple superparamagnetic single-spin model:

- For the parameters considered here and for low energy barriers $E_b/k_B T < 10$, the magnetization reversal process can be monitored in one single direct Langevin simulation of length 10^4 ns. In this case it is possible to count the number of switches directly and from this number the thermal stability of the system (quantified by the average lifetime) can be computed. The results obtained in this way provide the basis to test the FFS approach.
- As illustrated in Sec. 3.3.2, Kalmykov [24] gives an analytical formula (Eq. 3.69) to compute the thermal stability of single-macrospin particles under the influence of arbitrary homogeneous magnetic fields, which offers another possibility of comparison.
- The model is very instructive because the magnetic configurations of such a particle can be visualized as normalized vectors moving on the unit sphere. Such a visualization is not possible with analogous hyper-vectors of a full micromagnetic model.

4.4.1 Interface Definition and Verification

In the first step of the FFS procedure the minimum energy path of the magnetization reversal is determined. Since our goal is to simulate a reversal from the magnetization-down to the magnetization-up state, the NEB calculation is carried out for start and end configurations with magnetizations in the $-z$ and $+z$ -direction, respectively. The NEB procedure then yields the minimum energy configurations ($\hat{\mathbf{m}}_A$ and $\hat{\mathbf{m}}_B$ in Fig. 4.4a) as well as intermediate configurations along the minimum energy path ($\hat{\mathbf{m}}_i$ in Fig. 4.4a). In general one configuration vector $\hat{\mathbf{m}}_i$ contains the spatial components of all K computational nodes in the finite element model of the underlying grain, and thus has $3K$ components. The illustrative model just consists of one spin, hence $K = 1$. Note that the magnetization in the energy minima does not point in the z -direction because of the perpendicular external applied magnetic field in y -direction. In the next step the interfaces λ_A and λ_B of the stable states A and B around the energy minima need to

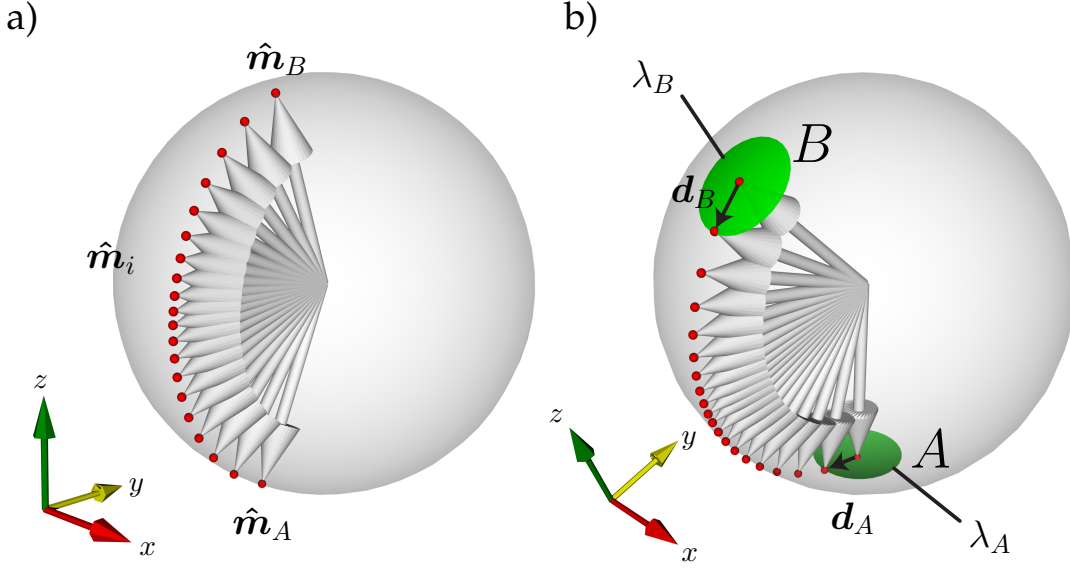


Figure 4.4: FFS interface definition for the single-macrospin model with a perpendicular external magnetic field applied in the negative y -direction. a) Minimum energy path of the magnetization reversal from \hat{m}_A to \hat{m}_B . b) Euclidean norm definition of the stable states A and B .

be properly defined (see Fig. 4.4b). We construct A and B by requiring that the deviation of the magnetization from the magnetization of the respective minimum energy configuration is smaller than a given value

$$\begin{aligned} \hat{m} \in A & \quad \text{if} \quad |\hat{m} - \hat{m}_A| = |d_A| \leq \lambda_A \\ \hat{m} \in B & \quad \text{if} \quad |\hat{m} - \hat{m}_B| = |d_B| \leq \lambda_B, \end{aligned} \quad (4.22)$$

where the vertical bars denote the Euclidean norm. It is important to choose the stable states A and B sufficiently narrow. Otherwise it may happen that a magnetization trajectory, which is only precessing around \hat{m}_B with a small opening angle, but which indeed returns to \hat{m}_A afterwards, is counted as a magnetic reversal trajectory (because it crossed the border interface λ_B). Such trajectories are known as ‘‘U-turns’’. In case of superparamagnetic particles they are frequently occurring error sources. If they are not correctly recognized, the rate constants are clearly overestimated. To obtain the correct rate constant it has to be ensured that $k_{A \rightarrow B}$ is independent of the chosen value of $\lambda_{A,B}$ for decreasing Euclidean norm threshold. This means that the rate constant should not change if the energy minimum definition is made even stricter. Simulations with too large $\lambda_{A,B}$ result in an overestimation of the rate constant, because ‘‘U-turns’’ are counted as magnetization reversals. This behavior is demonstrated in Fig. 4.5 for the illustrative model subject to a perpendicular external applied field with $h = 0.4$. It follows for all presented calculations: The definitions of the stable states A and B , and

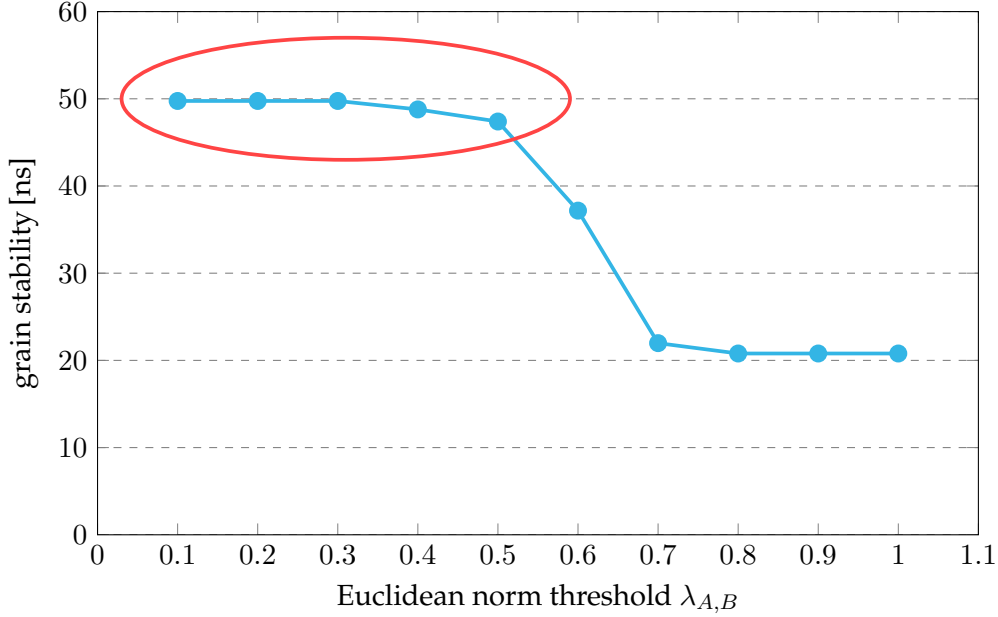


Figure 4.5: Grain stability of the illustrative model plotted against the Euclidean norm threshold $\lambda_{A,B}$, which is used to define the stable states A and B . A perpendicular external magnetic field with $h = 0.4$ is applied. In the marked area the evaluated grain stability is independent of the threshold value. Thus, it represents the “real” stability, which is not affected by “U-turns”.

thus the criteria for magnetization reversals, are suitable to guarantee that the system stays in a minimum, if its magnetization falls below $\lambda_{A,B}$ until a new rare event takes place. This holds for arbitrary damping of the system.

For the definition of interfaces λ_0 to λ_{n-1} we developed two different approaches, which are called hyperplane method and Euclidean norm method. We sequentially illustrate both approaches and present their verifications by comparing the obtained escape rates of the illustrative model with the corresponding analytical formula Eq. 3.74 for perpendicular external fields. If possible also results of direct Langevin simulations are presented.

Hyperplane method

As part of the hyperplane approach the difference vector \mathbf{n}_i of one magnetic configuration along the minimum energy path to the previous one is calculated

$$\mathbf{n}_i = \hat{\mathbf{m}}_i - \hat{\mathbf{m}}_{i-1}, \quad (4.23)$$

which is illustrated in Fig. 4.6a. Interface λ_i is then defined as the plane (or hyperplane if a full micromagnetic model is used) that passes through $\hat{\mathbf{m}}_i$ and is normal to \mathbf{n}_i . Note that in the string method the interfaces are also defined as hyperplanes normal to the string [35]. To decide whether an interface has been crossed, the position of the current

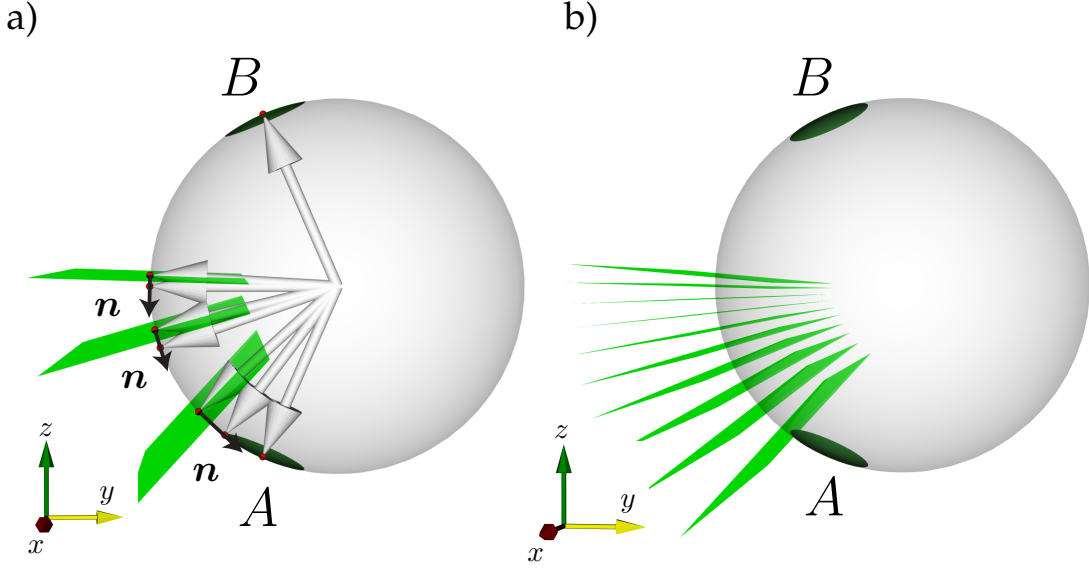


Figure 4.6: FFS hyperplane definition for the single-macrospin model with a perpendicular external magnetic field applied in the negative y -direction. a) Definition of the interfaces λ_0 to λ_{n-1} with hyperplanes. b) Overview of the final hyperplanes and stable states.

magnetization $\hat{\mathbf{m}}(t)$ vector relative to the hyperplane has to be determined. This can be done by computing the scalar product

$$\mathbf{n}_i \cdot [\hat{\mathbf{m}}(t) - \hat{\mathbf{m}}_i] \quad (4.24)$$

and checking its sign at each time step. The final interface definition of the hyperplane approach is shown in Fig. 4.6b.

In summary, stable states A and B are defined with the Euclidean distance to the minimum energy configurations. In between, hyperplanes are arranged along the minimum energy path. Note that there are only planes from region A up to the transition state of the magnetization reversal, because the probability of a trajectory starting from a hyperplane near the transition state to reach region B is sufficiently high. As a consequence, additional interfaces are not necessary and would only add to the computational cost, without improving the accuracy of the calculation.

Results

In a first verification step the simulation temperature and the external field strength are varied that the energy barrier has a constant value of $E_b/k_B T = 9$. Hence, the barrier is sufficiently small to observe several magnetization reversals even in a single direct Langevin simulation of length 10^4 ns. To detect a switch between the stable states in such a brute force calculation, the magnetization trajectory is followed on the surface of

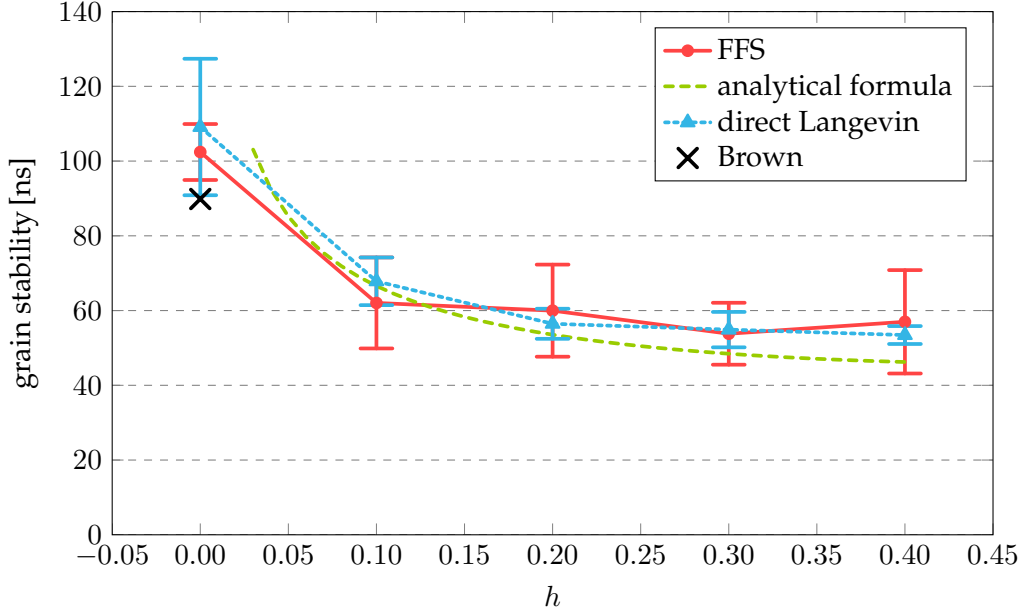


Figure 4.7: Thermal grain stability quantified by the average lifetime of the magnetic state for perpendicular homogeneous external magnetic fields with different field strengths. The FFS results (red solid line) and the direct Langevin simulation results (blue dotted line) are averages over five simulations. All simulations were performed with a damping constant of $\alpha = 0.02$. The error bars indicate the standard deviation σ_S of the attempt frequency based on repeated simulations with a certainty interval of 68.3%. The analytical behavior for the considered single-macrospin particle derived by Kalmykov [24] (Eq. 3.74) is shown as green dashed line. Brown’s [18] analytically calculated value at zero field (Eq. 3.62) is shown by a black x.

the unit sphere. The stable magnetic states are defined with the same Euclidean norm approach as used in FFS (see Sec. 4.4.1) with a threshold value of $\lambda_{A,B} = 0.5$. In the FFS method the stable states A and B are defined by the requirement that the Euclidean distance from the energy minima is less than 0.45. With these definitions the resulting rate constants are independent of the Euclidean norm threshold in both methods, as illustrated in Fig. 4.5. The rate constants thus arise purely from “real” magnetization reversals, which means that switched trajectories stay in their energy minima until a new rare switching event occurs. For both simulation methods a damping parameter of $\alpha = 0.02$ is used.

Thermal stabilities (quantified by average lifetimes) obtained from the direct Langevin simulations for perpendicular external fields with $0.0 \leq h \leq 0.4$ are shown in Fig. 4.7 as dotted blue line. For each field strength five Langevin simulations of 10^4 ns were carried out. The red solid line in Fig. 4.7 illustrates the thermal stability calculated with the FFS method with hyperplane interfaces. Mean values of again five simulations and the corresponding standard deviations are plotted. An optimization of the interface positions was performed for each field strength, such that the flux of partial trajecto-

$\frac{H_{ext}}{H_{ani}}$	\bar{p}_0	\bar{p}_1	\bar{p}_2	\bar{p}_3	$\bar{\tau}$ [ns]	\bar{f}_0 [GHz]	$\bar{\mathcal{V}}$	$\sigma_{\mathcal{V}}$ [GHz]	σ_S [GHz]
0.0	0.27	0.29	0.30	0.31	102.43	80.26	0.51	5.75	10.70
0.1	0.33	0.30	0.33	0.33	62.04	132.50	0.44	8.80	17.72
0.2	0.34	0.38	0.32	0.33	59.98	140.21	0.41	8.98	31.66
0.3	0.31	0.31	0.28	0.32	53.80	156.28	0.48	10.80	31.81
0.4	0.29	0.33	0.30	0.32	56.99	144.05	0.47	9.84	17.96

Table 4.1: FFS simulation results for perpendicular external fields with $0.0 \leq h \leq 0.4$. The crossing probabilities \bar{p}_0 to \bar{p}_3 , the lifetime $\bar{\tau}$, the prefactor (attempt frequency) \bar{f}_0 and the relative variance $\bar{\mathcal{V}}$ of \bar{f}_0 are average values over five separate simulations. σ_S is the standard deviation of \bar{f}_0 based on repeated FFS simulations and $\sigma_{\mathcal{V}}$ is estimated from the relative variance of the prefactor according to Eq. 4.25.

ries through all interfaces is nearly constant as described in Sec. 4.3.2. The results of these simulations are listed in Tab. 4.1. Crossing probabilities \bar{p}_i , lifetimes $\bar{\tau}$, prefactors (attempt frequencies) \bar{f}_0 and relative variances $\bar{\mathcal{V}}$ of \bar{f}_0 shown in the table are averages over five independent FFS simulations. Since the barrier is given, and thus has no error, the statistical error of the prefactor is evaluated based on Eq. 4.15 with

$$\sigma_{\mathcal{V}} = \bar{f}_0 \sqrt{\frac{\bar{\mathcal{V}}}{N_0}}. \quad (4.25)$$

In contrast σ_S is the standard deviation based on the repeated simulation. According to Fig. 4.7, FFS and direct Langevin calculations yield results that are identical up to their statistical errors. The green dashed line shows the thermal stability predicted by Kalmykov [24] (Eq. 3.74) for single-macrospin particles, which is only valid for $H_{ext} \geq 0.04H_{ani}$. Figure 4.7 proves that the simulations are in a good agreement with Kalmykov's analytical expression as well as with Brown's [18] formula (Eq. 3.62), which holds at zero field.

In a second verification step the illustrative model is investigated for different barrier heights ($9 \leq E_b/k_B T \leq 49$) but a fixed perpendicular external field with $h = 0.1$. Tab. 4.2 overviews the parameters and results of the corresponding FFS simulations. All FFS runs are optimized in terms of the algorithm presented in Sec. 4.3.2. For each barrier $E_b/k_B T$ five independent FFS calculations are performed. Fig. 4.8 illustrates that the FFS results again agree well with the analytical formula (Eq. 3.74). For better visualization the attempt frequency instead of the grain stability is shown in this plot, because the latter varies over several magnitudes due to the different energy barriers.

$E_b/k_B T$	n	\bar{p}_i (min-max)	\bar{f}_0 [GHz]	σ_γ [GHz]	σ_S [GHz]	CPU [h]
9	4	0.30 - 0.33	132.50	8.80	17.72	1
14	7	0.24 - 0.33	152.43	10.57	40.01	2
19	10	0.23 - 0.27	171.29	15.08	32.25	3
24	13	0.19 - 0.29	228.36	16.70	46.13	9
29	16	0.18 - 0.29	278.26	23.08	77.10	12
34	19	0.21 - 0.26	288.75	21.48	121.69	22
39	22	0.20 - 0.27	310.62	25.52	131.27	25
44	25	0.16 - 0.28	403.41	35.35	112.41	36
49	27	0.17 - 0.25	305.89	25.40	121.15	55

Table 4.2: Computational setup (number of interfaces n , range of average crossing probabilities \bar{p}_i) and results of FFS simulations with hyperplane interfaces (attempt frequency \bar{f}_0 , standard deviations σ_S, σ_γ and total simulation time in CPU hours) for different energy barriers $E_b/k_B T$ of the presented illustrative model. A perpendicular external magnetic field with $h = 0.1$ is applied. These are the FFS results of Fig. 4.8 in detail. Quantities with an overbar denote average values of five independent FFS simulations.

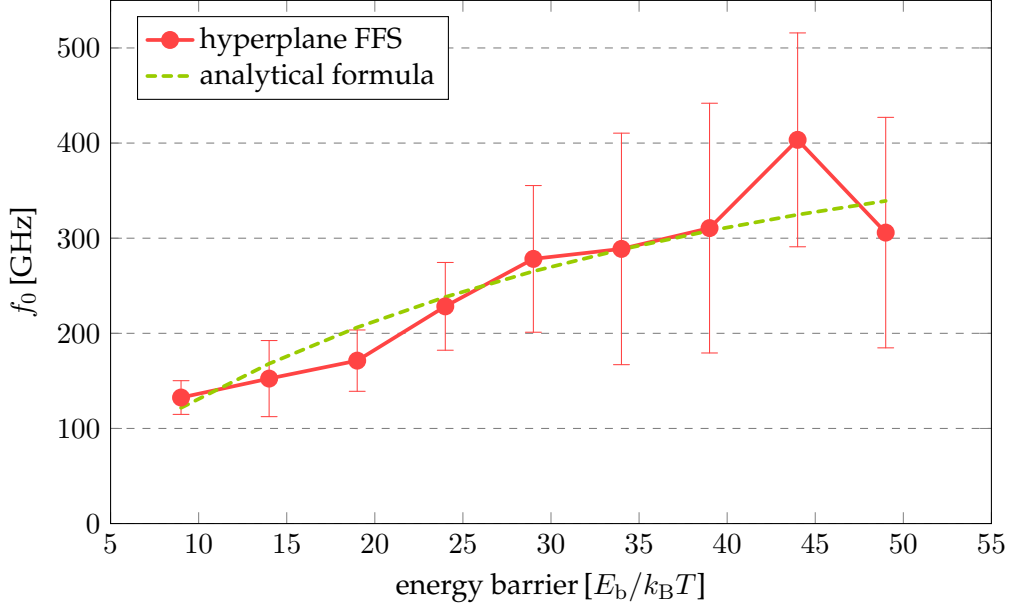


Figure 4.8: Attempt frequencies (prefactors of Eq. 4.1) of the illustrative single-macrospin model for different energy barriers $E_b/k_B T$. A perpendicular external magnetic field with $h = 0.1$ is applied. The FFS results (red solid line) are averages of five independent simulations and the error bars show the standard deviations σ_S of these repetitions (68.3% certainty). All detailed results can be found in Tab. 4.2. The analytically derived values according to Eq. 3.74 (green dashed line) agree well with the FFS results.

Euclidean norm method

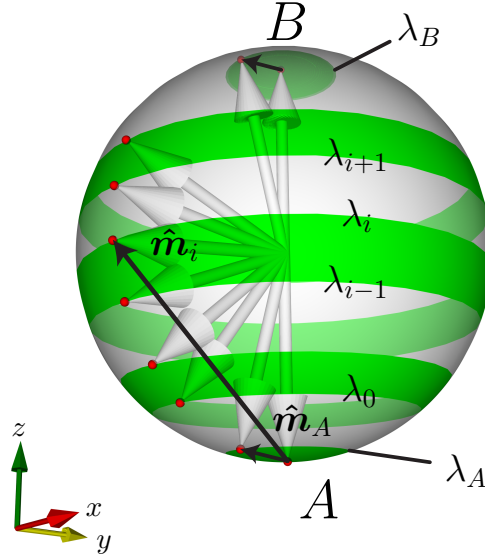


Figure 4.9: FFS Euclidean norm definition of the interfaces λ_i for the single-macrospin model subject to a perpendicular external magnetic field along the negative y -direction.

The second approach for the definition of the interfaces λ_i between the stable states A and B uses the Euclidean norm as follows

$$\lambda_i = |\hat{\mathbf{m}}_i - \hat{\mathbf{m}}_A| \quad \text{for} \quad 0 \leq i \leq n - 1. \quad (4.26)$$

Here the $\hat{\mathbf{m}}_i$ are again magnetic configurations along the minimum energy path obtained by the NEB method and $\hat{\mathbf{m}}_A$ is the minimum energy configuration of the initial state. Hence, the interfaces and the borders of the stable states A and B are uniformly specified by Euclidean norms of difference vectors of magnetic configurations as demonstrated in Fig. 4.9. One can check if an interface i is reached if $|\hat{\mathbf{m}} - \hat{\mathbf{m}}_A|$ exceeds the order parameter value λ_i at a given time step.

Results

$E_b/k_B T$	$n_{\text{interfaces}}$	\bar{p}_i (min-max)	\bar{f}_0 [GHz]	σ_γ [GHz]	σ_S [GHz]	CPU [h]
9	4	0.26 - 0.28	116.45	8.70	11.19	1
14	7	0.30 - 0.32	185.25	11.84	15.96	2
19	10	0.23 - 0.25	209.43	18.89	27.80	3
24	13	0.13 - 0.27	229.31	16.72	25.08	9
29	16	0.20 - 0.27	244.76	20.61	66.31	10
34	19	0.21 - 0.23	311.53	24.05	68.36	21
39	22	0.18 - 0.23	276.70	23.17	56.34	24
44	25	0.19 - 0.24	318.36	28.40	108.67	30
49	27	0.19 - 0.22	376.75	31.28	54.89	40

Table 4.3: Computational setup (number of interfaces $n_{\text{interfaces}}$, range of average crossing probabilities \bar{p}_i) and results of FFS simulations with Euclidean norm interfaces (attempt frequency \bar{f}_0 , standard deviations σ_S , σ_γ and total simulation times in CPU hours) for different energy barriers $E_b/k_B T$ of the presented illustrative model. A perpendicular external magnetic field with $h = 0.1$ is applied. These are the FFS results of Fig. 4.10 in detail. Quantities with an overbar denote average values of five independent FFS simulations.

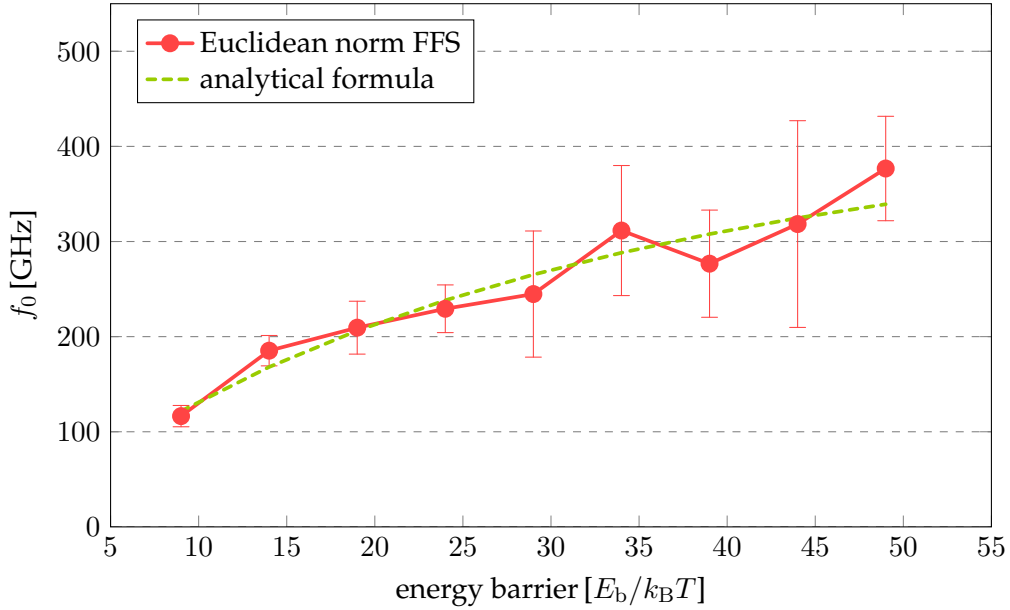


Figure 4.10: Attempt frequencies (prefactors of Eq. 4.1) of the illustrative single-macrospin model for different energy barriers $E_b/k_B T$. A perpendicular external magnetic field with $h = 0.1$ is applied. The FFS results (red solid line) are averages of five independent simulations and the error bars show the standard deviations σ_S of these repetitions (68.3% certainty). All detailed results can be found in Tab. 4.3. The analytically derived values according to Eq. 3.74 (green dashed line) agree well with the FFS results.

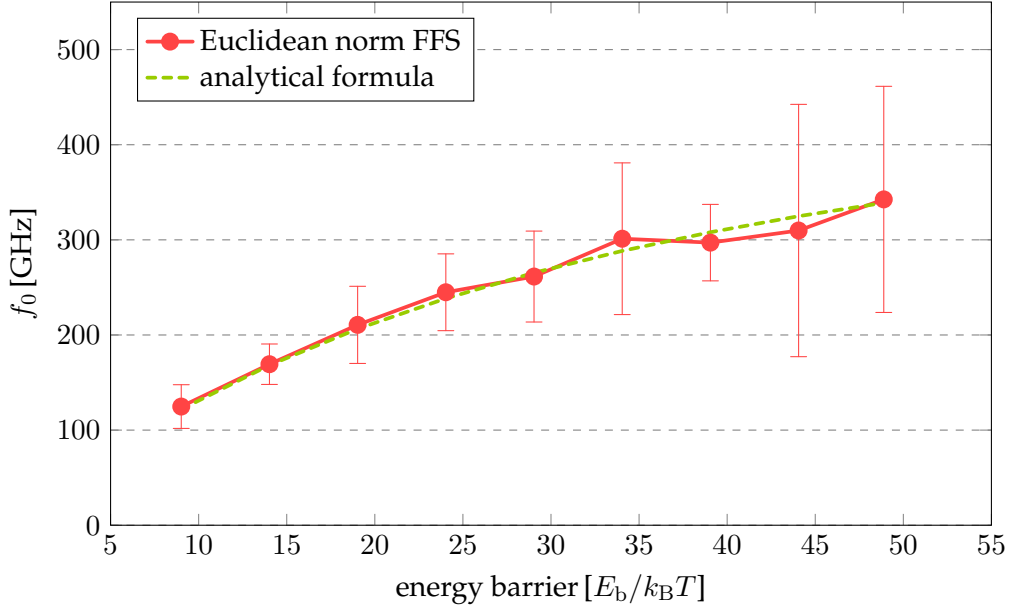


Figure 4.11: Same plot as Fig. 4.10 for an average of 15 FFS simulations for each value of $E_b/k_B T$.

In order to be able to compare the interface definition approaches we calculate thermal stabilities of the illustrative model for energy barriers in the range of $9 \leq E_b/k_B T \leq 49$, by varying the temperature of the FFS simulation at a fixed perpendicular external field with $h = 0.1$. The optimization procedure to obtain a constant flux of partial trajectories through all interfaces as described in Sec. 4.3.2 was again used. The results of five FFS simulations at each energy barrier are given in Tab. 4.3 and are shown in Fig. 4.10. The average attempt frequency \bar{f}_0 obtained by the Euclidean norm FFS method fits the analytical values again very well. However, the error bars, based on the repeated simulation, tend to be smaller than those of the hyperplane approach. For a total of 15 FFS simulations for each energy barrier $E_b/k_B T$ the averaged results almost reproduce the predicted analytical behavior perfectly as illustrated in Fig. 4.11.

4.4.2 Comparison of the computational efficiency

In this section we investigate the computational efficiency of all used simulation methods, which are the FFS approaches as well as the direct Langevin simulations. We start with a comparison of the computational effort in terms of used CPU hours on a single-core machine. After that the accuracy of the obtained rates (or grain stabilities) is discussed.

Since the direct calculation of thermal stabilities is impossible for energy barriers much larger than the thermal energy $k_B T$ we have to estimate its computational effort. We have to keep in mind that a sufficient number of spontaneous switches of the magne-

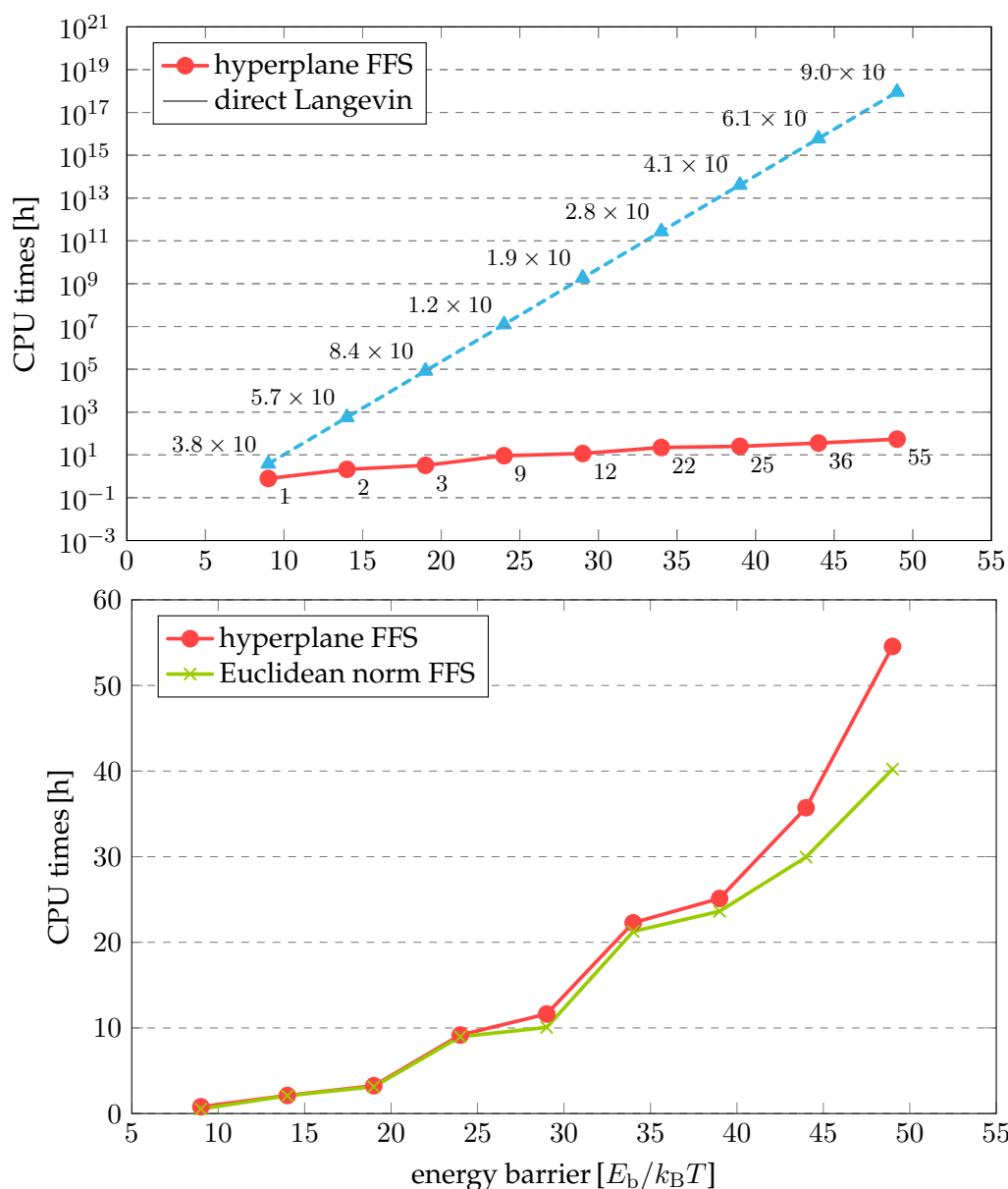


Figure 4.12: Total simulation times on a single-core machine for single-macrospin particles with different energy barriers. The simulation parameters are the same as those used to obtain the results shown in Figs. 4.8 and 4.10. For the direct simulation the required CPU time increases exponentially with increasing energy barrier E_b (blue dashed line extrapolated from a simulation with $E_b/k_B T = 9$). For the FFS method the total simulation time increases linearly with the number of interfaces and the number of trajectories per interface. In the upper plot direct Langevin calculations are opposed to hyperplane FFS simulations and in the lower plot the required computation time of both FFS approaches is compared.

tization has to be collected in order to ensure statistically significant results during a direct Langevin simulations. Therefore, the computational cost of a direct Langevin simulation increases exponentially with increasing energy barrier, as indicated in the upper plot of Fig. 4.12. The FFS approach, however, can deal with arbitrarily high

energetic barriers, and hence with very large lifetimes of magnetic states. The dependence of the required CPU hours with respect to the energy barrier (Fig. 4.12) can be explained as follows. For increasing energy barrier additional interfaces have to be inserted between the two stable states A and B to ensure that the crossing probabilities from one interface to the next remain approximately constant. The single Langevin trajectories used to compute the crossing probabilities have almost the same length for all energy barriers. They even get a bit shorter for increasing barrier heights, because the relaxation of the magnetization into the two energy minima becomes faster. As a consequence, the total simulation time increases almost linearly with the number of interfaces. An additional increase of CPU time is due to the larger number of trajectories generated at each interface (higher k_i) needed to keep the relative statistical variance \mathcal{V} constant (if p_i remains constant). The results shown in the upper plot of Fig. 4.12 imply that the total simulation times required by FFS and direct Langevin calculations are only comparable in the case of $E_b/k_B T = 9$. For a magnetic grain with a more realistic energy barrier it is not possible to determine the thermal stability with direct Langevin simulations, but with the FFS approach a calculation with good accuracy can be performed in less than 60 CPU hours on a single-core machine. Since all started trajectories at each interface are completely independent of each other they could be in principle parallelized with a perfect linear scaling.

The lower plot in Fig. 4.12 compares the computational cost of the two FFS approaches. Although the computation time is equal for low energy barriers the Euclidean norm method is significantly faster than the hyperplane method at very high barriers.

Concerning the accuracy of the computed rate constants (inverse thermal stabilities) Fig. 4.7 reveals that for energy barriers where direct Langevin simulations yield a result in a reasonable amount of time, the statistical error is comparable to that of FFS calculations. For higher fields the brute force variant has an error bar which is a bit more narrow, but the "real" thermal stability as obtained by Eq. 3.74 is not within one standard deviation for $h = 0.4$, in contrast to the FFS outcome. Comparing the computed attempt frequencies f_0 of the two FFS interface approaches in Figs. 4.8 and 4.10 one notices that the standard deviation based on the repeated simulation σ_S is smaller in the case of the Euclidean norm approach, especially at high energy barriers.

Since the transition probabilities p_i between the subsequent interfaces are optimized to be almost constant within all simulations and the k_i (number of trial runs per interface divided by the number of stored configurations at interface λ_0) are also the same in both FFS variants, the statistical variances \mathcal{V} , and thus $\sigma_{\mathcal{V}}$ are almost identical.

One point which should be mentioned is that in both FFS methods the standard deviation of the repeated simulations σ_S is significantly larger than the corresponding

standard deviation σ_V . A small mismatch can be explained by the fact that σ_V just accounts for statistical errors in the transition probabilities p_i between the FFS interfaces. The prefactor $\Phi_{A,0}$ in Eq. 4.6 is supposed to be exact, which is not completely true in our simulations. There are still small deviations of $\Phi_{A,0}$ between the repeated simulations. But these deviations are too small to explain the gap between σ_S and σ_V . Since the discrepancy increases for increasing energy barriers the reason could be, that the positions of the interfaces become too narrow. Equation 4.14 is only valid if the numbers of successful trial runs at subsequent interfaces are independent of each other, as mentioned in Sec. 4.3.1. This requirement could be violated for high energy barriers where the phase space is divided by many interfaces, because the precessional motion of the magnetization of the illustrative model just has two degrees of freedom. It is thus interesting if the mentioned mismatch is maintained for a full micromagnetic model with many degrees of freedom.

Summarized the Euclidean norm FFS approach is superior to the hyperplane FFS method in terms of the computational efficiency, at least in the context of the presented illustrative model. The former is faster and more accurate. Additionally the optimization algorithm introduced in Sec. 4.3.2 converges in less iteration steps in case of the Euclidean norm method. Within this procedure the interface positions have to be described with a scalar λ to construct an interpolation function between old and new positions. Hence, hyperplanes have to be represented by a scalar in each iteration, which makes the optimization procedure inefficient. On the top the Euclidean norm approach is contextually simpler, and thus easier to handle in practice. Nevertheless, the hyperplane method as well works flawlessly and may be preferable for some problems.

4.5 Graded media grains

Future magnetic recording devices will require high-coercivity materials such as FePt in order to insure thermal stability at high storage densities. However, the requirements of small volume (for high densities), low coercivity (for good writeability) and high thermal stability cannot be optimized at the same time using single phase grains, consisting of just one material. While the magnetic reversal of small grains of high-coercivity materials requires fields that exceed the capability of state-of-the-art magnetic write heads, small grains of low-coercivity materials have insufficient thermal stability. Recently, a new type of grain was proposed that is easily writeable and at the same time thermally stable even for small grain sizes [52, 53]. The grain consists of a stack of different materials with graded anisotropy, designed to overcome the superparamagnetic limit by reducing the coercive field while keeping a high barrier opposing spontaneous mag-

netization reversal. Calculations [36, 52, 53] carried out with the nudged elastic band (NEB) method [34] confirm a high energy barrier E_b for the magnetization reversal of such graded media grains with small volumes and low coercivity. Following the proposal of graded media grains, however, a controversy has arisen [54] on the value of the attempt frequency f_0 , which, together with the barrier height E_b , determines the thermal relaxation time $\tau = k_{A \rightarrow B}^{-1}$ according to the Arrhenius-Nèel law (Eq. 4.1). While one usually assumes that the attempt frequency is in the GHz range, it was suspected [54] that for graded media grains f_0 increases over many orders of magnitude, thus lowering the total thermal stability of graded media grains significantly despite the high energy barrier E_b . To reveal the full power of the FFS method we use it to compare the thermal stability of single phase and graded media grains, modeled fully micromagnetic. We prove that graded media grains are not restricted to the superparamagnetic limit, providing high density storage devices with low coercivity and at the same time high thermal stability.

We examine one graded media and two single phase grains of different magnetic anisotropy. The same model geometry, an elongated prism with a pentagonal basal plane, is used for all investigated grains. The prism has a height of 20 nm and the edge length of its basal plane is 3.53 nm. Based on its uniaxial anisotropy, the preferred magnetization direction of the particle points along the z -axis. Without the presence of an external magnetic field, the system has two energy minima with all magnetic moments aligned in the $\pm z$ -direction. The spatial discretization of the finite element calculations is the same for all models (54 nodes, 120 volume elements and 90 surface elements) as is the magnetic polarization $\mu_0 M_S = 0.5$ T, the exchange constant $A = 10^{-11}$ J/m and the damping constant $\alpha = 0.02$. Material and simulation parameters only differ in the profile of the anisotropy constant K_1 along the grains. While a single phase grain consists of just one material, the graded media grain consists of several materials with a quadratically increasing anisotropy constant, as proposed by Suess et al. [53].

In order to compare the different grain models regarding their applicability in real memory devices, we computed their coercive fields by analyzing the hysteresis loops of the grains determined in direct LLG simulations of the finite element model. The various coercive fields obtained from these calculations and the respective energy barriers of the magnetization reversals (obtained by the NEB method [34, 36]) are as follows. The graded media (GM) grain, which consists of 8 segments with a quadratically increasing anisotropy constant, $K_1(z) = z^2 \cdot 4.57 \times 10^{21}$ J/m⁵ has a coercive field of $\mu_0 H_C = 1.11$ T and an energy barrier of $E_b/k_B T = 53.2$. In addition we investigate a soft and a hard magnetic single phase (SmSP and HmSP) grain with anisotropies of $K_1 = 1.9 \times 10^5$ J/m³ and $K_1 = 6.61 \times 10^5$ J/m³, respectively. The SmSP grain has the

same coercive field ($\mu_0 H_C = 1.11$ T) as the graded media grain, but a significantly lower energy barrier of $E_b/k_B T = 22.47$. The HmSP grain has an energy barrier of

grain	K_1 [MJ/m ³]	$E_b/k_B T$	$\mu_0 H_C$ [T]
GM	0.0 – 1.4	53.62	1.11
SmSP	0.19	22.47	1.11
HmSP	0.661	53.78	3.30

Table 4.4: Comparison of the most important properties of the three investigated grain models. K_1 is the anisotropy constant, E_b the energy barrier (in units of $k_B T$) and $\mu_0 H_C$ the coercive field, obtained by simulated hysteresis loops. GM is the acronym for graded media, SmSP for soft magnetic single phase and HmSP for hard magnetic single phase.

$E_b/k_B T = 53.78$, which is comparable to that of the graded media grain, but has a significantly larger coercive field of $\mu_0 H_C = 3.3$ T. These properties are summarized in Tab. 4.4.

Using FFS, we next computed the magnetization reversal rates for the three different grains. Due to the high barrier of the GM grain 27 Euclidean norm interfaces between the magnetic stable states with magnetization-down (A) and magnetization-up (B) are required to determine its thermal stability at a temperature of 300 K. To estimate the accuracy of the computed rates, 10 FFS calculations with the same set of interfaces are performed. According to the optimization algorithm described in Sec. 4.3.2 the positions of the interfaces are arranged, in order to provide a constant flux of partial trajectories through the interfaces for each of the 10 simulations ($15\% \leq \bar{p}_i \leq 21\%$). Figure 4.13I illustrates some representatively chosen magnetic configurations along a transition path of the reversal process of the GM grain. The magnetic moments start to reverse in the upper soft magnetic part of the grain, while precessing around its easy axis (Fig. 4.13Ia). A domain wall then forms (Fig. 4.13Ib) and moves downwards to the hard magnetic parts of the grain (Fig. 4.13Ic-d), until all magnetic moments are finally reversed (Fig. 4.13Ie) and the particle reaches the opposite (meta)stable state. After averaging over all 10 repeated FFS simulations the mean attempt frequency of the magnetic transition becomes $\bar{f}_0 = 8893.14$ GHz, yielding an average grain stability of $\tau = 718.07$ years. The standard deviation of f_0 , estimated based on the repeated simulations, is $\sigma_S = 1997.95$ GHz. One single FFS simulation required an average of 21392.4 CPU hours. For a certainty interval of 99.7% ($3\sigma_S$), the GM grain is stable for at least 412.77 years. The corresponding standard deviations σ_V obtained from the single FFS simulations have a range of $602.80 \text{ GHz} \leq \sigma_V \leq 1265.17 \text{ GHz}$, which is in the order of magnitude of the standard deviation estimate based on the repeated FFS simulations, $\sigma_S = 1997.95$ GHz.

It seems that the interfaces in this full micromagnetic model with many degrees of free-

dom are not placed too narrow and the number of successful trial runs at an interface is independent of the corresponding number at the previous interface. Under these conditions the equation for the relative statistical variance \mathcal{V} (Eq. 4.14) by Allen et al. [50] holds, and thus the error estimation is valid in contrast to the case of high energy barriers of the illustrative model, as discussed in Sec. 4.4.2. Hence, repeating FFS simulations with the same setup provides no additional information on the error of the rate, as the statistical properties of a single FFS simulation already allow for a reliable error estimation. For this reason, only single simulations are discussed from this point on.

Although the SmSP grain has the same coercivity as the GM grain, due to the lower energy barrier only 11 Euclidean norm interfaces are required in the FFS simulation of the SmSP grain. Also in this case the positions of the interfaces are optimized to produce a constant flux of partial trajectories ($17\% \leq p_i \leq 20\%$). A typical magnetization reversal path of the SmSp grain, obtained at a temperature of 300 K, is shown in Figs. 4.13IIa-e. The difference to the transition path of the GM grain (Fig. 4.13I) is obvious. As demonstrated in Fig. 4.13IIa, the magnetic moments in all parts of the SmSP grain start to precess around the easy axis of the grain. In the course of the transition, depicted in Figs. 4.13IIb-e, the magnetic moments reverse almost homogeneously just like the moments in a single-domain particle. The FFS simulation of the SmSP grain yields an attempt frequency of $f_0 = 288.79$ GHz corresponding to a thermal stability of $\tau = 19.81$ ms. The relative accuracy of the attempt frequency is the same as that of the GM grain.

Finally we carried out an FFS simulation for the HmSP grain, which has the same energy barrier as the GM grain, but a much higher coercive field. The FFS simulation at a temperature of 300 K requires 29 Euclidean norm interfaces and the optimized partial flux of trajectories ranges from 18% to 24%. The whole FFS simulation required 11255.27 CPU hours. The mechanism for the magnetization reversal is similar to that of the GM grain. Inspecting a typical transition path in Fig. 4.13IIIa-e, we notice that the reversal of the magnetic moments starts at one end of the grain (Fig. 4.13IIIa). Then a domain wall forms (Fig. 4.13IIIb) and propagates through the prism (Fig. 4.13IIIc-d), until it is completed (Fig. 4.13IIIe). Because of the symmetry of the system, it is equally probable for the domain wall to arise in the lower part of the particle as in the upper part, which is a main difference to the transition in the GM grain. The computed attempt frequency of the rare event is $f_0 = 6560.08$ GHz, yielding a thermal stability of $\tau = 1099.90$ years.

Table 4.5 summarizes the most important similarities and differences of the graded media grain and the two single phase grains with the same geometry. If one asks for a magnetic particle with low coercivity, one might expect that the GM grain or the SmSP

grain	f_0 [GHz]	τ	σ_V [GHz]	CPU [h]
GM	8893.14	718.07 <i>a</i>	825.90	21392.4
SmSP	288.79	19.81 <i>ms</i>	17.31	6727.1
HmS	6560.08	1099.90 <i>a</i>	613.57	11255.3

Table 4.5: FFS results for the graded media (GM) grain, the soft magnetic single phase (SmSP) grain and the hard magnetic single phase (HmSP) grain. Here, f_0 is the attempt frequency, τ the grain lifetime and σ_V is the standard deviation of f_0 , computed according to Eq. 4.25. The last column contains the CPU hours used in the FFS simulations. The GM grain results are averages over 10 repeated FFS simulations.

grain to be a good choice (see Tab. 4.4). By looking at the thermal stabilities, however, it is obvious that the SmSP grain could never be used in a storage device, because it changes its magnetic state about 50 times per second (at 300 K) on the average. In contrast, the GM grain has excellent thermal stability with a reversal rate of one per about 700 years. Comparing single phase with graded architecture (with the same energy barrier), the thermal stability of the HmSP grain is slightly higher, but its coercive field is much larger. Graded media grains can combine both, low coercivity and high thermal stability, and thus are able to overcome the superparamagnetic limit.

It has to be emphasized that the rate constants presented are only qualitatively correct, meaning that the relative values of the thermal escape rates are accurate, but their absolute values depend on the spatial discretization length scale used in the finite element model of the particles. Since the strength of the thermal field ξ in Eq. 4.2 is dependent on the discretization volume, the magnetization dynamics of the underlying grains are also mesh size dependent. In principle, an atomistic discretization should produce the correct dynamics, and thus the correct escape rates. Nevertheless, the conclusions that

- a graded media grain with the same energy barrier as a single phase grain has a significantly lower coercive field
- a graded media grain with the same coercive field as a single phase grain has a significantly larger thermal stability

remains valid.

In summary, we have proven for the first time, using forward flux sampling, that the concept of magnetic grains with graded anisotropy provides very small nanostructures with high thermal stability and low coercivity. The results are obtained without any free parameters by directly integrating the underlying equation of motion (Eq. 4.2). Due to the quadratically increasing anisotropy the grains combine the desired properties of both, soft and hard magnetic parts, without suffering from their disadvantages.

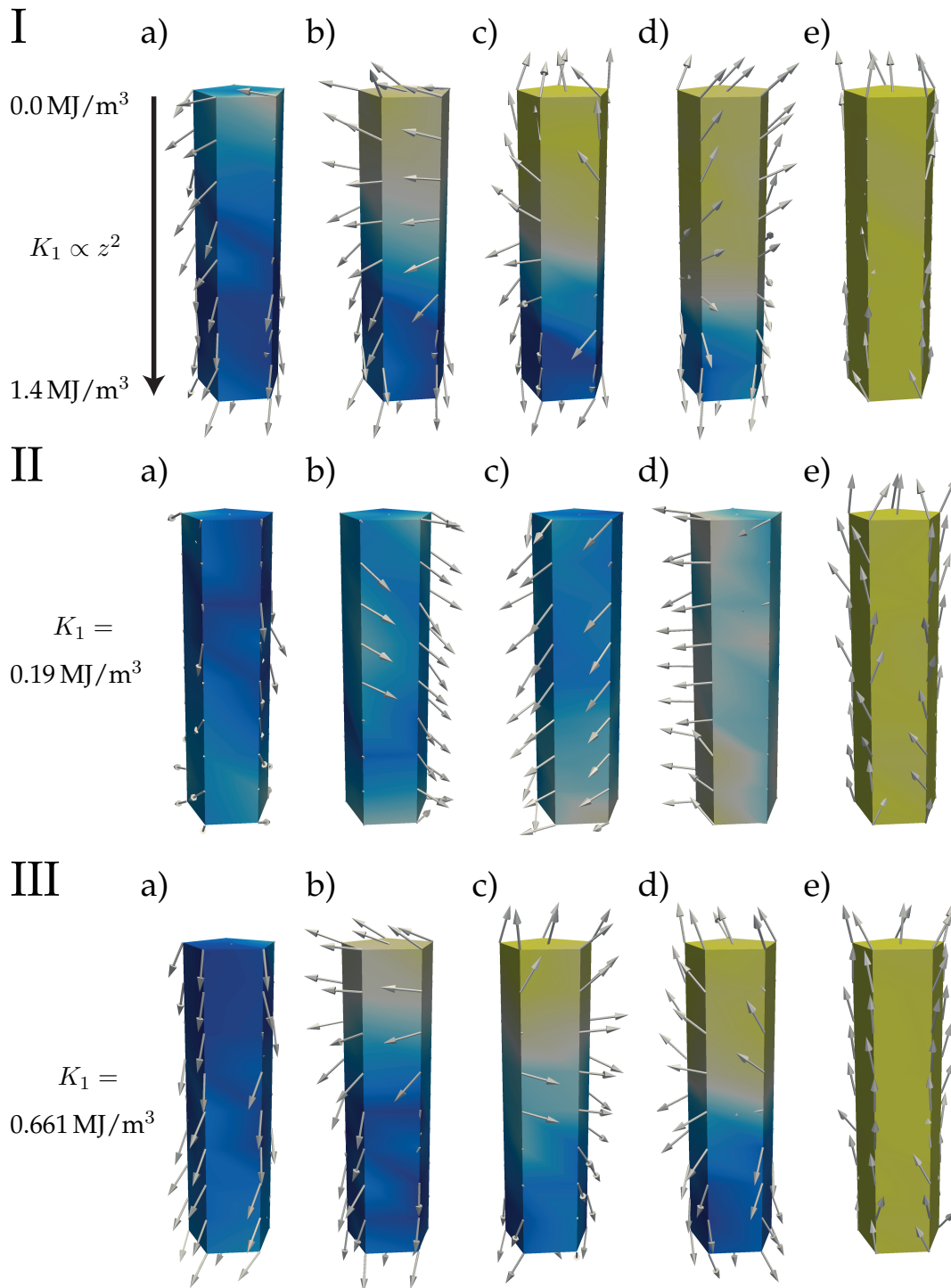


Figure 4.13: Exemplarily chosen magnetic configurations along the transition paths of thermally activated magnetization reversals of the investigated I) graded media (GM) grain, II) soft magnetic single phase (SmSP) grain and III) hard magnetic single phase (HmSP) grain, at a temperature of 300 K. The GM grain has an anisotropy constant $K_1(z) \propto z^2$ increasing quadratically along the grain from zero to a maximum of $K_{1,\max} = 1.4 \text{ MJ/m}^3$, as displayed in I). The colors on the grains indicate the average normalized z -component of the magnetization.

Heat-assisted recording

Portions of this chapter were previously published as [55] and have been reproduced with permission of the coauthors and in accordance with the publisher's policy. Content which was not generated by the author of this thesis is explicitly denoted. Copyright is held by the American Physical Society.

5.1 Introduction

Over the past decades the areal storage density of hard disk drives (HDDs) continuously increased [56]. In order to keep up this increase, many inventions on both sides, the magnetic write head and the recording medium were necessary. One of the first improvements beyond the pure scaling of all involved parts of a HDD was the introduction of anisotropic magnetoresistive write heads. A significant increase in the sensitivity of magnetic heads became possible due to the discovery of the effect of giant magnetoresistance [57, 58], which is the basis for all modern magnetic read heads. Concerning the recording medium, where all information is written and stored, the invention of antiferromagnetic coupled media and especially the transition from longitudinal to perpendicular recording [59, 60] have to be mentioned. A recent improvement [52] uses recording grains consisting of many different materials with graded anisotropy instead of grains with single phases. Nevertheless, the areal storage density increase of HDDs slowed down with the state-of-the-art recording techniques. With decreasing particle size, magnetically harder recording grains have to be used in order that the stored information remains thermally stable. In principle, the magnetic field required to write a graded media grain can be arbitrarily reduced with enough layers. However, it is technically not possible to produce such grains with a continuous change of their anisotropy constant.

Heat-assisted recording [61, 62, 63, 64, 65] could be the next step to provide a further increase in the areal storage density of HDDs. In this technique the recording medium is locally heated near to or above the Curie temperature T_C to be able to reverse the magnetic moments of recording grains with very high coercivity, like FePt. In combination with an additional write assistance of grains with graded Curie temperatures [66], the further continuous increase of the areal storage density of HDDs is trusted for the next years.

There are several ways to handle the effect of temperature in micromagnetism. The most common way to account for thermal fluctuations, acting on the magnetic moments of a ferromagnetic particle, is to incorporate a random thermal field in the equation of motion. At zero temperature the integration of the Landau-Lifshitz-Gilbert (LLG) equation is an established method to describe magnetization dynamics. One problem of the LLG equation is, that the magnetization length is proposed to be fixed, independent of temperature. Once the spatial discretization of a ferromagnetic particle is not atomistic, this restriction is wrong at high temperatures, because the phase transition from the ferromagnetic state to the paramagnetic state at the Curie temperature cannot be modeled in each macroscopic simulation cell. It is well known from molecular field theory that the length of the total magnetization of an ensemble of magnetic moments decreases with increasing temperature and finally ends up with zero length at T_C . Hence, a powerful high-temperature micromagnetic equation should reproduce this behavior in each computational cell. The Landau-Lifshitz-Bloch (LLB) equation derived by Garanin [67] fulfills the requirement and the absolute value of the magnetization is no longer a constant. It links between the LLG equation at low temperatures and the Bloch equation at high temperatures. Since in an atomistic LLG model each atom of a magnetic particle has to be described with one spin the simulation already becomes computationally very expensive for small grains with lateral dimensions of a few nanometers. In contrast, the LLB equation makes it possible to compute large areas of a particle, or even the whole grain, with just one magnetic moment. Hence, LLB simulations are very fast compared to their atomistic LLG counterparts. As a result, bit error rates of magnetic grains with realistic dimensions can be computed, which would not be possible with atomistic LLG calculations.

5.2 Dynamic equations

As already mentioned, the Landau-Lifshitz-Bloch (LLB) equation describes the magnetization dynamics of magnetic particles at high temperatures without the restriction of a fixed magnetization length, and thus allows for its longitudinal relaxation. The valid-

ity of the LLB was already proven in various publications [68, 69, 70, 71, 69, 72, 73, 74, 75, 76, 77]. In its most recent formulation [74], it has the form

$$\begin{aligned} \frac{d\mathbf{m}}{dt} = & - \mu_0 \gamma' (\mathbf{m} \times \mathbf{H}_{\text{eff}}) \\ & - \frac{\alpha_{\perp} \mu_0 \gamma'}{m^2} \{ \mathbf{m} \times [\mathbf{m} \times (\mathbf{H}_{\text{eff}} + \boldsymbol{\xi}_{\perp})] \} \\ & + \frac{\alpha_{\parallel} \mu_0 \gamma'}{m^2} \mathbf{m} (\mathbf{m} \cdot \mathbf{H}_{\text{eff}}) + \boldsymbol{\xi}_{\parallel}, \end{aligned} \quad (5.1)$$

where γ' is the reduced electron gyromagnetic ratio ($\gamma' = |\gamma_e|/(1 + \lambda^2)$, with $|\gamma_e| = 1.760859708 \cdot 10^{11} \text{ (Ts)}^{-1}$), μ_0 is the vacuum permeability and \mathbf{m} is the reduced magnetization \mathbf{M}/M_0 , with the saturation magnetization at zero temperature M_0 . In addition α_{\parallel} and α_{\perp} are dimensionless temperature-dependent longitudinal and transverse damping parameters given by

$$\alpha_{\perp} = \begin{cases} \lambda \left(1 - \frac{T}{T_C}\right) & T < T_C \\ \alpha_{\parallel} & T \geq T_C \end{cases}, \quad \alpha_{\parallel} = \lambda \frac{2T}{3T_C}. \quad (5.2)$$

The coupling of the spin to the heat bath on an atomistic level is described by λ . T_C donates the Curie temperature. The longitudinal and perpendicular thermal fields are denoted with $\eta = \parallel$ and $\eta = \perp$, respectively. $\boldsymbol{\xi}_{\eta}$ consist of white noise random numbers with zero mean and a variance of

$$\langle \xi_{\eta,i}(t, \mathbf{r}) \xi_{\eta,j}(t', \mathbf{r}') \rangle = 2D_{\eta} \delta_{ij} \delta(\mathbf{r} - \mathbf{r}') \delta(t - t'), \quad (5.3)$$

where the diffusion constants D_{η} are given by

$$\begin{aligned} D_{\perp} &= \frac{(\alpha_{\perp} - \alpha_{\parallel}) k_B T}{\gamma' \mu_0^2 M_0 V \alpha_{\perp}^2}, \\ D_{\parallel} &= \frac{\alpha_{\parallel} \gamma' k_B T}{M_0 V}. \end{aligned} \quad (5.4)$$

The detailed derivation of D_{\perp} and D_{\parallel} is illustrated in Appendix F. The effective magnetic field \mathbf{H}_{eff} in Eq. 5.1 consists of four contributions in our model. Besides the external field \mathbf{H}_{ext} , it contains the intergrain exchange field \mathbf{H}_{ex} , which is discussed in more detail in Sec. 5.5, the anisotropy field \mathbf{H}_{ani} and the internal exchange field \mathbf{H}_{J} ,

$$\mathbf{H}_{\text{eff}} = \mathbf{H}_{\text{ext}} + \mathbf{H}_{\text{ex}} + \mathbf{H}_{\text{ani}} + \mathbf{H}_{\text{J}}. \quad (5.5)$$

For the anisotropy field we use the compact form

$$\mathbf{H}_{\text{ani}} = \frac{1}{\tilde{\chi}_{\perp}} (m_x \mathbf{e}_x + m_y \mathbf{e}_y), \quad (5.6)$$

with the perpendicular susceptibility $\tilde{\chi}_{\perp}$. Here it is assumed that the easy axis, arising from the uniaxial anisotropy of the crystal structure, points along the z -direction. Since

the anisotropy constant K_1 and the magnetization M are both temperature-dependent, $\tilde{\chi}_\perp$ is also a function of temperature. Two further temperature-dependent material functions appear in the internal exchange field \mathbf{H}_J , controlling the length of the magnetization, which is defined as

$$\mathbf{H}_J = \begin{cases} \frac{1}{2\tilde{\chi}_\parallel} \left(1 - \frac{m^2}{m_e^2}\right) \mathbf{m} & T \lesssim T_C \\ -\frac{1}{\tilde{\chi}_\parallel} \left(1 + \frac{3}{5} \frac{T_C}{T-T_C} m^2\right) \mathbf{m} & T \gtrsim T_C. \end{cases} \quad (5.7)$$

In this equation m_e is the zero-field-reduced equilibrium magnetization. The perpendicular and longitudinal susceptibilities are specified as

$$\tilde{\chi}_\eta = \left(\frac{dm_\eta}{dB_{\text{ext},\eta}} \right)_{B_{\text{ext},\eta} \rightarrow 0}. \quad (5.8)$$

To integrate the LLB equation at arbitrary temperatures, the detailed temperature dependence of m_e , $\tilde{\chi}_\parallel$ and $\tilde{\chi}_\perp$ has to be known. LLG simulations with an atomistic spatial discretization of the underlying ferromagnetic particle as well as a mean-field ansatz can be used for this purpose.

For the atomistic approach we use the LLG code VAMPIRE [78], where the dynamic equation of motion is implemented as follows

$$\begin{aligned} \frac{d\mathbf{S}_k}{dt} = & - \gamma' \{ \mathbf{S}_k \times (\mathbf{H}_{\text{eff},k} + \boldsymbol{\xi}_k) \} \\ & - \gamma' \lambda \{ \mathbf{S}_k \times [\mathbf{S}_k \times (\mathbf{H}_{\text{eff},k} + \boldsymbol{\xi}_k)] \}. \end{aligned} \quad (5.9)$$

Here \mathbf{S}_k is a unit vector denoting the direction of the spin of lattice site k . The random thermal field again has white noise properties with zero mean and a variance of

$$\langle \xi_{i,k}(t) \xi_{j,l}(t') \rangle = \frac{2\lambda k_B T}{\gamma \mu_S} \delta_{ij} \delta_{kl} \delta(t - t'), \quad (5.10)$$

where i, j are the Cartesian components of the thermal field and k, l represent the lattice sites. Equations 5.9 and 5.10 are equivalent to Eqs. 4.2 and 4.4 if the spatial discretization becomes atomistic, and thus the magnetization unit vector $\hat{\mathbf{m}}$ is replaced with the spin \mathbf{S}_k . Additionally, the magnetic moment of an atom is written as $\mu_S = M_S v$ and we use λ for the damping constant instead of α in the atomistic formulation. As shown in Appendix D the effective magnetic field $\mathbf{H}_{\text{eff},k}$ acting on spin k can be expressed as the derivative of the spin Hamiltonian with respect to \mathbf{S}_k ,

$$\mathbf{H}_{\text{eff},k} = -\frac{1}{\mu_S} \frac{\partial \mathcal{H}}{\partial \mathbf{S}_k}. \quad (5.11)$$

VAMPIRE uses a typical spin Hamiltonian containing exchange energy, uniaxial anisotropy energy and Zeeman energy as follows

$$\begin{aligned} \mathcal{H} = & - \sum_{k,l} J_{k,l} \mathbf{S}_k \cdot \mathbf{S}_l - K_1 \sum_k S_{z,i}^2 \\ & - \mu_S \sum_k \mathbf{H}_{\text{ext}} \cdot \mathbf{S}_k. \end{aligned} \quad (5.12)$$

Besides the geometry of the particle, the Heisenberg exchange parameters $J_{k,l}$, the uniaxial anisotropy constant K_1 and the atomistic spin moment μ_S are the main input parameters in this model.

Compared to the atomistic LLG equation (Eq. 5.9), the LLB equation has two additional contributions, namely, the last two terms on the right-hand side of Eq. 5.1. These terms describe the changes in the length of the magnetization with temperature and ensure that even the magnetization of a particle, represented with just one magnetic moment, vanishes at the Curie temperature.

5.3 Temperature dependent material functions

For the solution of the LLB equation the temperature dependence of the zero-field equilibrium magnetization $m_e(T)$, the parallel susceptibility $\tilde{\chi}_{\parallel}(T)$ and the normal susceptibility $\tilde{\chi}_{\perp}(T)$ are required. This information is obtained by atomistic simulations using VAMPIRE. In this work we use cylindrical layers with 5 nm height and basal planes with a diameter of 5 nm or 10 nm. We model three different materials, a hard magnetic (HM) one with strong exchange coupling and two soft magnetic (SM) ones with similar exchange coupling but higher Curie temperatures. For simplicity, all materials are assumed to have a simple cubic crystal structure. The detailed parameters are illustrated in Tab. 5.1. For any other system the explained procedures work similarly.

	HM	SM1	SM2
K_1 [J/m ³]	$6.6 \cdot 10^6$	0.0	0.0
A_{ex} [J/m]	$2.158 \cdot 10^{-11}$	$2.992 \cdot 10^{-11}$	$2.992 \cdot 10^{-11}$
μ_S [μ_B]	1.7	1.7	2.56
J_S [T]	1.43	1.43	2.15
a [nm]	0.24	0.24	0.24
λ	0.1	1.0	1.0
T_C [K]	536.47	820.78	795.19

Table 5.1: Simulation input parameters of a hard magnetic (HM) material and two soft magnetic (SM) materials. K_1 is the anisotropy constant, A_{ex} is the bulk exchange interaction in the materials, μ_S is the atomistic magnetic moment in units of the Bohr magneton μ_B , J_S is the corresponding saturation magnetization in the LLB model, a is the lattice constant of the used simple cubic lattice, λ is the damping constant and T_C is the Curie temperature.

5.3.1 Calculation of $m_e(T)$

We simulate 100 trajectories of 20000 time steps with an integration step of 10^{-15} s (after 20000 equilibration steps) for each temperature value in the range of 0 – 800 K for the

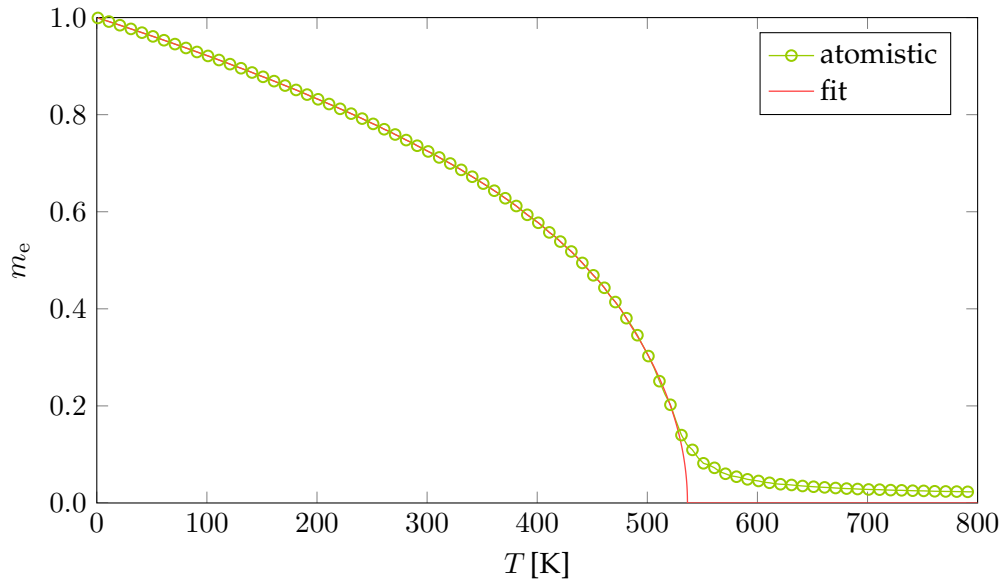


Figure 5.1: Zero-field equilibrium magnetization m_e versus temperature, calculated from an atomistic model of the HM material (see Tab. 5.1). The red solid line shows a fit, representing an infinite system.

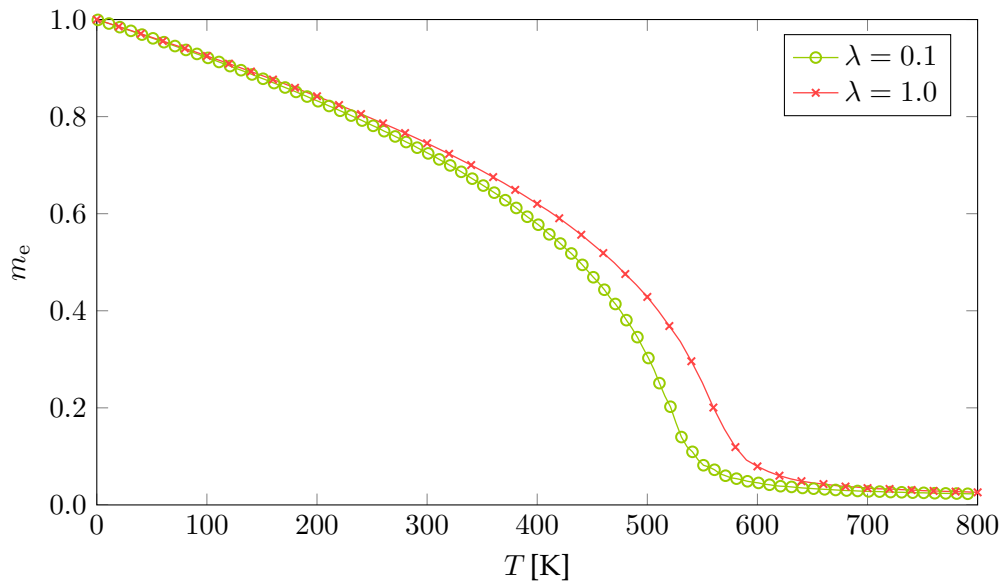


Figure 5.2: Zero field equilibrium magnetization m_e versus temperature, calculated from an atomistic model of the HM material (see Tab. 5.1) for different damping constants λ .

HM material using VAMPIRE. Figure 5.1 illustrates the atomistic result for $m_e(T)$ after averaging over the 100 calculated trajectories. The plot clearly shows finite size effects. The LLB equation requires temperature-dependent functions for an infinite system, because the Curie point has to be properly defined. Thus, the atomistic data are fitted with true critical behavior near T_C . A fit with $f(T) = c\sqrt{1 - T/T_C}$, where c is a fitting

constant, extrapolates to $T_C = 536.47$ K. It has to be pointed out, that not only the magnetic anisotropy, the exchange constant, the saturation polarization and the system size determine the zero-field equilibrium magnetization, but also the used damping in the atomistic LLG dynamics has an influence. Figure 5.2 compares $m_e(T)$ for the same HM particle with different damping constants. The same procedure as explained above is used to calculate m_e for the SM layers.

5.3.2 Calculation of $\tilde{\chi}_{\parallel}(T)$ and $\tilde{\chi}_{\perp}(T)$

According to the spin fluctuation model the transverse and parallel susceptibilities can be obtained by the fluctuations of the magnetization components between subsequent time steps in the atomistic model as follows

$$\tilde{\chi}_{\eta} = \frac{\mu_S N}{k_B T} \left(\langle m_{\eta}^2 \rangle - \langle m_{\eta} \rangle^2 \right). \quad (5.13)$$

Transverse and parallel denote directions with respect to the easy axis of the investigated particle. To be consistent with Eq. 5.8, where the susceptibilities are defined with respect to an external applied field, both, the preferred magnetic direction and the direction of the magnetic field, are assumed to be parallel. In Eq. 5.13 N is the number of spins, T is the temperature and

$$m_{\eta} = \frac{1}{N} \sum_{i=k}^N S_{\eta,k} \quad (5.14)$$

is the average magnetization along the direction of η . All fluctuations are calculated at zero applied field. In the case of the HM material the corresponding fluctuations, obtained by 100 atomistic trajectories of 20000 time steps ($\Delta t = 10^{-15}$ s, after 20000 equilibration steps) at each temperature in the range of 0 – 800 K, are illustrated in Fig. 5.3. The expected critical behavior of $\tilde{\chi}_{\parallel}$ at the Curie point can be clearly seen. Above T_C the particle is paramagnetic, and thus the susceptibilities in all directions become equal. As mentioned in the preceding section, the LLB equation requires temperature-dependent functions for an infinite system. From the spin fluctuation model it is known that the longitudinal susceptibility is proportional to $1/(T - T_C)$ around the Curie temperature, which is used as fit function. At low temperatures

$$\tilde{\chi}_{\perp} = \frac{M_0 m_e^2}{2K_1(T)} \quad (5.15)$$

holds. If $K_1(T)$ is expressed with a power law $K_1(T) \propto m_e^c$, the final piecewise fit functions for the susceptibilities are as follows

$$\tilde{\chi}_{\parallel} = \begin{cases} \frac{c_1}{T_C - T} & T < T_C \\ \frac{c_2}{T - T_C} & T > T_C, \end{cases} \quad (5.16)$$

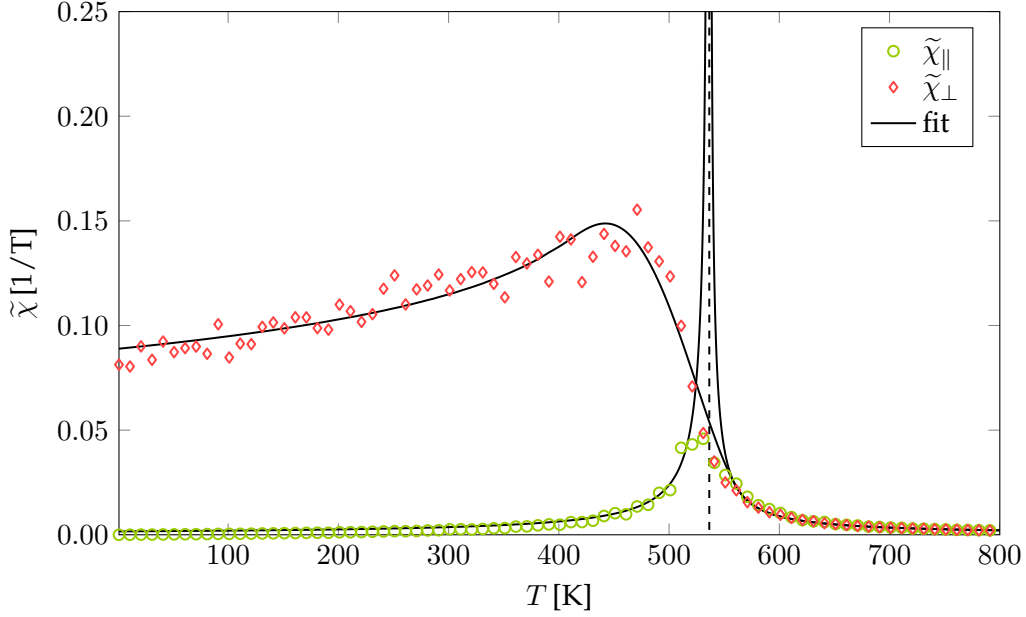


Figure 5.3: Transverse and parallel susceptibilities versus temperature of a HM material (see Tab. 5.1), obtained by the fluctuations of the magnetization components in an atomistic model. The lines show fit functions extrapolating to the critical behavior of an infinite system. The dashed line indicates T_C .

$$\tilde{\chi}_{\perp} = \begin{cases} c_3 m_e^{c_4} & T \ll T_C \\ \frac{c_5}{T - T_C} & T > T_C, \end{cases} \quad (5.17)$$

where $c_1 - c_5$ are fit parameters, which have to be determined for the investigated particle. In the intermediate temperature range where $\tilde{\chi}_{\perp}$ is still undefined, a fourth-order polynomial is used, which is continuously differentiable at the connection points to the low- and high-temperature functions. With the remaining degree of freedom of the polynomial the atomistic data are then fitted. The positions of the intersection points, which delimit the parts with different fit behavior of $\tilde{\chi}_{\perp}$, are chosen to minimize the mean squared displacement of the fit and the atomistic fluctuations in the whole temperature range. For the HM material with strong uniaxial anisotropy, the illustrated procedure to compute the required temperature-dependent susceptibilities is straightforward.

It has to be mentioned that the above-presented approach to determine the equilibrium magnetization and the susceptibilities from atomistic simulations was already well described by Kazantseva et. al [71]. We repeated it for completeness. Unfortunately, the so far illustrated calculation of $\tilde{\chi}_{\parallel}(T)$ and $\tilde{\chi}_{\perp}(T)$ just works for a hard magnetic material with strong uniaxial anisotropy.

It is different in the case of the SM materials (see Tab. 5.1), which have small or no uni-

axial anisotropy, but still strong exchange. Without an external field such particles are superparamagnetic. It is just shown how to deal with the SM1 material in the following, because the procedure works analogously for a SM2 material.

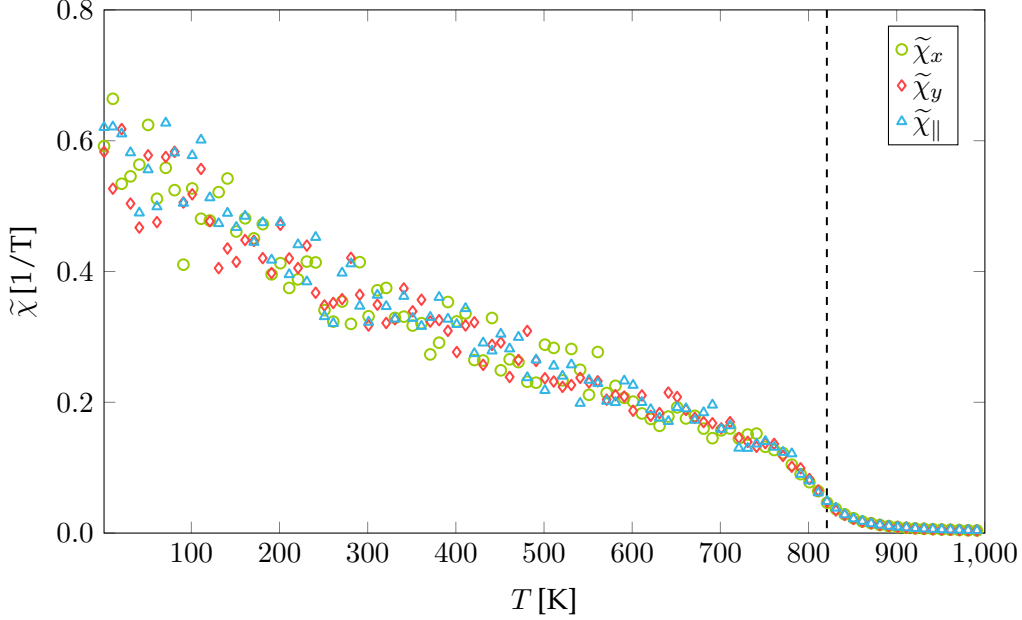


Figure 5.4: Susceptibilities versus temperature of the SM1 material (see Tab. 5.1), obtained by the fluctuations of the magnetization components in an atomistic LLG model. The dashed line indicates T_C . The data belong to a cylindrical particle consisting of the SM material (see Tab. 5.1) and are simulated with VAMPIRE.

Averaging over the corresponding magnetization fluctuations of 100 trajectories at each temperature from 0 K to 1000 K yields the susceptibilities shown in Fig. 5.4. All components of the susceptibility coincide, because the particle has no preferred magnetic direction. Hence, there does not exist a critical behavior of $\tilde{\chi}_{||}$. Above the Curie point we again find the $(T - T_C)^{-1}$ dependence of all susceptibility components. For low temperatures Fig. 5.4 does not reflect the full range of the magnetization fluctuations. The thermal field, which drives the magnetization, is small, and hence the simulated trajectories are too short to capture the full magnitude of the susceptibilities. From a physical point of view, $\tilde{\chi}_{\perp}$ should diverge at zero temperature because of Eq. 5.15. If K_1 is zero at $T = 0$ then the anisotropy constant should still be zero at higher temperatures. Since the anisotropy field is zero for a ferromagnetic material with zero K_1 , the transverse susceptibility has to be infinite according to Eq. 5.6. In the general case of a soft magnetic material with a small but nonvanishing anisotropy constant, the mean value of the transverse susceptibility converges to $\tilde{\chi}_{\perp} \rightarrow \frac{\mu_S N}{3k_B T}$. This should also be observed in the magnetization fluctuations, if the simulated trajectories are long enough. In the paramagnetic state above T_C a fit of the magnetization fluctuations with $c/(T - T_C)$

according to Eq. 5.16 can be used to describe the transverse susceptibility, independent of K_1 .

The construction of the parallel susceptibility for the SM materials is not that straightforward. $\tilde{\chi}_{\parallel}$ ensures the magnetization length in the LLB equation to remain in the vicinity of m_e , according to the internal exchange field \mathbf{H}_J (Eq. 5.7). Since $\tilde{\chi}_{\parallel}$ cannot be obtained by fluctuations of the z -component of the magnetization, we propose to extract it from the variance in the magnetization length as

$$\tilde{\chi}_{\parallel} = \tilde{\chi}_m = b \frac{\mu_S N}{k_B T} \left(\langle |\mathbf{m}|^2 \rangle - \langle |\mathbf{m}| \rangle^2 \right) = b \frac{\mu_S N}{k_B T} \text{Var}(|\mathbf{m}|). \quad (5.18)$$

Figure 5.5 displays that the fluctuations of the magnetization length are smaller than

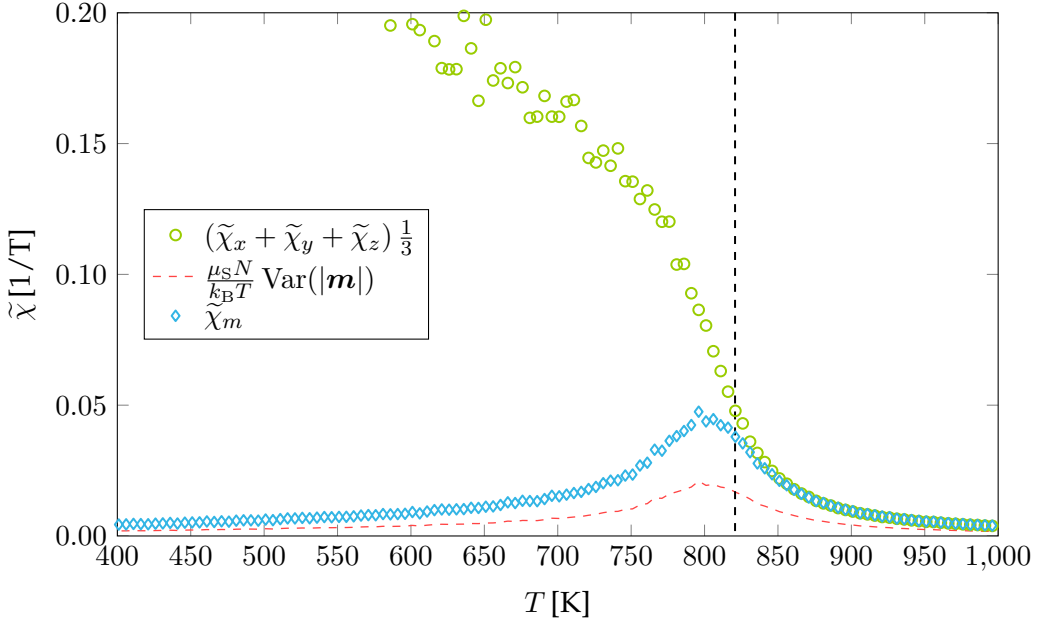


Figure 5.5: Variance of the magnetization length fitted to the average of the Cartesian components of the susceptibility, above T_C . The resulting function $\tilde{\chi}_m$ serves as parallel susceptibility. The dashed line indicates T_C . The data belong to a cylindrical particle consisting of the SM1 material (see Tab. 5.1) and are simulated with VAMPIRE.

the fluctuations of its components, because the length cannot change its sign. However, $\text{Var}(|\mathbf{m}|)$ shows critical behavior. With the proportionality factor b in Eq. 5.18 the length fluctuations are scaled to the average fluctuations of its Cartesian components ($\sum_i \frac{1}{3} \tilde{\chi}_i$) above the Curie point (Fig. 5.5). The fit functions listed in Eq. 5.16 are then applied to the resulting $\tilde{\chi}_m$, yielding the parallel susceptibility, which is needed for the LLB model, as shown in Fig. 5.6.

The above-presented procedure to obtain the parallel susceptibility for the LLB model can, in principle, be applied to an arbitrary particle, ranging from very soft to very hard

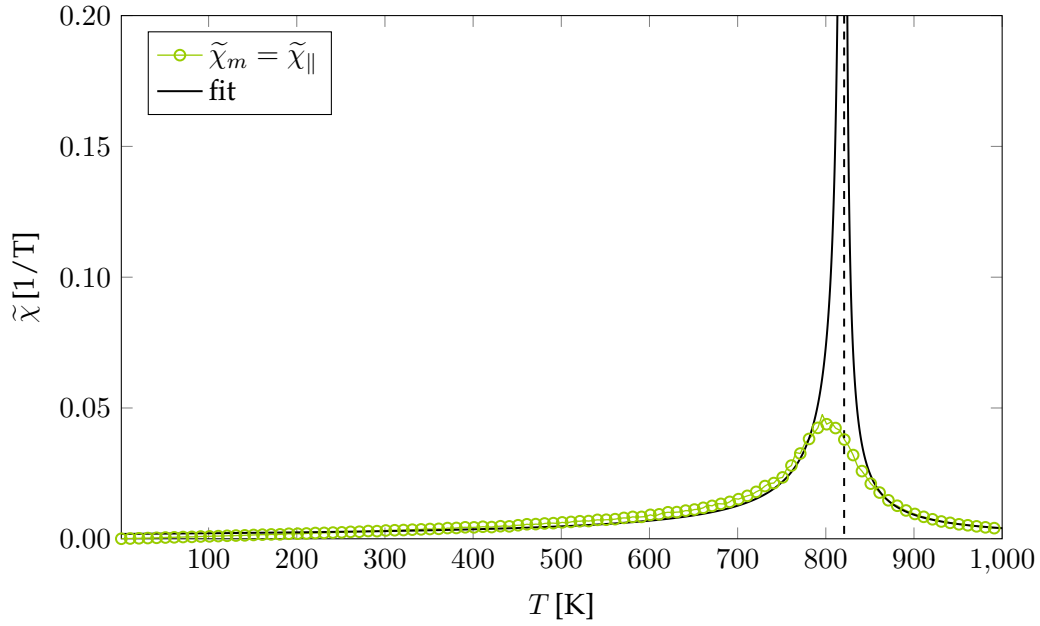


Figure 5.6: Fit of the parallel susceptibility of the SM1 material according to Eq. 5.16. The dashed line indicates T_C .

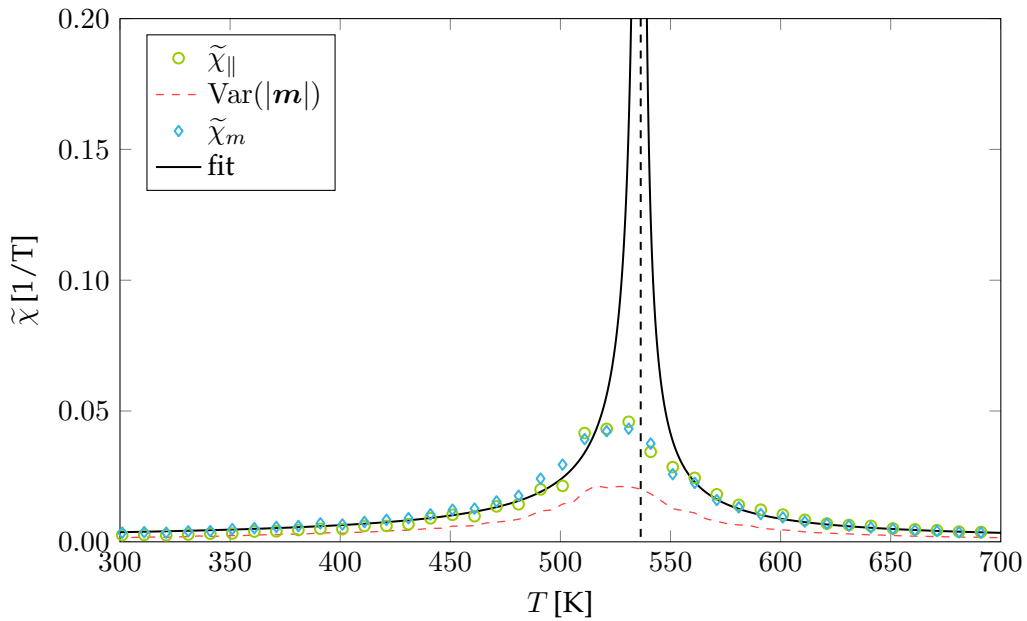


Figure 5.7: Identical fluctuations of the z -component of the magnetization ($\tilde{\chi}_{||}$) and its length ($\tilde{\chi}_m$), after scaling the latter. The dashed line indicates T_C . The data belong to a cylindrical particle consisting of the HM material (see Tab. 5.1) and are simulated with VAMPIRE.

magnetic. Figure 5.7 illustrates that the scaled fluctuations of the magnetization length correspond to the fluctuations of its z -component, also in case of the HM material.

5.4 LLB versus VAMPIRE (dynamics comparison)

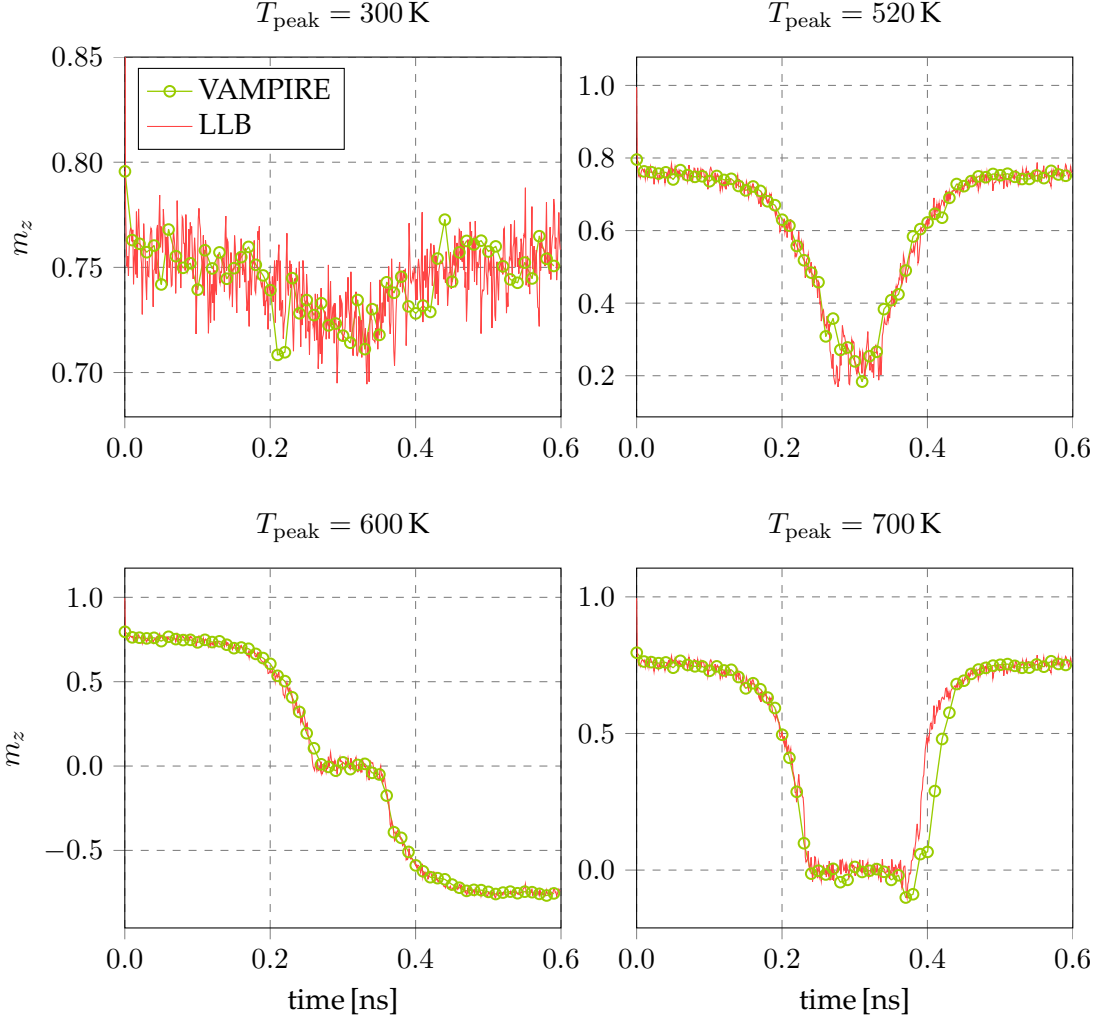


Figure 5.8: Dynamics of the z -component of the magnetization of a HM layer (see Tab. 5.1) subject to a Gaussian heat pulse with a length of $t_{\text{peak}} = 100$ ps and different peak temperatures. Simulation data obtained by atomistic LLG simulations using VAMPIRE and LLB calculations are compared. In the LLB model, where the whole layer is represented by one spin, temperature-dependent material functions as shown in Sec. 5.3 are used.

In order to test the computed temperature-dependent material functions we compare short magnetization trajectories of 0.6 ps obtained by integrating the LLB equation with atomistic simulations using VAMPIRE. Firstly, the magnetization dynamics of the HM material under the influence of a Gaussian heat pulse is examined. The profile of the heat pulse is given by

$$T(t) = (T_{\text{peak}} - T_{\text{min}}) e^{-\left(\frac{t-t_{\text{peak}}}{t_{\text{pulse}}}\right)^2} + T_{\text{min}}. \quad (5.19)$$

The initial temperature of the pulse T_{min} is set to 270 K and $t_{\text{peak}} = 3t_{\text{pulse}}$ is valid in

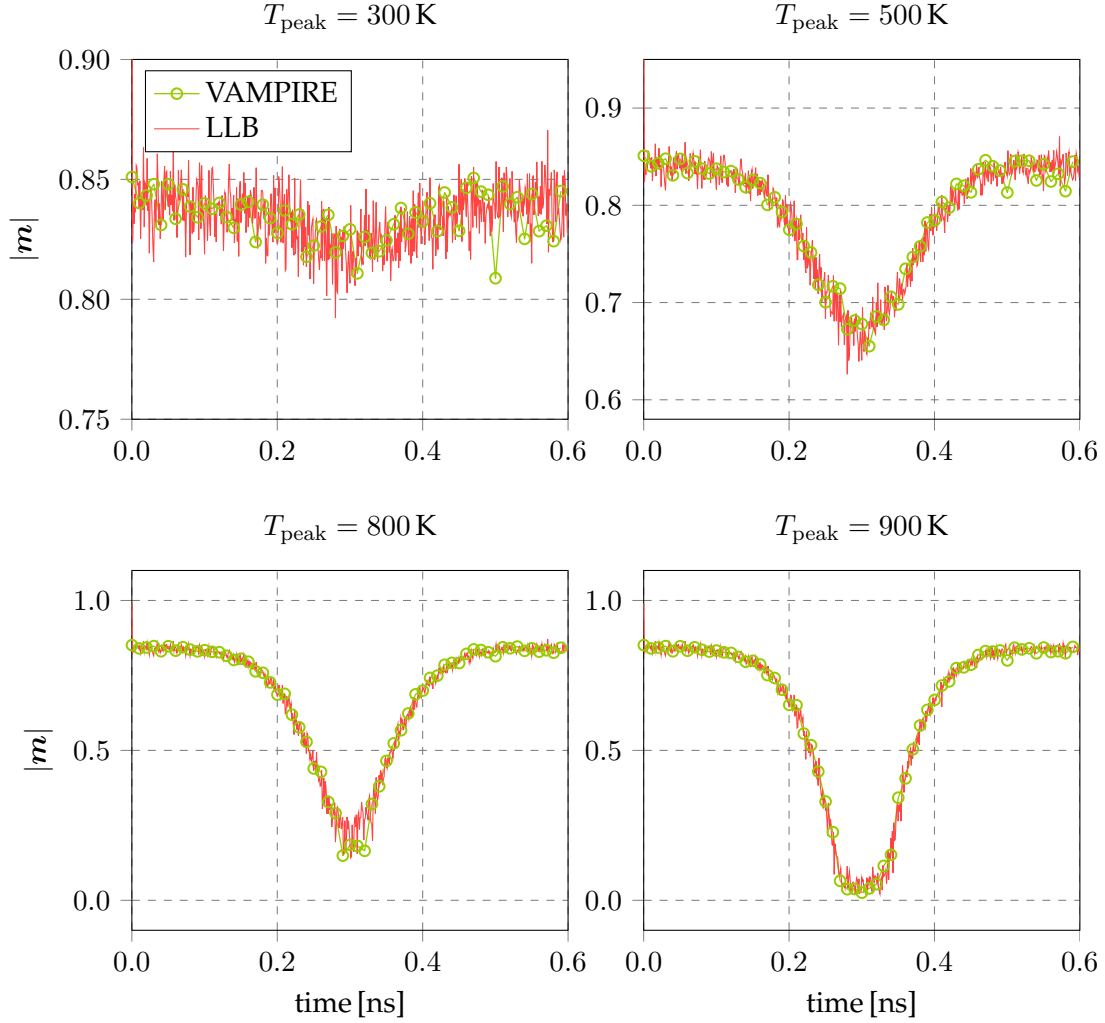


Figure 5.9: Dynamics of the magnetization length of a SM1 layer (see Tab. 5.1) subject to a Gaussian heat pulse with a length of $t_{\text{peak}} = 100$ ps and different peak temperatures. Simulation data obtained by atomistic LLG simulations using VAMPIRE and LLB calculations are compared. In the LLB model, where the whole layer is represented by one spin, temperature-dependent material functions as shown in Sec. 5.3 are used.

all simulations. Here a pulse duration of $t_{\text{peak}} = 100$ ps is used, and thus the maximum temperature is reached at $t_{\text{peak}} = 0.3$ ns. All presented trajectories start with a magnetization fully aligned along the positive z -direction. Figure 5.8 illustrates the z -component of the magnetization for different peak temperatures of the applied heat pulse. Although the HM layer is represented with just one spin in the LLB simulations the resulting curves fit the averaged magnetization of the VAMPIRE data almost perfectly for temperatures beyond and above the Curie temperature as well as close to it. As expected, the magnetization decreases at high temperatures and reaches zero above T_C . As the lower plots in Fig. 5.8 point out m_z can randomly relax in its initial or in the opposing direction after the temperature of the heat pulse again decreases under the

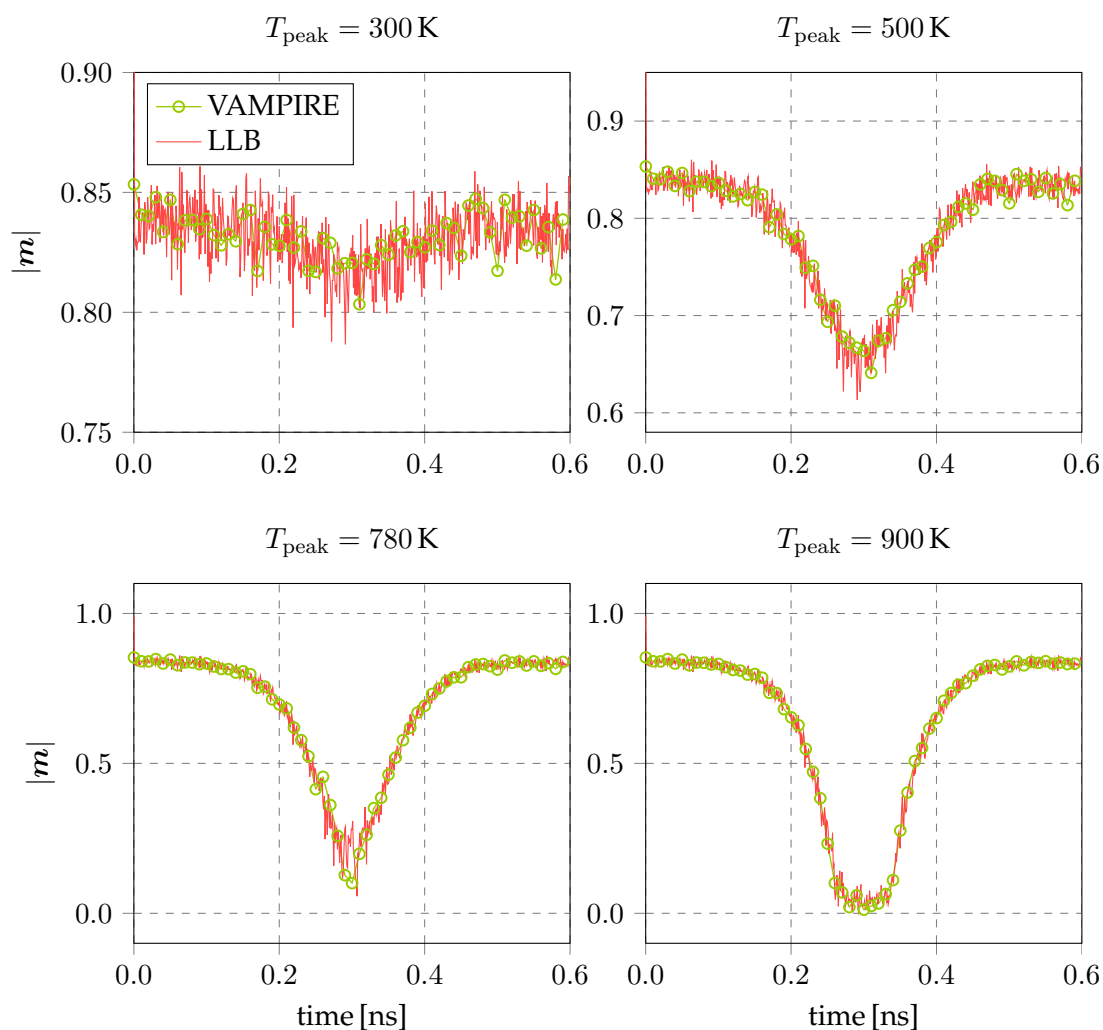


Figure 5.10: Same comparison as shown in Fig. 5.9 for a SM2 layer (see Tab. 5.1).

Curie temperature.

Since the components of the SM layers fluctuate very strong (they have no preferred magnetic direction) their magnetization lengths are compared in a first step. Heat pulses with different peak temperatures are again applied yielding the curves of the magnetization length shown in Figs. 5.9 and 5.10. The accordance between VAMPIRE and LLB is again very good and the figures show no noteworthy differences as the SM1 and SM2 materials are equal despite of a small change in their magnetic moment. It is very important for the simulations of the following sections that the magnetization dynamics of the SM layers under an external magnetic field are well reproduced by the LLB model. Hence, Figs. 5.11 and 5.12 show m_z at constant temperature subject to an external applied field of 0.5 T. The curves are again very similar for the two SM layers and the agreement is good between atomistic LLG and LLB simulations. In the upper plots we notice that the magnetization reversal is very fast and the lower plots again

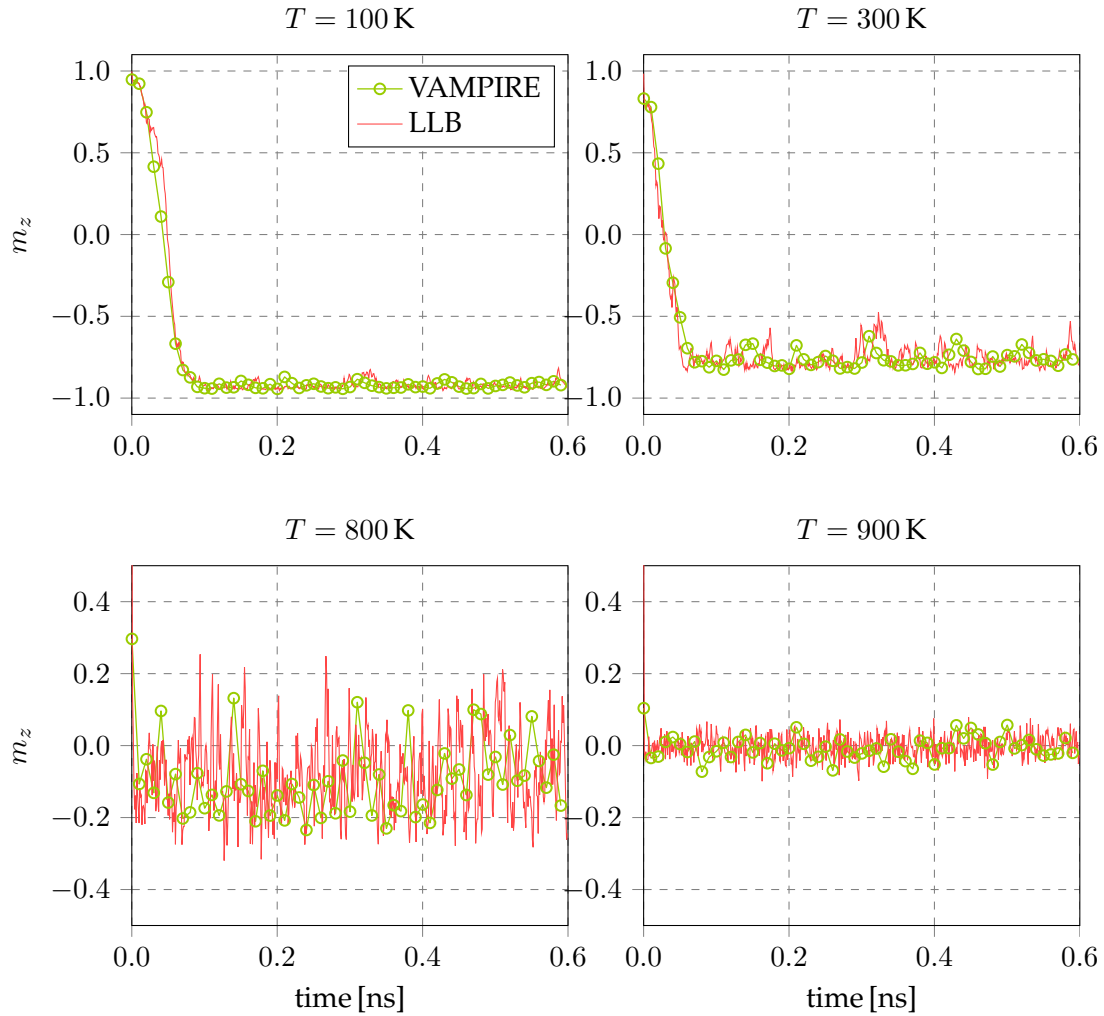


Figure 5.11: Dynamics of the z -component of the magnetization of a SM1 layer (see Tab. 5.1) at different constant temperatures. Additionally, a magnetic field of 0.5 T is applied to the layer. Simulation data obtained by atomistic LLG simulations using VAMPIRE and LLB calculations are compared. In the LLB model, where the whole layer is represented by one spin, temperature-dependent material functions as shown in Sec. 5.3 are used.

point out that the magnetization vanishes near the Curie point.

Summarized, this section proves that the calculated temperature-dependent material functions are appropriate to produce the correct magnetization dynamics of the presented materials (see Tab. 5.1), by computing the time evolution of a single spin using the LLB equation. This is valid for both, varying temperatures and external magnetic fields.

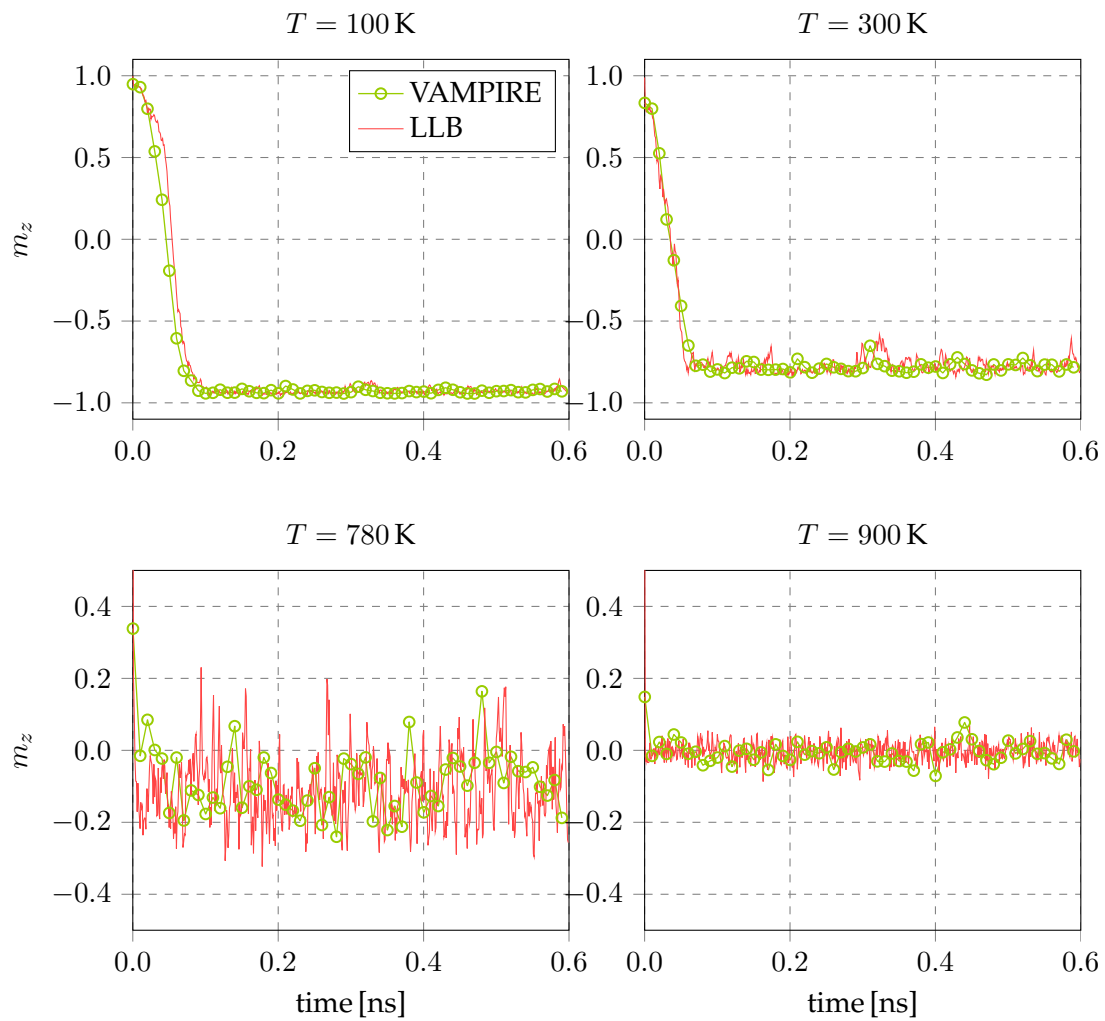


Figure 5.12: Same comparison as shown in Fig. 5.11 for a SM2 layer (see Tab. 5.1).

5.5 Intergrain exchange

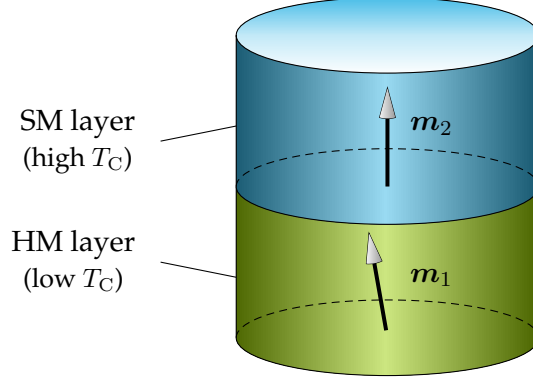


Figure 5.13: Grain model consisting of a stack of two layers with high and low Curie temperatures, coupled via an intergrain exchange interaction on the boundary surface. Each layer is represented as a single magnetization vector (m_1 and m_2).

Since we aim to model high/low T_C grains, we have to describe the coupling of different material layers. In the coarse-grained model each layer is represented by one magnetization vector, which are coupled via an intergrain exchange interaction on the boundary surface, as shown in Fig. 5.13. In this work we restrict ourselves to two layers, but it is easy to extend the model to an arbitrary layer number. In order to derive the intergrain exchange the Heisenberg Hamiltonian, which gives the total exchange energy across the grain's boundary surface, serves as a starting point,

$$\mathcal{H} = - \sum_{ss} J_{kl} \mathbf{S}_k \mathbf{S}_l. \quad (5.20)$$

Here ss indicates the sum over all surface spins. The exchange integrals J_{kl} are assumed to be independent of the lattice site. With the unit vectors \mathbf{u}_k and \mathbf{u}_l along the spin directions the Hamiltonian reads

$$\mathcal{H} = -JS^2 \sum_{ss} \mathbf{u}_k \mathbf{u}_l. \quad (5.21)$$

In a simple cubic lattice each spin just has one nearest neighbor on the opposing side of an interface. In this case one can rewrite \sum_{ss} as sum over all spins on the surface of layer 1, each interacting with its neighboring spin in layer 2,

$$\mathcal{H} = -2JS^2 \sum_k \mathbf{u}_{k,1} \mathbf{u}_{k,2}. \quad (5.22)$$

Now we perform the transition from the atomistic to the LLB description where all spins in each layer are described with just one magnetization vector. If F is assumed to be the area of the interaction surface and a the lattice constant in the atomistic model,

we have F/a^2 interacting pairs of spins on the boundary surface. The Hamiltonian becomes

$$\mathcal{H} = -2JS^2 \frac{F}{a^2} \frac{\mathbf{m}_1 \cdot \mathbf{m}_2}{m_1 m_2}, \quad (5.23)$$

where unit vectors are written with \mathbf{m}_i/m_i , because the magnetization length is not conserved in the LLB model. With Eq. 5.23 the intergrain exchange field of layer 1 can be derived by taking the derivative of the exchange energy with respect to the layer's magnetic moment,

$$\mathbf{H}_{\text{iex},1} = -\frac{1}{V\mu_0 M_0} \frac{\partial}{\partial \mathbf{m}_1} \mathcal{H}. \quad (5.24)$$

The intergrain exchange field calculates to

$$\begin{aligned} \mathbf{H}_{\text{iex},1} &= \frac{2JS^2 F}{a^2 V \mu_0 M_0} \left(\frac{\mathbf{m}_2 m_1 m_2 - \mathbf{m}_1 m_2 \frac{m_1}{m_1} m_2}{m_1^2 m_2^2} \right) \\ &= \frac{2JS^2}{a^2 d \mu_0 M_0} \left(\frac{\mathbf{m}_2}{m_1 m_2} - \cos(\theta_{12}) \frac{\mathbf{m}_1}{m_1^2} \right), \end{aligned} \quad (5.25)$$

with the angle between the magnetic moments θ_{12} and the thickness d of layer 1. Introducing the temperature-dependent intergrain exchange constant $A_{\text{iex}}(T) = JS^2/a$, the intergrain exchange field acting on the magnetization of layer 1 becomes

$$\mathbf{H}_{\text{iex},1} = \frac{2A_{\text{iex}}(T)}{ad\mu_0 M_0} \left(\frac{\mathbf{m}_2}{m_1 m_2} - \cos(\theta_{12}) \frac{\mathbf{m}_1}{m_1^2} \right). \quad (5.26)$$

The computation of the temperature dependence of A_{iex} is, in general, less straightforward. For example, in the case of FePt the bulk exchange stiffness was successfully calculated by determining the free energy and the width of a domain wall in the investigated material [71, 79]. There also exists an approach where the dispersion relation of thermally excited spin waves yields the temperature dependence of the exchange coupling [80]. Both methods are computationally expensive and yield the same scaling behavior of $A_{\text{iex}} \sim m^\alpha$. We try to keep the coarse-grained LLB model as simple as possible and construct the temperature dependence of the intergrain exchange analytically from the according dependencies of the bulk exchange constants in the interacting layers. These are described with a power law of the magnetization length $A(T) \propto m_e^\alpha(T)$, which holds at least for low temperatures. In many cases it is also a suitable description at high temperatures [80].

From a physical point of view we ask for symmetric exchange constants with equivalent $A_{12}(T)$ and $A_{21}(T)$. There are two obvious possibilities for symmetric intergrain exchange constants

- an arithmetic mean of the bulk values,

$$A_{\text{iex}}(T) = A_{\text{iex}}(0) \frac{m_{e,1}^\alpha(T) + m_{e,2}^\beta(T)}{2} \quad (5.27)$$

- or an the geometric mean of the bulk values,

$$A_{\text{ie}}(T) = A_{\text{ie}}(0) \sqrt{m_{\text{e},1}^{\alpha}(T) m_{\text{e},2}^{\beta}(T)}. \quad (5.28)$$

α and β are the corresponding power-law exponents for the temperature dependence of the bulk exchange constants of the layers. At the Curie temperature the magnetization becomes zero, thus also the intergrain exchange should vanish. Since the geometric mean is zero as soon as one of the equilibrium magnetizations vanishes, the geometric mean is the preferred formulation. Finally, the full exchange field of layer 1 is

$$\mathbf{H}_{\text{ie},1} = \frac{2A_{\text{ie}}(0) \sqrt{m_{\text{e},1}^{\alpha}(T) m_{\text{e},2}^{\beta}(T)}}{ad\mu_0 M_0 m_1} \left(\frac{\mathbf{m}_2}{m_2} - \cos(\theta_{12}) \frac{\mathbf{m}_1}{m_1} \right). \quad (5.29)$$

Atxitia et al. [80] investigated the power law of the exchange stiffness with numerical methods and derived the exponent of FePt analytically to 1.76. The underlying Hamiltonian in Ref. [80] also considers the two-site anisotropy and not only uniaxial anisotropy, as in our performed atomistic simulations. Nevertheless, we use this exponent for the HM material, because its material properties are very similar to those of FePt. It turned out in the simulations that the values of the exponents in the power laws are not crucial in a sense that deviations of 10-20 % do not change the following results significantly. For a generic ferromagnet with localized magnetic moments on a simple cubic lattice and in the absence of anisotropy the exponent becomes 1.66 [80], which is used for the SM layers.

5.6 Intergrain exchange field correction

We investigate the switching behavior of a high/low T_C grain subject to a heat pulse with Gaussian profile according to Eq. 5.19. The grain has a cylindrical geometry with a basal plane diameter of 5 nm and a total height of 10 nm and it consists of 50 % HM and 50 % SM material as introduced in Tab. 5.1. All calculations start with a magnetization in the positive z -direction. An external magnetic field assists the magnetization reversal and points in the negative z -direction with a tilt of 0.1 rad. In the atomistic simulations with VAMPIRE a simple cubic crystal lattice with a lattice constant of $a = 0.24$ nm is assumed in all parts of the grain. We compute the switching probability of the recording grain subject to heat pulses with different durations t_{pulse} and peak temperatures. Figure 5.14 illustrates such switching probability curves for heat pulses with a duration of $t_{\text{pulse}} = 100$ ps and an external field with $\mu_0 H_{\text{ext}} = 0.5$ T. Each probability value is an average of 128 independent trajectories computed with both, the coarse-grained LLB model (red solid lines) and with VAMPIRE (green lines with circles), for different intergrain exchange constants $A_{\text{ie}}(0)$. The accordance is insufficient for weak intergrain

exchange. Although the curves seem to agree well for strong exchange coupling, we see that the problem is the same for large $A_{\text{iex}}(0)$. Actually, there exists a LLB switching probability curve which fits the VAMPIRE data much better. As long as the exchange is strong, the switching probability curves do not change much, and thus the agreement still seems to be good in Fig. 5.14. In order to resolve the discrepancy between LLB and VAMPIRE simulations we examine a simpler system, consisting of two identical HM layers. We calculate the switching probabilities for six intergrain exchange values ($A_{\text{iex},n} = 2.158 \cdot 10^{-11}/2^n \text{ J/m}$, $0 \leq n \leq 5$) using VAMPIRE. The applied Gaussian heat pulse has again a duration of $t_{\text{pulse}} = 100 \text{ ps}$ and the applied field has a strength of 0.5 T. Since the coarse-grained LLB model is computationally less expensive, the same probability curves for 70 values of $A_{\text{iex}}(0)$ are simulated in the same range. After that, the LLB results are fitted to the atomistic ones, yielding correction factors k_{cor} for the exchange field in the LLB model as shown in Fig. 5.15. For increasing intergrain exchange constant the reduction of \mathbf{H}_{iex} increases linearly. This dependence can be understood as follows: For weak coupling the exchange interaction is mainly located at the interface between the layers, but for large A_{iex} the domain wall is not restricted to the interface but extends towards the bulk magnets. However, in the LLB approach the grain is not discretized and the domain wall cannot be formed except at the interface. Hence, the domain wall energy is overestimated. For this reason the final expression of the intergrain exchange field is

$$\mathbf{H}_{\text{iex},1} = k_{\text{cor}} \frac{2A_{\text{iex}}(T)}{ad\mu_0 M_0} \left(\frac{\mathbf{m}_2}{m_1 m_2} - \cos(\theta_{12}) \frac{\mathbf{m}_1}{m_1^2} \right). \quad (5.30)$$

If full intergrain exchange coupling between the equal layers is assumed, a correction factor of almost $k_{\text{cor}} = 1/20$ is needed in the exchange field to reproduce the correct dynamics with the LLB model. It is not surprising that the correction factor nearly equals the ratio of the lattice constant and the layer thickness $k_{\text{cor}} \sim a/d$. After inserting the reduction factor in Eq. 5.30 and considering that the magnetization lengths m_1 and m_2 are almost identical in the same material, the exchange field becomes

$$\mathbf{H}_{\text{ex}} = \frac{2A_{\text{iex}}(T)}{d^2 \mu_0 M_0 m^2} (\mathbf{m}_2 - \cos(\theta_{12}) \mathbf{m}_1). \quad (5.31)$$

Under the micromagnetic assumption that neighboring magnetic moments just comprise small angles, $\cos(\theta_{12}) \approx 1$ is valid, and thus Eq. 5.31 becomes identical to the discretized Laplace operator (discretization length d) in a finite difference schema [70, 71, 72, 77].

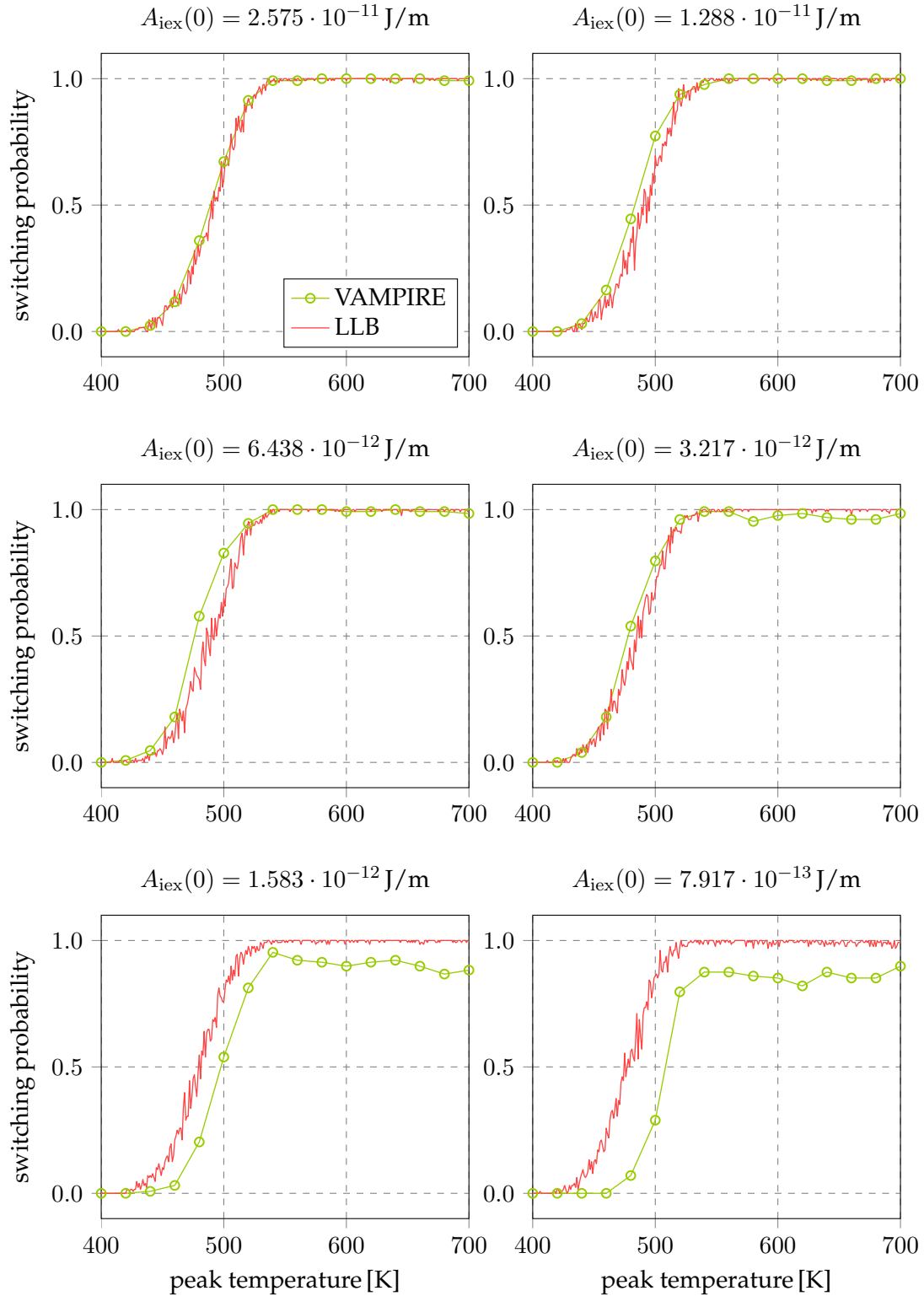


Figure 5.14: Comparison of atomistic switching probability curves (green lines with circles) with the results of the coarse-grained LLB model (red solid lines) for different intergrain exchange constants ($A_{\text{iex},n}(0) = 2.575 \cdot 10^{-11}/2^n \text{ J/m}$, $0 \leq n \leq 5$). The investigated high/low T_C grain is subject to a Gaussian heat pulse with $t_{\text{pulse}} = 100 \text{ ps}$ and an external field with 0.5 T strength.

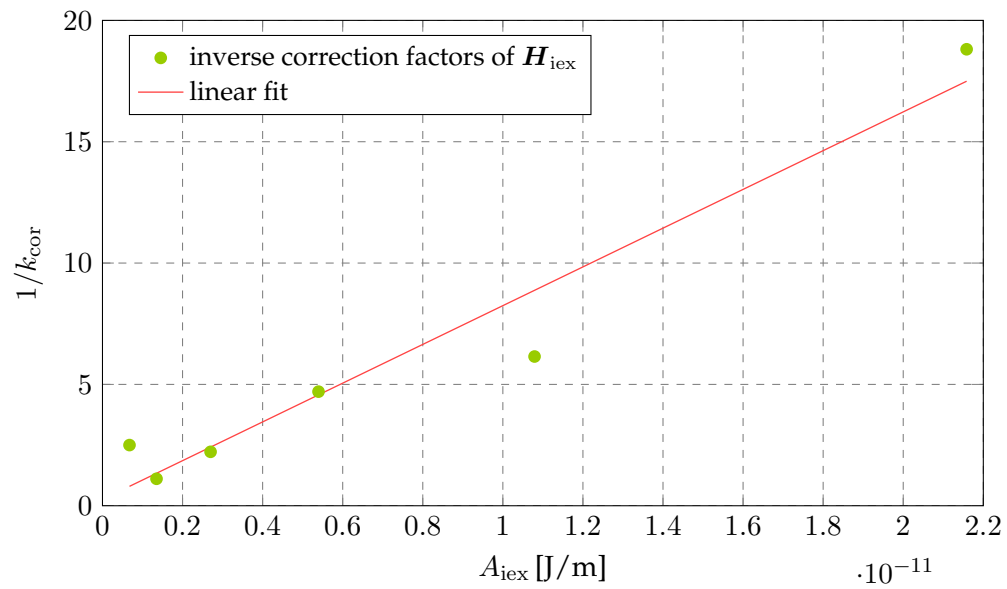


Figure 5.15: Linear fit of the inverse correction factors $1/k_{\text{cor}}$ of the intergrain exchange field in the LLB model consisting of two HM layers (see Tab. 5.1). The bulk exchange interaction within the layers is assumed to be $A_{\text{ex}} = 2.158 \cdot 10^{-11} \text{ J/m}$.

5.7 Results

The case is similar for grains consisting of layers with different bulk exchanges. The presented construction of a linear correction fit function for the exchange field from several switching probability simulations at different strengths of the intergrain exchange works well, as we prove in the following.

5.7.1 Model verification

id	diameter [nm]	SM	t_{pulse} [ps]	$\mu_0 H_{\text{ext}}$ [T]	figure
1	5	SM1	100	0.5	5.16
2	5	SM1	10	0.5	5.17
3	5	SM1	100	0.8	5.18
4	5	SM2	100	0.5	5.19
5	10	SM1	100	0.5	5.20
6	10	SM2	100	0.5	5.21

Table 5.2: Simulation parameters for the verification cases of the coarse-grained LLB model. Switching probability curves for cylindrical grains with different diameters are calculated. Different high/low T_C combinations of a HM material and one of the SM materials (see Tab. 5.1) are used. t_{pulse} indicates the duration of the applied heat pulse and $\mu_0 H_{\text{ext}}$ gives the strength of the applied magnetic field. In the last column the figure number of the verification plot is given.

To validate the coarse-grained LLB model we calculate switching probability curves for several high/low T_C grains of different sizes and composites. Additionally, we vary the duration of the applied Gaussian heat pulse and the strength of the applied thermal field. Table 5.2 presents all used parameters and links the corresponding figures (Figs. 5.16 to 5.21) of the comparisons between VAMPIRE and LLB simulations. New correction values according to Sec. 5.6 have to be calculated if the external field or the composite is changed, because these parameters influence the exchange properties at the interface. Hence, changes in the size of the grain or the duration of the heat pulse can be treated without the need of a new correction function. The coarse-grained LLB model with two magnetic moments throughout produces the same switching probabilities as the atomistic model with over 14000 spins. The accordance is very good except for an intermediate intergrain exchange constant of $A_{\text{ex}}(0) = 3.217 \cdot 10^{-12} \text{ J/m}$, where the edge of the switching probability curve is slightly shifted in some cases (Figs. 5.18, 5.19 and 5.21). Nevertheless, the final switching probabilities are still correctly reproduced by the coarse-grained LLB model.

Qualitatively, the data demonstrate that, in case of strong intergrain exchange, the switching probability almost everywhere reaches 100%, if the heat pulse is long enough.

All figures with $t_{\text{pulse}} = 100$ ps have in common that, in case of weak coupling, the switching probability decreases significantly at high peak temperatures and the edge of the probability curve shifts to higher peak temperatures. A very short heat pulse with $t_{\text{pulse}} = 10$ ps yields probabilities below 0.8 independent of the exchange coupling as shown in Fig. 5.17. As expected, under the influence of a higher external field the switching probabilities remain in the vicinity of 1 even for weak coupling in contrast to a field of $\mu_0 H_{\text{ext}} = 0.5$ T. Larger grains increase the switching behavior (Figs. 5.20 and 5.21). In order to get an overview of all calculated curves the switching probabilities with full exchange ($A_{\text{ex}}(0) = 2.575 \cdot 10^{-11}$ J/m) are compared in Fig. 5.22. The grain under the high external field of 0.8 T switches at the lowest peak temperature between 400 and 450 K. The final probability at high temperatures is throughout one. If weaker magnetic fields are given grains with a SM layer with high magnetic moment and low Curie temperature show better switching performance than grains with a SM layer having a low μ_S (high T_C). Especially the grain with the SM1 material and a basal plane diameter of 5 nm does not reach a final switching probability of one. This would be insufficient in bit pattern recording for example, where an incorrect reversal directly leads to a bit error. Here the better choice is a grain with a HM/SM2 composite. In the case of larger grains we detect steeper switching edges than for the corresponding smaller grains. Then the switching has a probability of one for both, SM1 and SM2 layer compounds. However, for high density recording a grain diameter of 10 nm is too large for both, bit patterned media and granular recording. The red curve belonging to the simulations with a short heat pulse of $t_{\text{pulse}} = 10$ ps reveals a very poor switching behavior, and thus such pulses are not recommendable in heat-assisted recording of the presented grains. The dependency of the pulse duration is investigated in the next section in more detail.

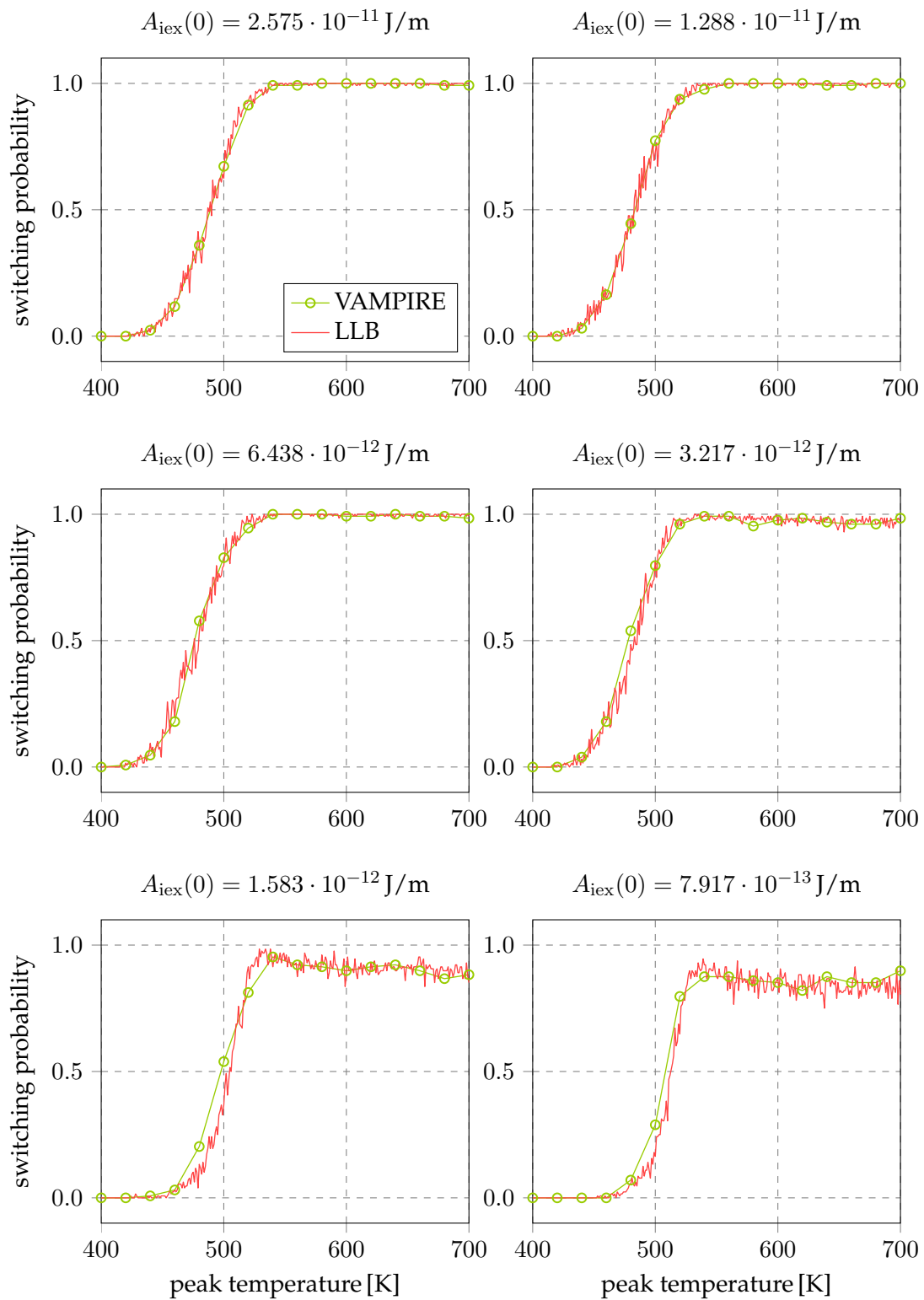


Figure 5.16: Switching probabilities as in Fig. 5.14 with a corrected intergrain exchange field for different $A_{\text{iex}}(0)$. The correction function is constructed as described in Sec. 5.6.

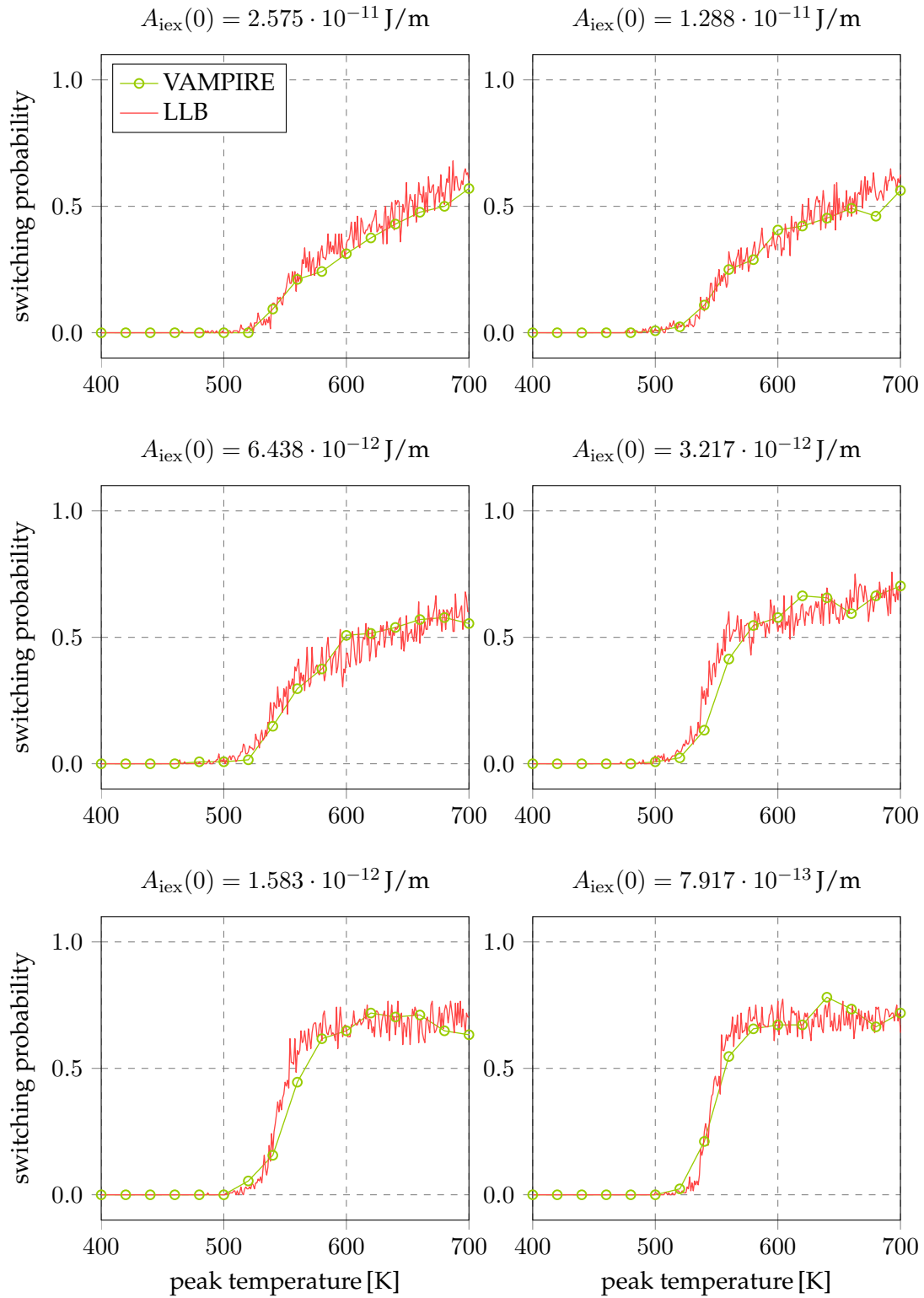


Figure 5.17: Switching probabilities of a cylindrical high/low T_C recording grain for different intergrain exchange constants ($A_{\text{iex},n}(0) = 2.575 \cdot 10^{-11}/2^n \text{ J/m}$, $0 \leq n \leq 5$) subject to a Gaussian heat pulse. The detailed material and simulation parameters are given in Tab. 5.2. The exchange field in the LLB model is corrected as described in Sec. 5.6.

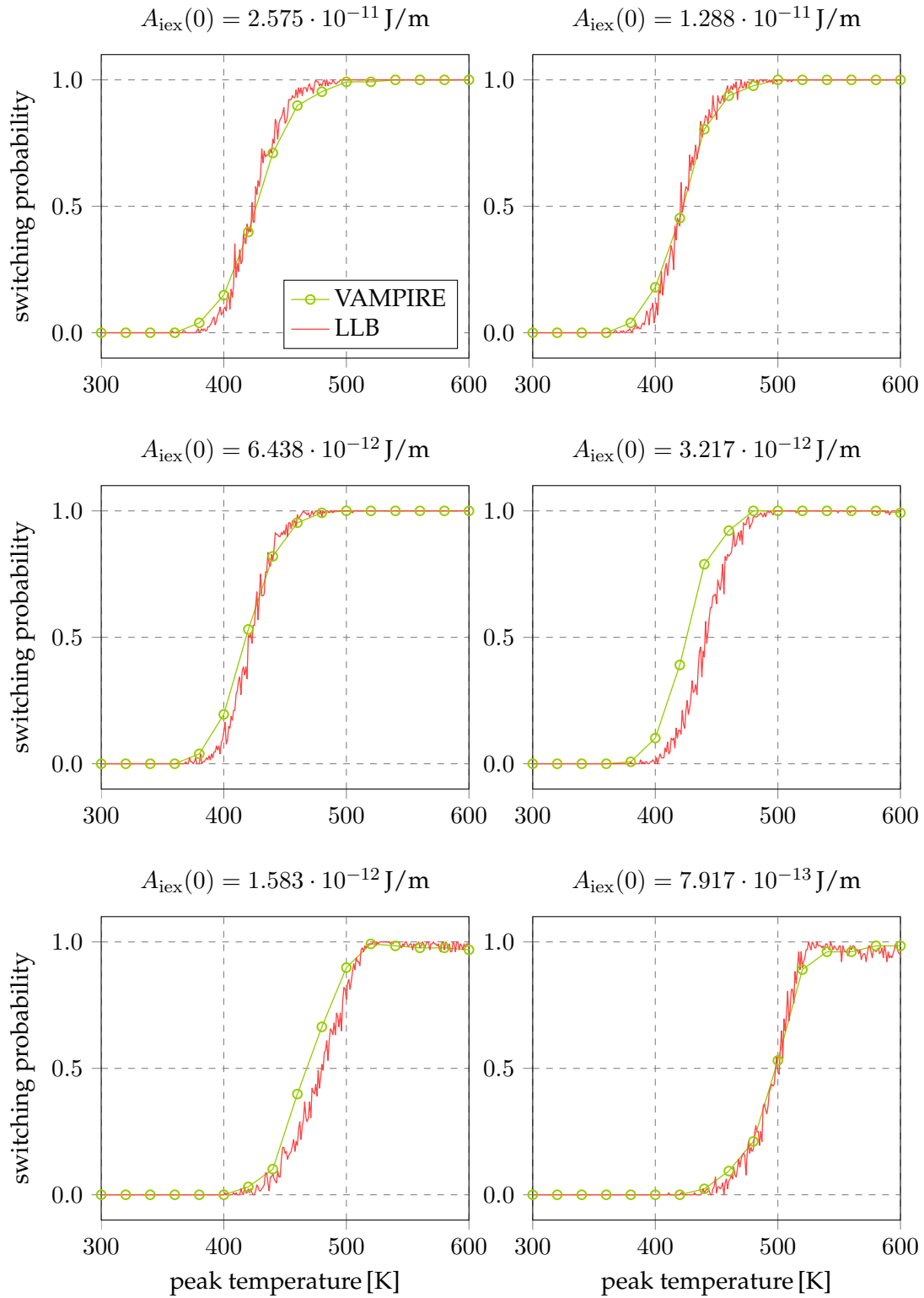


Figure 5.18: Switching probabilities of a cylindrical high/low T_C recording grain for different intergrain exchange constants ($A_{\text{iex},n}(0) = 2.575 \cdot 10^{-11}/2^n \text{ J/m}$, $0 \leq n \leq 5$) subject to a Gaussian heat pulse. The detailed material and simulation parameters are given in Tab. 5.2. The exchange field in the LLB model is corrected as described in Sec. 5.6.

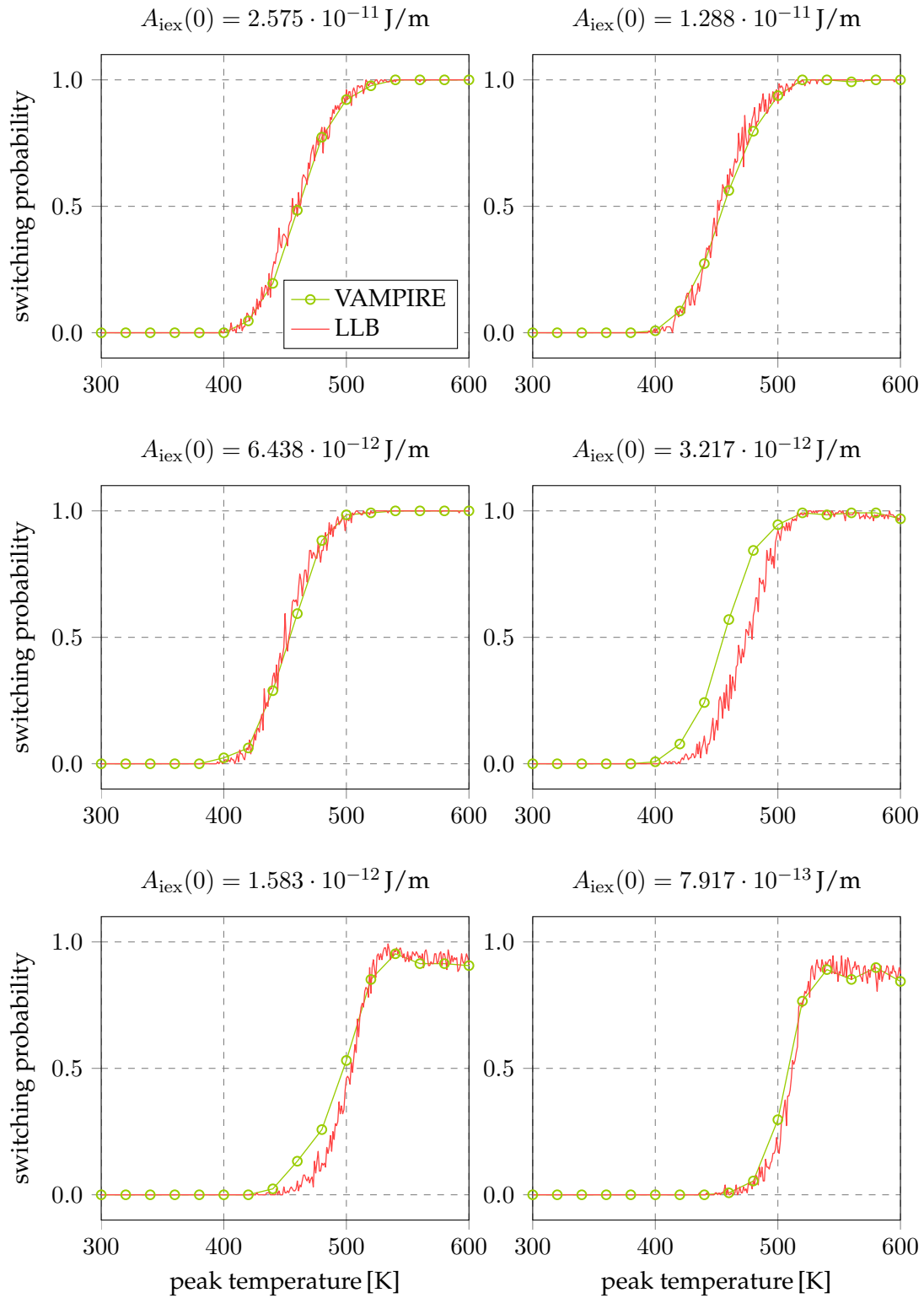


Figure 5.19: Switching probabilities of a cylindrical high/low T_C recording grain for different intergrain exchange constants ($A_{\text{iex},n}(0) = 2.575 \cdot 10^{-11}/2^n \text{ J/m}$, $0 \leq n \leq 5$) subject to a Gaussian heat pulse. The detailed material and simulation parameters are given in Tab. 5.2. The exchange field in the LLB model is corrected as described in Sec. 5.6.

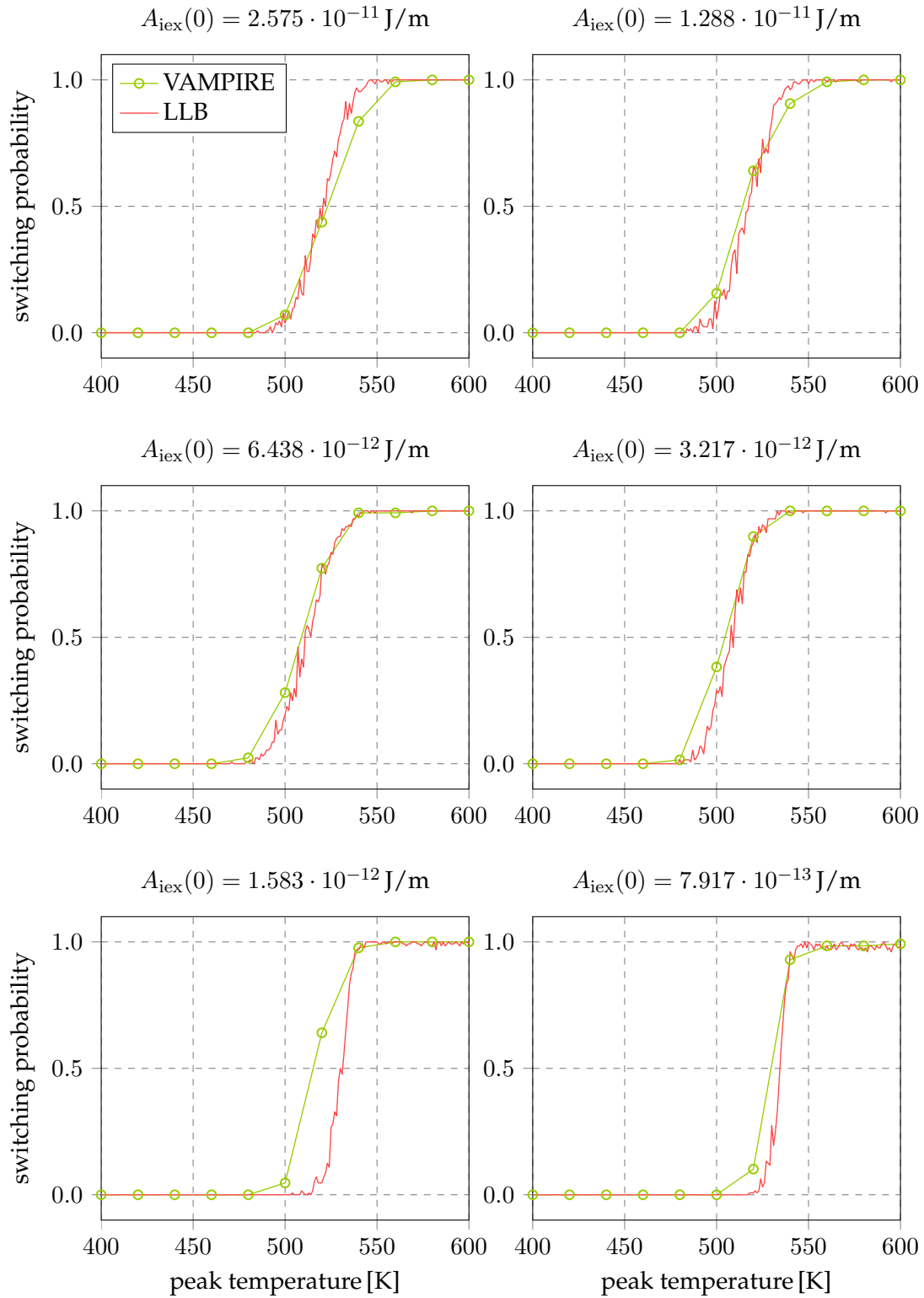


Figure 5.20: Switching probabilities of a cylindrical high/low T_C recording grain for different intergrain exchange constants ($A_{\text{iex},n}(0) = 2.575 \cdot 10^{-11}/2^n \text{ J/m}$, $0 \leq n \leq 5$) subject to a Gaussian heat pulse. The detailed material and simulation parameters are given in Tab. 5.2. The exchange field in the LLB model is corrected as described in Sec. 5.6.

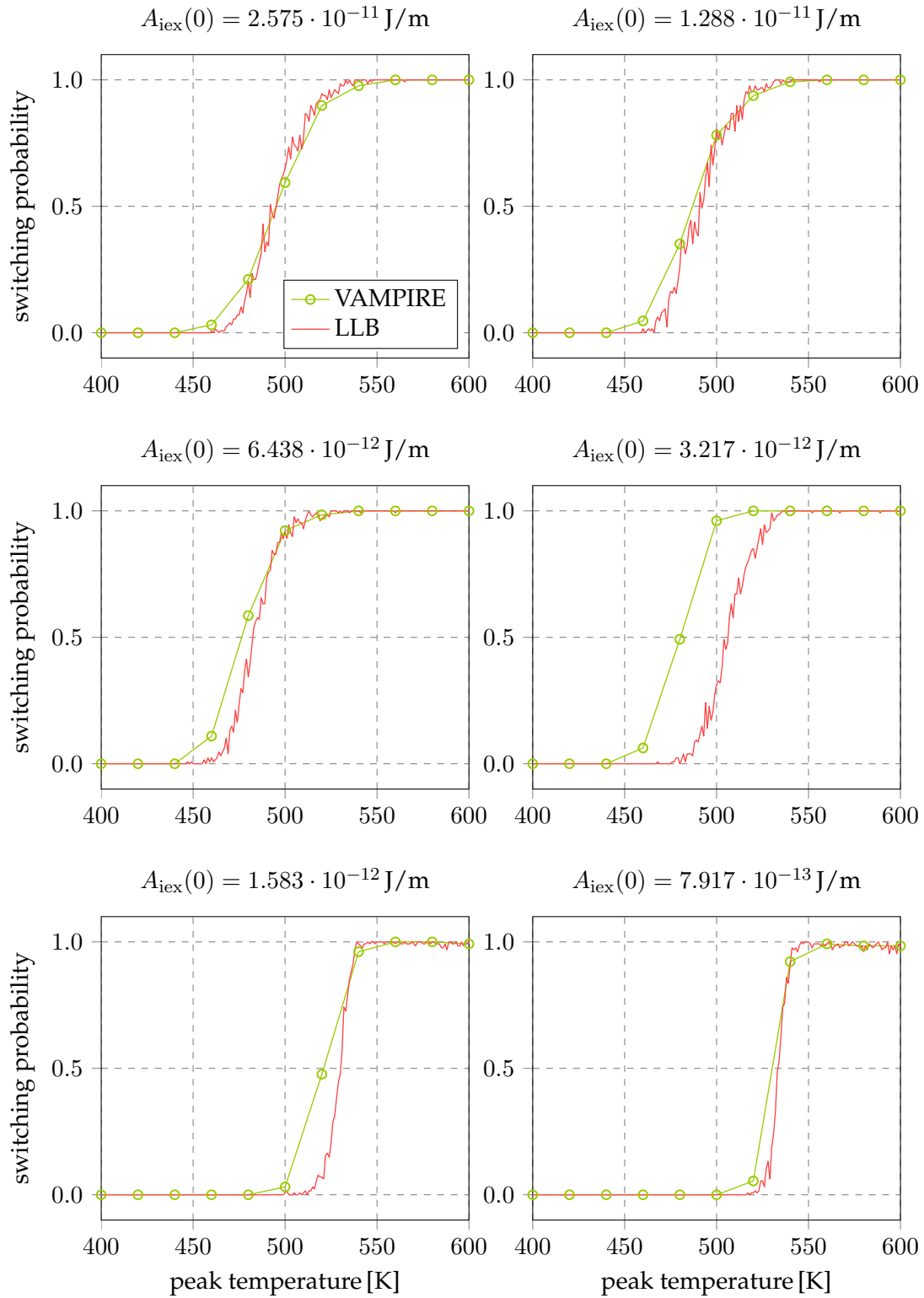


Figure 5.21: Switching probabilities of a cylindrical high/low T_C recording grain for different intergrain exchange constants ($A_{\text{iex},n}(0) = 2.575 \cdot 10^{-11}/2^n \text{ J/m}$, $0 \leq n \leq 5$) subject to a Gaussian heat pulse. The detailed material and simulation parameters are given in Tab. 5.2. The exchange field in the LLB model is corrected as described in Sec. 5.6.

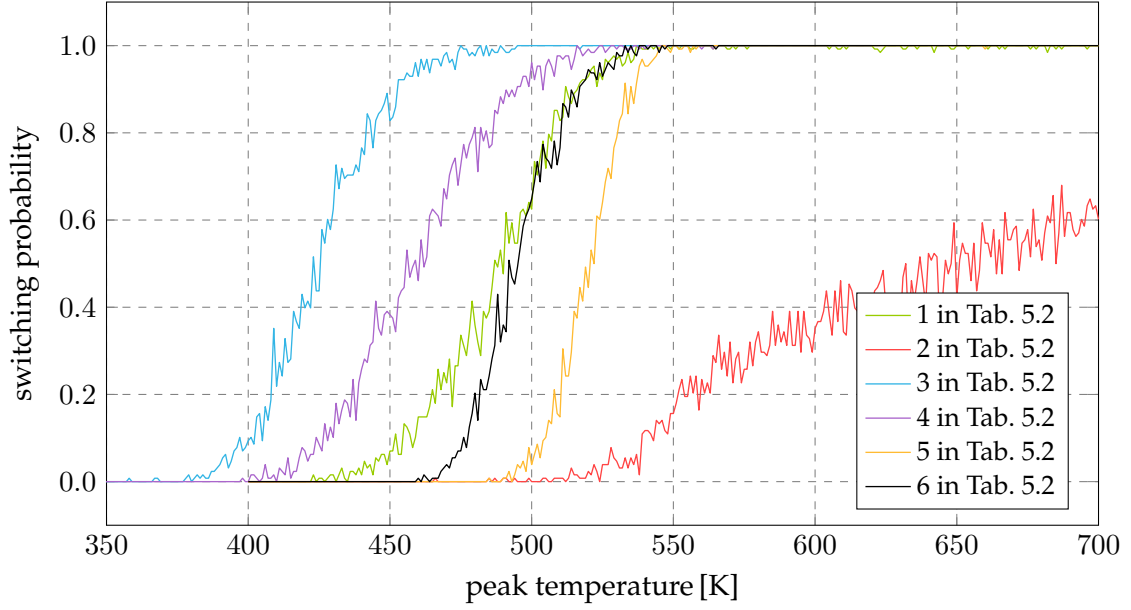


Figure 5.22: Comparison of the switching probability curves with $A_{\text{iex}}(0) = 2.575 \cdot 10^{-11}$ J/m of Figs. 5.16 to 5.21.

5.7.2 Phase diagrams

After validating the coarse-grained LLB model we can benefit from its efficiency and calculate phase diagrams of the switching probability for various high/low T_C grains under different conditions, like varying heat pulse durations or exchange coupling between the layers.

diameter [nm]	SM	$\mu_0 H_{\text{ext}}$ [T]	t_{pulse} [ps]	$A_{\text{iex}}(0)$ [10^{-11} J/m]	figure
5	SM1	0.5	10 – 500	2.575	5.23
5	SM1	0.8	10 – 500	2.575	5.24
5	SM2	0.5	10 – 500	2.575	5.25
10	SM2	0.5	10 – 500	2.575	5.26
5	SM1	0.5	100	0.0515 – 2.575	5.27
5	SM2	0.5	100	0.0515 – 2.575	5.28
10	SM2	0.5	100	0.0515 – 2.575	5.29

Table 5.3: Simulation parameters for the switching probability phase diagrams of Figs. 5.23-5.29. Cylindrical grains consisting of different HM/SM layer combinations subject to an external magnetic field $\mu_0 H_{\text{ext}}$ are used. Besides the variation of the peak temperature of an applied Gaussian heat pulse the pulse duration t_{pulse} or the exchange coupling $A_{\text{iex}}(0)$ between the layers is changed.

In Tab. 5.3 the investigated parameters are summarized. Each diagram contains a total of 4000 phase points. Each point shows the switching probability computed from 128

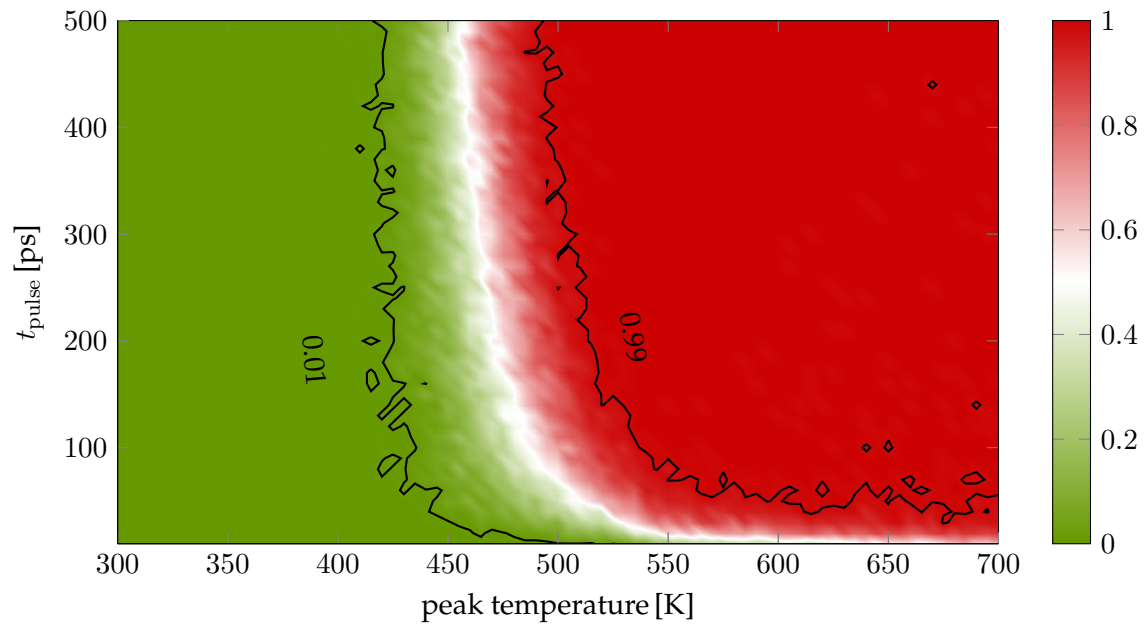


Figure 5.23: Switching probabilities of a HM/SM1 recording grain subject to a Gaussian heat pulse with different lengths t_{pulse} and peak temperatures. The intergrain exchange constant between the layers at zero temperature is $A_{\text{ie}} = 2.575 \cdot 10^{-11}$ J/m. Additionally, an external magnetic field of 0.5 T is applied to the grain. The detailed parameters are presented in Tab. 5.3.

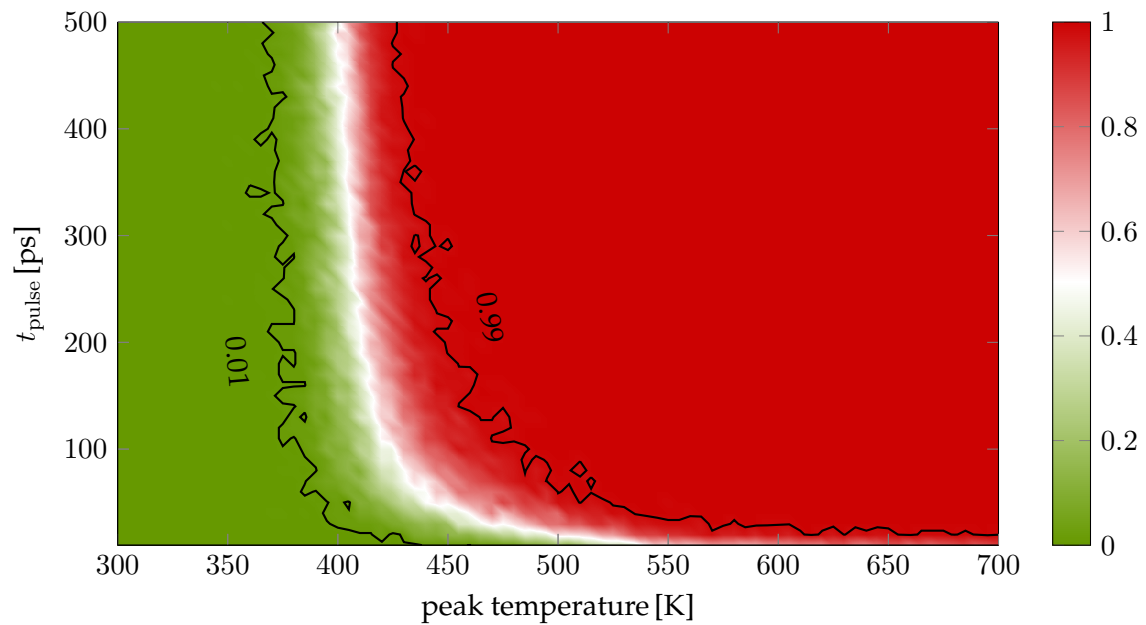


Figure 5.24: Same as Fig. 5.23 with an external magnetic field of 0.8 T. The detailed parameters are presented in Tab. 5.3.

switching trajectories. One trajectory with a pulse duration of $t_{\text{pulse}} = 100$ ps requires almost 35 min of computation time on a single core machine with VAMPIRE while the same simulation finishes within 7 s with the LLB model. Hence, the phase diagrams are

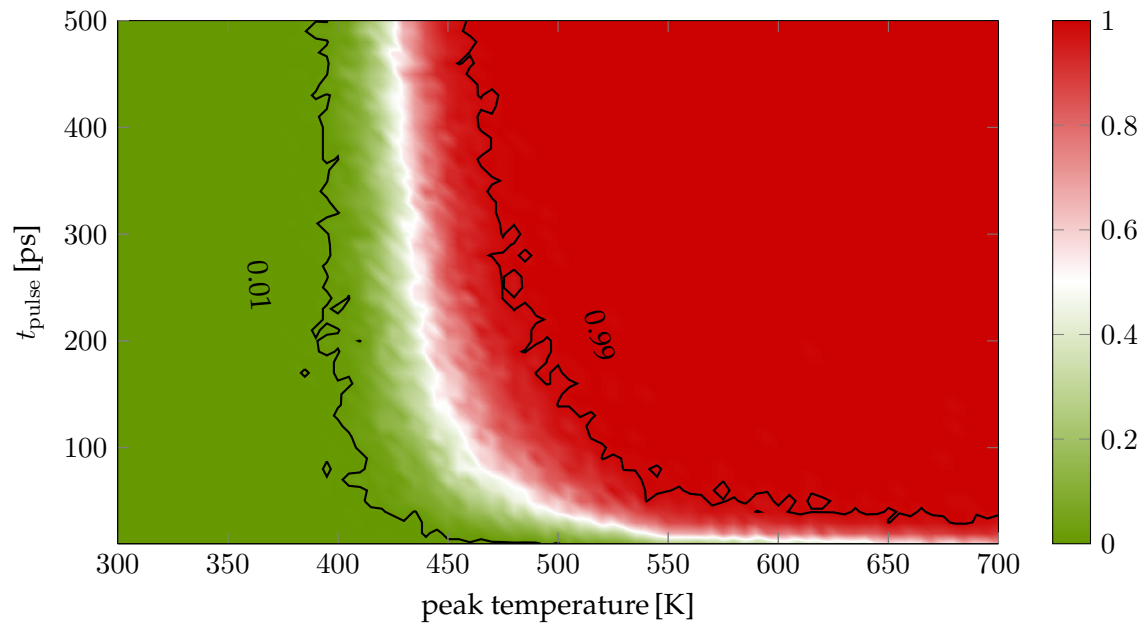


Figure 5.25: Same as Fig. 5.23 for a HM/SM2 recording grain. The detailed parameters are presented in Tab. 5.3.

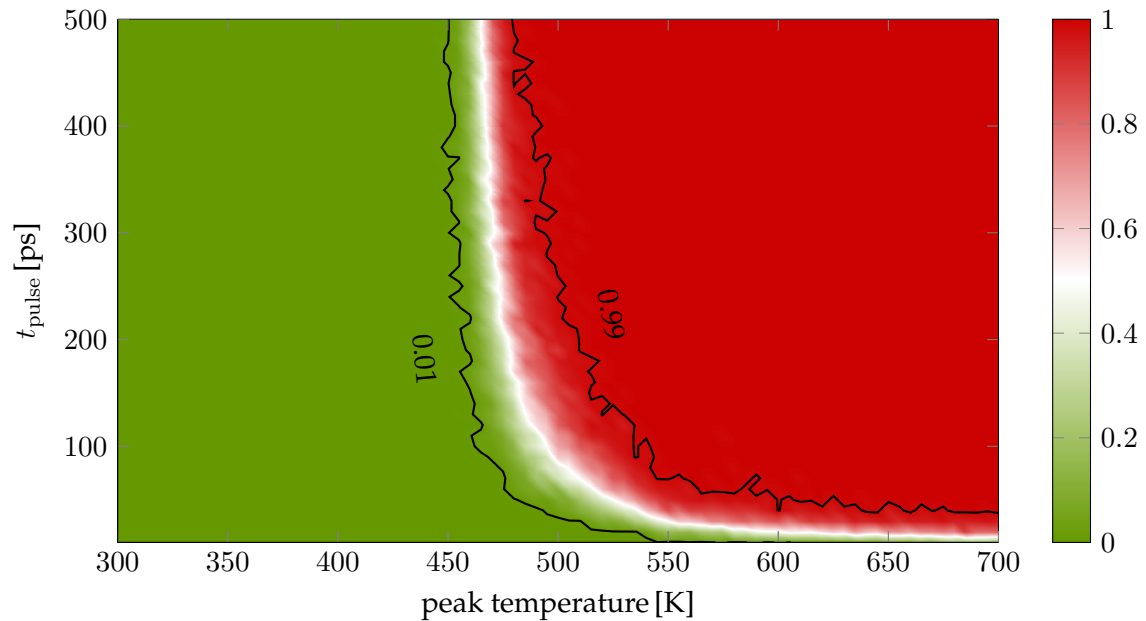


Figure 5.26: Same as Fig. 5.25 for a grain with 10 nm diameter. The detailed parameters are presented in Tab. 5.3.

difficult or even completely impossible to generate with atomistic LLG simulations. Figures 5.23 to 5.26 display that the switching probability does not improve much for field pulses $t_{\text{pulse}} > 100$ ps for both, HM/SM1 grains and HM/SM2 grains, independent of the external field and the grain size. At higher fields of 0.8 T (Fig. 5.24) the switching

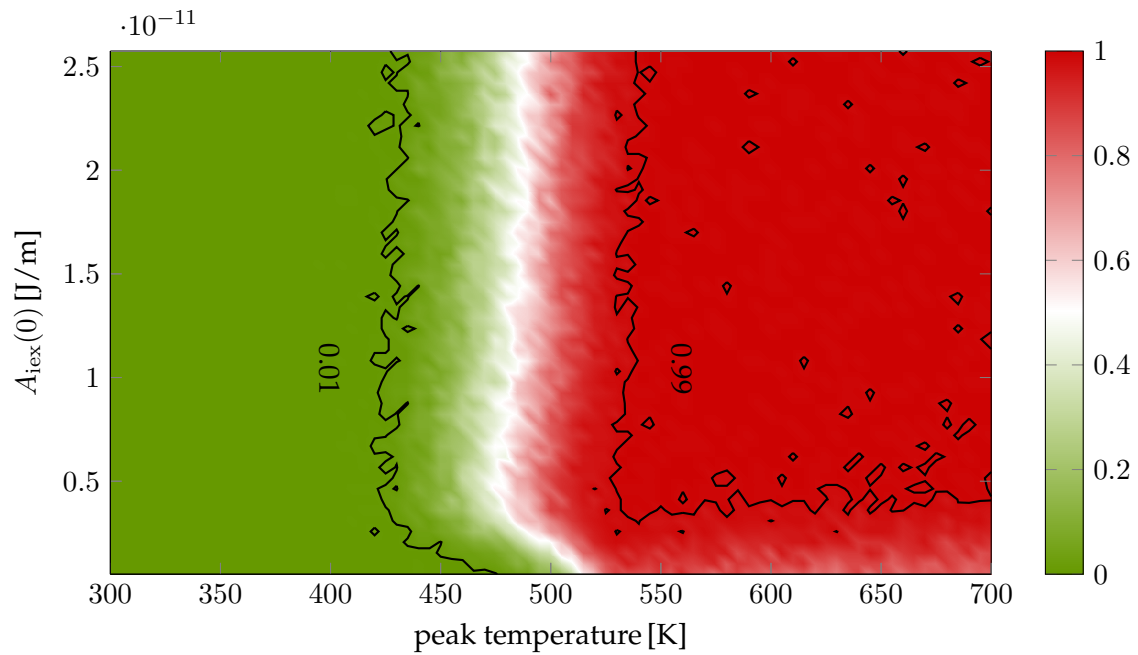


Figure 5.27: Switching probabilities of a HM/SM1 recording grain subject to a Gaussian heat pulse with a duration of $t_{\text{pulse}} = 100$ ps. The intergrain exchange constant between the layers at zero temperature varies from $5.15 \cdot 10^{-13} \text{ J/m} \leq A_{\text{iex}}(0) \leq 2.575 \cdot 10^{-11} \text{ J/m}$ and the peak temperature of the heat pulse varies between $300 \text{ K} \leq T_{\text{peak}} \leq 700 \text{ K}$. Additionally, an external magnetic field of 0.5 T is applied to the grain. The detailed parameters are presented in Tab. 5.3.

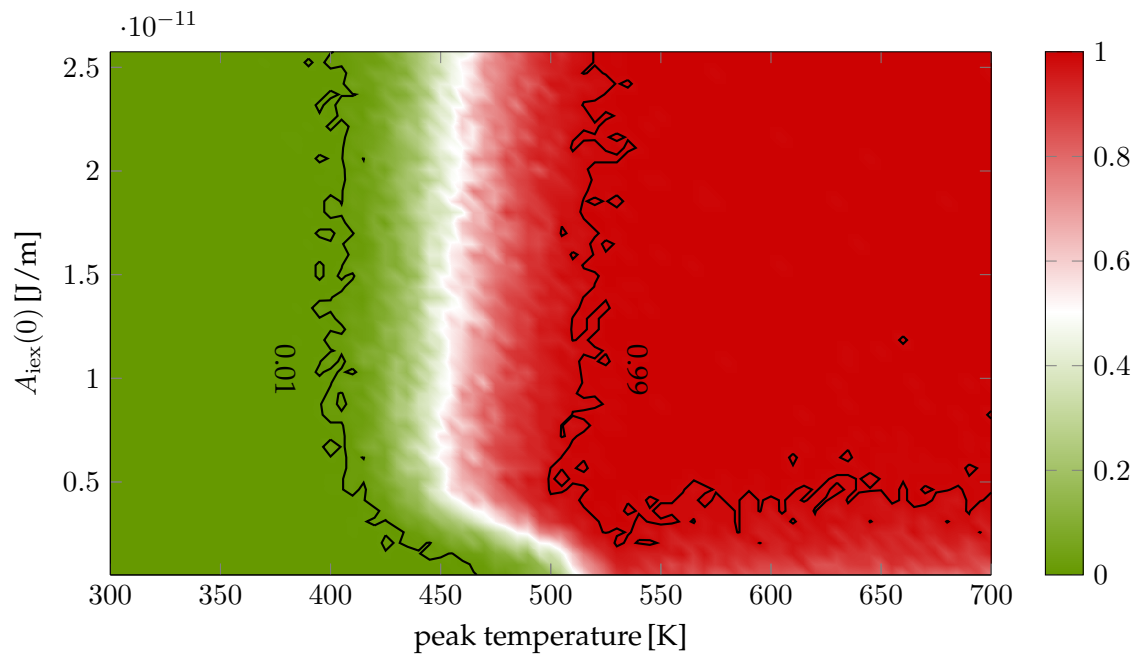


Figure 5.28: Same as Fig. 5.27 for a composite of a HM and a SM2 material. The detailed parameters are presented in Tab. 5.3.

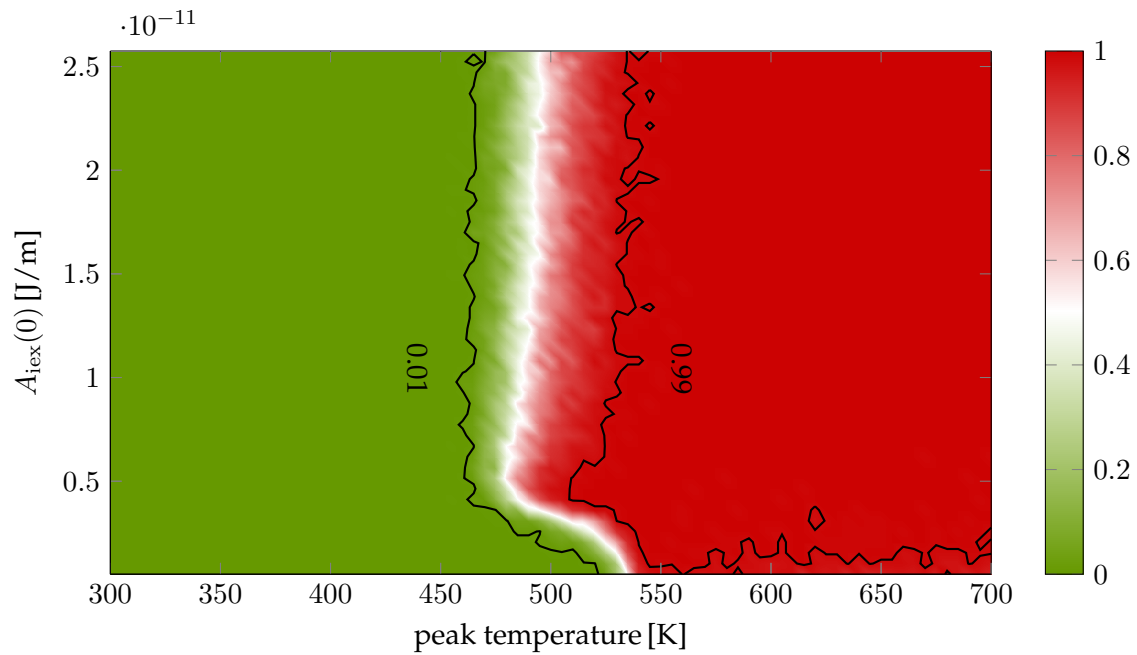


Figure 5.29: Same as Fig. 5.28 for a grain with a basal plane diameter of 10 nm. The detailed parameters are presented in Tab. 5.3.

starts at the lowest temperatures, but the smaller HM/SM2 grain in Fig. 5.25 shows a similar performance. The area, where the actual magnetization reversal takes place, is the most narrow for larger grains (Fig. 5.26), but it is independent of the used material combination if Figs. 5.23 and 5.25 are compared.

The dependence of the switching probability on the exchange interaction between the high and low T_C layers shows a peak at intermediate values of about $A_{iex}(0) = 0.65 \cdot 10^{-11} \text{ J/m}$ (Figs. 5.27, 5.28 and 5.29). This holds for HM/SM1 as well as for HM/SM2 grains of different sizes. Even the switching area is more narrow at intermediate exchange coupling than for large coupling. If $A_{iex}(0)$ decreases beyond $0.4 \cdot 10^{-11} \text{ J/m}$ the switching probability no longer exceeds 0.99. Here the two layers decouple, and thus the switching probability converges to the probability of two separated grains of half size. For the HM/SM1 composite with 5 nm diameter Fig. 5.27 displays that a complete switching of the particle is not guaranteed as indicated by the numerous islands where the probability falls below 0.99. The case is different for the HM/SM2 grain, where complete switching in a wide parameter range occurs as presented in Fig. 5.28. The best result is obtained for a larger grain with a diameter of 10 nm (Fig. 5.29), where the switching edge is very narrow.

The problem in heat-assisted recording is that the magnetic write head cannot be positioned directly over the grain, and thus a field strength of 0.8 T is hard to produce. Unfortunately, grains with 10 nm diameter are too large for high density storage devices,

even in bit patterned media recording. Hence, if an external field of 0.5 T is supposed an optimal heat assistance, which guarantees fast and reliable switching, consists of a pulse with a duration of 100 – 150 ps and a peak temperature of about 575 K. This statement is valid for recording grains made of a composite of HM/SM2 materials with an intermediate exchange coupling of about $A_{\text{iex}}(0) = 0.65 \cdot 10^{-11}$ J/m.

5.8 Media design

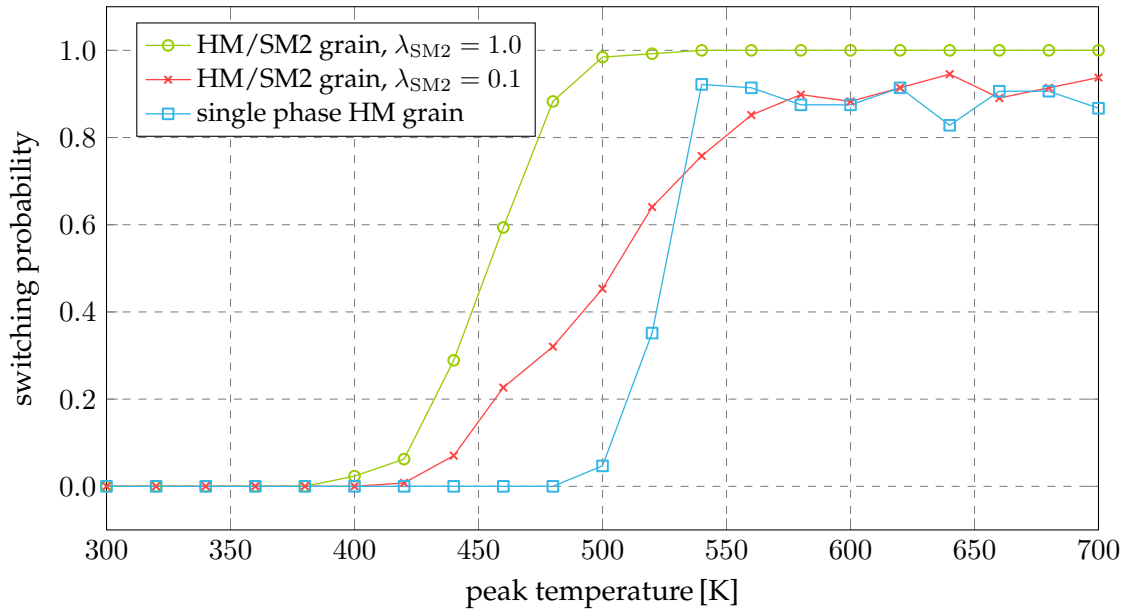


Figure 5.30: Comparison of the switching probability between a single phase HM grain and high/low T_C grains with different damping constants in the soft magnetic layer. The composite grains have an intermediate exchange coupling of $A_{\text{iex}}(0) = 6.438 \cdot 10^{-12}$ J/m. A Gaussian heat pulse with $t_{\text{pulse}} = 100$ ps and an external magnetic field of 0.5 T are applied to all grains.

In the previous section we analyzed the switching probability of high/low T_C grains and its dependency on heat pulse duration, grain size and the strength of the exchange coupling. It turned out that a cylindrical grain with a diameter of 5 nm and a thickness of 10 nm, consisting of 50 % the HM and 50 % the SM2 material, has best recording properties along with a heat pulse of 100 – 150 ps, if an external magnetic field of 0.5 T is given. In the best case the exchange coupling is intermediate with a value of about $A_{\text{iex}}(0) = 6.438 \cdot 10^{-12}$ J/m. Without any discussion we supposed the soft magnetic layer of the grain with high Curie temperature to have a high damping of $\lambda = 1.0$. This is extraordinary, because most realistic materials are described with intermediate damping values between 0.01 and 0.1 in micromagnetism. Especially this high damping value is responsible to significantly increase the switching probability of a grain with different Curie temperatures as Fig. 5.30 proves. Here we compare a single phase

HM grain and two composite HM/SM2 grains with high and low damping in the soft magnetic layer under a heat pulse with $t_{\text{pulse}} = 100$ ps and an applied field of 0.5 T. At first view it is surprising that the composite grain with a damping constant of $\lambda = 0.1$ in the SM layer performs even worse than a single phase HM grain and has a very poor switching probability. If we take a closer look at the magnetization dynamics in both layers it becomes clear. At temperatures above 600 K the magnetization of the HM layer vanishes, but the SM layer still is far away from its Curie point. Since the exchange interaction also vanishes with zero magnetization length of the HM layer, the SM layer is now driven solely by the external field, which tries to switch its magnetization. Due to the small damping constant the reversal is very slow, and thus the external field cannot rotate the magnetization before the temperature of the heat pulse again decreases under the Curie temperature of the HM layer. Since both layers are again coupled at low temperatures ($< T_{C,\text{HM}}$) the HM layer magnetization is biased in its initial direction by the SM layer. This is the reason why the composite grain with low damping in the SM layer has a worse switching probability than the single phase HM grain. In contrast, with a high damping the relaxation is fast enough to complete the magnetization reversal in the SM layer within t_{pulse} . Hence, the HM layer magnetization is biased in the switched direction, which remarkably improves the switching probability of the high/low T_C grain. The edge of the switching curve of the high damping HM/SM2 stack is shifted to much lower temperatures far below the Curie temperature of the HM layer, compared to the single phase grain. Although the slope of the switching edge for the composite grain is lower it is not believed to be a limiting factor at least in bit pattern recording where large temperature differences between neighboring islands are ensured.

In practice, the damping constant of soft magnetic elements can be increased by rare-earth dopants [81]. Hence, the presented composites with different Curie temperatures are possibly the next generation of recording grains in heat-assisted recording of bit patterned media. Without these type of grains heat-assisted recording will have problems with thermally written-in errors [82].

Conclusion and outlook

6.1 Conclusion

In the first part of this thesis it was demonstrated, that the thermal stability of magnetic particles can be predicted accurately and efficiently with the forward flux sampling (FFS) method. To apply FFS, the configuration space between two stable magnetic states is divided using interfaces along the minimum energy path of the magnetic transition. The resulting thermal stabilities are in good agreement with direct Langevin simulations of single-macrospin particles with a low energy barrier. The total simulation time for calculating the thermal stability of magnetic particles, however, is significantly lower when using the FFS method. To illustrate the potential of FFS, the magnetization reversal of a graded media grain with realistic dimensions was simulated. Furthermore it was proven for the first time, that the concept of magnetic grains with graded anisotropy provides very small nanostructures with high thermal stability and low coercivity. The results were obtained without any free parameter via directly integrating the underlying equation of motion. Due to the quadratically increasing anisotropy the grains combine the desired properties of both, soft and hard magnetic parts, without suffering from their disadvantages.

In the second part of this thesis the influence of heat assistance in magnetic recording was investigated. Especially the modeling of an additional write assistance by using grains with high/low T_C layers was a main concern of this work. To deal with high temperatures in the vicinity of the Curie point, a computationally very cheap coarse-grained LLB model was developed. The LLB model treats each magnetic grain as a single magnetization vector. It requires detailed information about the temperature dependence of the zero-field equilibrium magnetization $m_e(T)$, the transverse and par-

allel susceptibilities $\tilde{\chi}_{\perp}(T)$ and $\tilde{\chi}_{\parallel}(T)$ and the intergrain exchange $A_{\text{ie}}(T)$. In addition an exact expression for the intergrain exchange field in the context of this LLB model was derived. It was proven, that the LLB switching probabilities of the coarse-grained model fit atomistic simulation results remarkably well, for strong as well as for weak intergrain exchange coupling. The speed-up of the LLB system compared to the atomistic calculations is formidable, which makes it easy to analyze the detailed influence of different heat pulses or other parameters with low computational effort, even for recording grains of realistic sizes. By means of the coarse-grained LLB model, an optimized grain for heat-assisted recording of bit patterned media was introduced, consisting of a composite of high and low T_C materials. With high damping in the layer with a high Curie temperature, the performance of such a composite grain is much better than that of a single phase grain, and thus heat-assisted recording of bit patterned media can be both, fast and reliable.

6.2 Outlook

The incorporation of forward flux sampling in the coarse-grained Landau-Lifshitz-Bloch model would be a possible task for the future. Consequently, the calculation of the thermal stability of graded media grains as presented in Sec. 4.5 could be significantly accelerated. Some preliminary work would be required to compute the temperature-dependent material functions of all layers in a grain from atomistic simulations. But as soon as the model is fully determined, a realistic recording grain with graded anisotropy could be represented with just a few spins, and thus its thermal stability could be obtained with very low computational effort.

A second very interesting application of the LLB model and forward flux sampling would be the calculation of signal to noise ratios for a whole granular recording medium. Without FFS the switching probability has to be determined by repeated switching trajectories as shown in Sec.5.7, but with FFS one trajectory would be sufficient. However, as presented in Sec. 4.3 FFS is only valid for time-homogeneous Markov systems, in other words memoryless systems with no time dependent external forces. If time dependent forces exist, the system becomes time-inhomogeneous. In this case also transition rates become time dependent. We can imagine such situations during a conventional writing process on a hard disk drive, where a write head moves over the magnetic grains, and thus a time dependent external field is applied to the particles. As long as the movement of the write head is slow enough, the system can locally adapt to the field. Transition rates are time dependent, but the time dependence just enters through the time dependence of the external field. With heat-assisted magnetic recording the

problem is more complicated. The system cannot adapt to the very short applied laser pulse. For such situations a more sophisticated method called non-stationary forward flux sampling (NS-FFS) [83, 84] can be used. It is very similar to FFS and generates a biased set of trajectories, which sample transitions between two states A and B as a function of time for non-stationary stochastic systems. In NS-FFS the phase space is two dimensional, with time as a second coordinate besides the progress coordinate λ , and thus the phase space has to be divided into segments in both dimensions. The aim of NS-FFS is to generate a set of trajectories, which uniformly covers the phase space of interest in time and in λ . Stochastic branching and pruning are used to generate trees of trajectories with dynamically weighted segments. The weighting of the segments allows to sample all parts of the phase space equally, because trajectory segments in low-probability regions are weighted heavier than trajectory segments in high-probability regions.

Jump moments

We want to derive the jump moments $a^{(n)}(x)$ of the FP equation (Eq. 2.3) in terms of

$$a^{(n)}(x) = \lim_{\Delta t \rightarrow 0} \frac{1}{\Delta t} \left\langle [X(t + \Delta t) - X(t)]^n \right\rangle \Big|_{X(t)=x} \quad (\text{A.1})$$

from

$$a^{(n)}(x) = \int_{-\infty}^{\infty} (x' - x)^n W(x'|x) dx'. \quad (\text{A.2})$$

First of all, one has to define the average of $[X(t + \Delta t) - X(t)]^n$ with the initial value $X(t) = x$ as

$$\left\langle [X(t + \tau) - X(t)]^n \right\rangle \Big|_{X(t)=x} = \mathcal{A}_n(x; \tau, t) \quad (\text{A.3})$$

$$= \int_{-\infty}^{\infty} (x' - x)^n P(x', t + \tau | x, t) dx'. \quad (\text{A.4})$$

The short time transition probability $P(x', t + \tau | x, t)$ can be written as

$$P(x', t + \tau | x, t) = \delta(x' - x) [1 - a_0(x)\tau] + W(x'|x)\tau + \mathcal{O}(\tau^2). \quad (\text{A.5})$$

In this equation $W(x'|x)\tau$ is the transition probability from x to x' during the time τ and $a_0(x)$ is the zeroth jump moment. Since the total transition probability from x during the time τ equals $a_0(x)\tau$, the probability that no transition takes place during τ is given by $1 - a_0(x)\tau$. Hence, Eq. A.5 defines the sum of the probability for a transition from x to x' plus the probability that nothing happens during τ . Inserting Eq. A.5 into Eq. A.4 yields

$$\begin{aligned} \mathcal{A}_n(x; \tau, t) &= \tau \int_{-\infty}^{\infty} (x' - x)^n W(x'|x) dx' + \mathcal{O}(\tau^2) \\ &= a^{(n)}(x)\tau + \mathcal{O}(\tau^2). \end{aligned} \quad (\text{A.6})$$

As a consequence the jump moments can be identified with

$$a^{(n)}(x) = \left. \frac{\partial}{\partial \tau} \mathcal{A}_n(x; \tau, t) \right|_{\tau=0}. \quad (\text{A.7})$$

After replacing the partial derivative with a difference quotient and using the definition of $\mathcal{A}_n(x; \tau, t)$ (Eq. A.3), the jump moments have the desired form as follows

$$\begin{aligned} a^{(n)}(x) &= \lim_{\Delta t \rightarrow 0} \frac{\mathcal{A}_n(x; \Delta t, t)}{\Delta t} \\ &= \lim_{\Delta t \rightarrow 0} \frac{1}{\Delta t} \left\langle [X(t + \Delta t) - X(t)]^n \right\rangle \Big|_{X(t)=x}. \end{aligned} \quad (\text{A.8})$$

From LLG to Fokker-Planck

As introduced in Sec. 2.3.2 the general form of a set of Langevin equations with multiplicative noise is

$$\frac{dM_i}{dt} = A_i(\mathbf{M}, t) + \sum_k B_{ik}(\mathbf{M}, t)\xi_k(t), \quad (\text{B.1})$$

where \mathbf{M} is the magnetization of a considered particle. On the other hand the equation of motion of the magnetization of a particle subject to thermal fluctuations is the LLG equation (Eq. 3.46)

$$\frac{d\mathbf{M}}{dt} = -\frac{\gamma\mu_0}{1+\alpha^2} [\mathbf{M} \times (\mathbf{H}_{\text{eff}} + \boldsymbol{\xi})] - \frac{\alpha\gamma\mu_0}{(1+\alpha^2)M_S} \{\mathbf{M} \times [\mathbf{M} \times (\mathbf{H}_{\text{eff}} + \boldsymbol{\xi})]\}. \quad (\text{B.2})$$

If the LLG equation is rearranged that the drift coefficient $A_i(\mathbf{M}, t)$ and diffusion coefficient $B_{ik}(\mathbf{M}, t)$ of the Langevin equation are identifiable, the corresponding Fokker-Planck equation can be reconstructed immediately, according to Eq. 2.20. Here we use the coefficients proposed by Ref. [39] as follows

$$A_i(\mathbf{M}, t) = \left\{ -\frac{\gamma\mu_0}{1+\alpha^2} \mathbf{M} \times \mathbf{H}_{\text{eff}} - \frac{\alpha\gamma\mu_0}{(1+\alpha^2)M_S} \mathbf{M} \times (\mathbf{M} \times \mathbf{H}_{\text{eff}}) \right\}_i \quad (\text{B.3})$$

$$B_{ik}(\mathbf{M}, t) = -\frac{\gamma\mu_0}{1+\alpha^2} \sum_j \varepsilon_{ijk} M_j - \frac{\alpha\gamma\mu_0}{(1+\alpha^2)M_S} (M_i M_k - M_S^2 \delta_{ik}) \quad (\text{B.4})$$

and prove that they yield the correct LLG equation. Inserting the coefficients into the Langevin equation (Eq. B.1) results

$$\begin{aligned} \frac{dM_i}{dt} &= - \left\{ \frac{\gamma\mu_0}{1+\alpha^2} \mathbf{M} \times \mathbf{H}_{\text{eff}} + \frac{\alpha\gamma\mu_0}{(1+\alpha^2)M_S} \mathbf{M} \times (\mathbf{M} \times \mathbf{H}_{\text{eff}}) \right\}_i \\ &\quad - \sum_k \left[\frac{\gamma\mu_0}{1+\alpha^2} \sum_j \varepsilon_{ijk} M_j + \frac{\alpha\gamma\mu_0}{(1+\alpha^2)M_S} (M_i M_k - M_S^2 \delta_{ik}) \right] \xi_k(t). \end{aligned} \quad (\text{B.5})$$

If we use the properties of the double cross product

$$\begin{aligned}
\{\mathbf{M} \times (\mathbf{M} \times \mathbf{H})\}_i &= \sum_{jklm} \varepsilon_{ijk} M_j \varepsilon_{klm} M_l H_m \\
&= \sum_{jklm} \varepsilon_{kij} \varepsilon_{klm} M_j M_l H_m \\
&= \sum_{jlm} (\delta_{il} \delta_{jm} - \delta_{im} \delta_{jl}) M_j M_l H_m \\
&= \sum_m \left(M_m M_i - \sum_l M_l M_l \delta_{im} \right) H_m \\
&= \sum_k (M_k M_i - M_S^2 \delta_{ik}) H_k,
\end{aligned} \tag{B.6}$$

Eq. B.5 becomes

$$\begin{aligned}
\frac{dM_i}{dt} = & - \left\{ \frac{\gamma \mu_0}{1 + \alpha^2} \mathbf{M} \times \mathbf{H}_{\text{eff}} + \frac{\alpha \gamma \mu_0}{(1 + \alpha^2) M_S} \mathbf{M} \times (\mathbf{M} \times \mathbf{H}_{\text{eff}}) \right\}_i \\
& - \left\{ \frac{\gamma \mu_0}{1 + \alpha^2} \mathbf{M} \times \boldsymbol{\xi} + \frac{\alpha \gamma \mu_0}{(1 + \alpha^2) M_S} \mathbf{M} \times (\mathbf{M} \times \boldsymbol{\xi}) \right\}_i,
\end{aligned} \tag{B.7}$$

which illustrates the desired stochastic LLG equation

$$\frac{d\mathbf{M}}{dt} = -\gamma' \mu_0 [\mathbf{M} \times (\mathbf{H}_{\text{eff}} + \boldsymbol{\xi})] - \frac{\alpha \gamma' \mu_0}{M_S} \{\mathbf{M} \times [\mathbf{M} \times (\mathbf{H}_{\text{eff}} + \boldsymbol{\xi})]\}. \tag{B.8}$$

Here the abbreviation $\gamma' = \frac{\gamma}{1 + \alpha^2}$ is used. According to Eq. 2.20 the multivariate Fokker-Planck equation thus has the form

$$\begin{aligned}
\frac{\partial \rho}{\partial t} = & - \sum_i \frac{\partial}{\partial M_i} \left[\left(A_i + D \sum_{jk} B_{jk} \frac{\partial B_{ik}}{\partial M_j} \right) \rho \right] \\
& + \sum_{ij} \frac{\partial^2}{\partial M_i \partial M_j} \left[\left(D \sum_k B_{ik} B_{jk} \right) \rho \right].
\end{aligned} \tag{B.9}$$

If the derivate with respect to M_j is evaluated in the second term of Eq. B.9, the FP equation has the form of a continuity equation

$$\begin{aligned}
\frac{\partial \rho}{\partial t} = & - \sum_i \frac{\partial}{\partial M_i} \left[\left(A_i + D \sum_{jk} B_{jk} \frac{\partial B_{ik}}{\partial M_j} \right) \rho \right] \\
& + \sum_i \frac{\partial}{\partial M_i} \left[D \sum_{jk} \left(\frac{\partial B_{ik}}{\partial M_j} B_{jk} + B_{ik} \frac{\partial B_{jk}}{\partial M_j} + B_{ik} B_{jk} \frac{\partial}{\partial M_j} \right) \rho \right] \\
\frac{\partial \rho}{\partial t} = & - \sum_i \frac{\partial}{\partial M_i} \left[\left(A_i - D \sum_k B_{ik} \sum_j \frac{\partial B_{jk}}{\partial M_j} - D \sum_{jk} B_{ik} B_{jk} \frac{\partial}{\partial M_j} \right) \rho \right].
\end{aligned} \tag{B.10}$$

The sum $\sum_j \frac{\partial B_{jk}}{\partial M_j}$ in the second term can be simplified with the definition of B_{ik} (Eq. B.4)

$$\begin{aligned}
\sum_i \frac{\partial B_{ik}}{\partial M_i} &= \sum_i \frac{\partial}{\partial M_i} \left[-\gamma' \mu_0 \sum_j \varepsilon_{ijk} M_j - \frac{\alpha \gamma' \mu_0}{M_S} (M_i M_k - M_S^2 \delta_{ik}) \right] \\
&= -\gamma' \mu_0 \sum_{ij} \varepsilon_{ijk} \delta_{ij} - \frac{\alpha \gamma' \mu_0}{M_S} \sum_i \left(\delta_{ii} M_k + M_i \delta_{ik} - 2 \sum_l \delta_{il} M_l \delta_{ik} \right) \\
&= -\gamma' \mu_0 \sum_i \varepsilon_{iik} - \frac{\alpha \gamma' \mu_0}{M_S} (3M_k + M_k - 2M_k) \\
&= -2 \frac{\alpha \gamma' \mu_0}{M_S} M_k. \tag{B.11}
\end{aligned}$$

Using this expression in Eq. B.10 cancels the whole second term

$$\begin{aligned}
\sum_k B_{ik} \sum_j \frac{\partial B_{jk}}{\partial M_j} &= -2 \frac{\alpha \gamma' \mu_0}{M_S} \sum_k \left[-\gamma' \mu_0 \sum_j \varepsilon_{ijk} M_j - \frac{\alpha \gamma' \mu_0}{M_S} (M_i M_k - M_S^2 \delta_{ik}) \right] M_k \\
&= 2 \frac{\alpha \gamma' \mu_0}{M_S} \sum_{jk} \gamma' \mu_0 \varepsilon_{ijk} M_j M_k + 2 \frac{\alpha \gamma' \mu_0}{M_S} \left(\sum_k M_i M_k M_k - \sum_k M_S^2 \delta_{ik} M_k \right) \\
&= 2 \frac{\alpha \gamma' \mu_0}{M_S} (M_i M_S^2 - M_S^2 M_i) = 0 \tag{B.12}
\end{aligned}$$

The third term on the right-hand side of Eq. B.10 also simplifies to

$$\begin{aligned}
D \sum_{jk} B_{ik} B_{jk} \frac{\partial \rho}{\partial M_j} &= D \sum_{jk} \left[-\gamma' \mu_0 \sum_l \varepsilon_{ilk} M_l - \frac{\alpha \gamma' \mu_0}{M_S} (M_i M_k - M_S^2 \delta_{ik}) \right] \\
&\quad \cdot \left[-\gamma' \mu_0 \sum_n \varepsilon_{jnk} M_n - \frac{\alpha \gamma' \mu_0}{M_S} (M_j M_k - M_S^2 \delta_{jk}) \right] \frac{\partial \rho}{\partial M_j} \\
&= D \left[\gamma'^2 \mu_0^2 \sum_{jkl n} \varepsilon_{ilk} M_l \varepsilon_{jnk} M_n \right. \\
&\quad + \frac{\alpha \gamma'^2 \mu_0^2}{M_S} \sum_{jlk} \varepsilon_{ilk} M_l (M_j M_k - M_S^2 \delta_{jk}) \\
&\quad + \frac{\alpha \gamma'^2 \mu_0^2}{M_S} \sum_{jnk} \varepsilon_{jnk} M_n (M_i M_k - M_S^2 \delta_{ik}) \\
&\quad \left. + \left(\frac{\alpha \gamma' \mu_0}{M_S} \right)^2 \sum_{jk} (M_i M_k - M_S^2 \delta_{ik}) (M_j M_k - M_S^2 \delta_{jk}) \right] \frac{\partial \rho}{\partial M_j}
\end{aligned}$$

$$\begin{aligned}
D \sum_{jk} B_{ik} B_{jk} \frac{\partial \rho}{\partial M_j} &= D \left[\gamma'^2 \mu_0^2 \sum_{jln} (\delta_{ij} \delta_{ln} - \delta_{in} \delta_{lj}) M_l M_n \right. \\
&\quad + \frac{\alpha \gamma'^2 \mu_0^2}{M_S} \left(\sum_{jlk} \varepsilon_{ilk} M_j M_l M_k \overset{0}{-} \sum_{jl} \varepsilon_{ilj} M_S^2 \right) \\
&\quad + \frac{\alpha \gamma'^2 \mu_0^2}{M_S} \left(\sum_{jnk} \varepsilon_{jnk} M_i M_n M_k \overset{0}{-} \sum_{jn} \varepsilon_{jni} M_S^2 \right) \\
&\quad \left. + \left(\frac{\alpha \gamma' \mu_0}{M_S} \right)^2 \sum_{jk} (M_i M_k M_j M_k - M_i M_k M_S^2 \delta_{jk} - M_j M_k M_S^2 \delta_{ik} + M_S^4 \delta_{ik} \delta_{jk}) \right] \frac{\partial \rho}{\partial M_j} \\
&= D \left[\gamma'^2 \mu_0^2 \left(\sum_{jl} \delta_{ij} M_l M_l - \sum_{jk} M_j M_i \right) \right. \\
&\quad + \frac{\alpha \gamma'^2 \mu_0^2}{M_S} \sum_{jl} \left(-\varepsilon_{ilj} M_S^2 - \varepsilon_{jli} M_S^2 \right) \\
&\quad \left. + \left(\frac{\alpha \gamma' \mu_0}{M_S} \right)^2 \left(\sum_i M_i M_j M_S^2 - \sum_i M_i M_j M_S^2 - \sum_j M_j M_i M_S^2 + \sum_{jk} M_S^4 \delta_{ik} \delta_{jk} \right) \right] \frac{\partial \rho}{\partial M_j} \\
&= D \left[\gamma'^2 \mu_0^2 \sum_j (\delta_{ij} M_S^2 - M_j M_i) \right. \\
&\quad \left. + (\alpha \gamma' \mu_0)^2 \sum_j (-M_j M_i + M_S^2 \delta_{ij}) \right] \frac{\partial \rho}{\partial M_j} \\
&= -D \gamma'^2 \mu_0^2 (1 + \alpha^2) \sum_j (M_i M_j - \delta_{ij} M_S^2) \frac{\partial \rho}{\partial M_j} \\
&= -D \gamma'^2 \mu_0^2 (1 + \alpha^2) \left[\mathbf{M} \times \left(\mathbf{M} \times \frac{\partial \rho}{\partial \mathbf{M}} \right) \right]_i. \tag{B.13}
\end{aligned}$$

Hence, the probability distribution of the magnetization \mathbf{M} becomes

$$\begin{aligned}
\frac{\partial \rho}{\partial t} &= - \sum_i \frac{\partial}{\partial M_i} \left[\left(A_i - D \sum_{jk} B_{ik} B_{jk} \frac{\partial}{\partial M_j} \right) \rho \right] \\
&= - \sum_i \frac{\partial}{\partial M_i} \left\{ \left[-\gamma' \mu_0 \mathbf{M} \times \mathbf{H}_{\text{eff}} - \frac{\alpha \gamma' \mu_0}{M_S} \mathbf{M} \times (\mathbf{M} \times \mathbf{H}_{\text{eff}}) \right. \right. \\
&\quad \left. \left. + D \gamma'^2 \mu_0^2 (1 + \alpha^2) \mathbf{M} \times \left(\mathbf{M} \times \frac{\partial}{\partial \mathbf{M}} \right) \right] \rho \right\}_i \\
\Rightarrow \frac{\partial \rho}{\partial t} &= - \frac{\partial}{\partial \mathbf{M}} \cdot \left\{ \left[-\frac{\gamma \mu_0}{1 + \alpha^2} \mathbf{M} \times \mathbf{H}_{\text{eff}} - \frac{\alpha \gamma \mu_0}{(1 + \alpha^2) M_S} \mathbf{M} \times (\mathbf{M} \times \mathbf{H}_{\text{eff}}) \right. \right. \\
&\quad \left. \left. + \frac{D \gamma^2 \mu_0^2}{1 + \alpha^2} \mathbf{M} \times \left(\mathbf{M} \times \frac{\partial}{\partial \mathbf{M}} \right) \right] \rho \right\}. \tag{B.14}
\end{aligned}$$

Thermal field strength in the LLG

Starting point for the derivation of the strength of the thermal fluctuations ξ is the FP equation (Eq. B.14) of the LLG equation, describing the probability distribution of the magnetization M

$$\frac{\partial \rho}{\partial t} = -\frac{\partial}{\partial M} \cdot \left\{ \left[-\frac{\gamma \mu_0}{1 + \alpha^2} \mathbf{M} \times \mathbf{H}_{\text{eff}} - \frac{\alpha \gamma \mu_0}{(1 + \alpha^2) M_S} \mathbf{M} \times (\mathbf{M} \times \mathbf{H}_{\text{eff}}) + \frac{D \gamma^2 \mu_0^2}{1 + \alpha^2} \mathbf{M} \times \left(\mathbf{M} \times \frac{\partial}{\partial M} \right) \right] \rho \right\}. \quad (\text{C.1})$$

If the magnetic system is in thermal equilibrium the probability distribution ρ equals the Boltzmann distribution

$$\rho_0 = e^{-\beta E_{\text{tot}}}, \quad (\text{C.2})$$

where β is the inverse thermal energy $(k_B T)^{-1}$ and E_{tot} is the total energy of the system, consisting of exchange energy E_{exc} , anisotropy energy E_{ani} , demagnetization energy E_{demag} and Zeeman energy E_{zee}

$$\begin{aligned} E_{\text{tot}} &= E_{\text{exc}} + E_{\text{ani}} + E_{\text{demag}} + E_{\text{zee}} \\ &= \frac{\mathcal{J} S^2 c}{a} \int [(\nabla m_x)^2 + (\nabla m_y)^2 + (\nabla m_z)^2] dv \\ &\quad + \int K_1 [1 - (\mathbf{e}_{\text{easy}} \cdot \hat{\mathbf{m}})^2] dv \\ &\quad - \frac{\mu_0 M_S}{2} \int \hat{\mathbf{m}} \cdot \mathbf{H}_{\text{demag}} dv \\ &\quad - \mu_0 M_S \int \hat{\mathbf{m}} \cdot \mathbf{H}_{\text{ext}} dv. \end{aligned} \quad (\text{C.3})$$

Here $\hat{\mathbf{m}} = \frac{M}{M_S}$ is the magnetization normalized by the saturation magnetization. In a discretized system the total energy of the system is related to the effective field with

Eq. D.17, resulting in

$$\frac{\partial \rho_0}{\partial \mathbf{M}} = -\beta \frac{\partial E_{\text{tot}}}{\partial \mathbf{M}} \rho_0 = -\beta (-\mu_0 v \mathbf{H}_{\text{eff}}) \rho_0 = \mu_0 \beta v \mathbf{H}_{\text{eff}} \rho_0, \quad (\text{C.4})$$

where v is the volume of a discretization cell. In thermal equilibrium where $\rho = \rho_0$ holds the first term in Eq. C.1 vanishes

$$\begin{aligned} & -\frac{\partial}{\partial \mathbf{M}} \cdot \left(-\frac{\gamma \mu_0}{1 + \alpha^2} \mathbf{M} \times \mathbf{H}_{\text{eff}} \rho_0 \right) \\ &= \frac{\gamma}{(1 + \alpha^2) \beta v} \frac{\partial}{\partial \mathbf{M}} \cdot \left(\mathbf{M} \times \frac{\partial \rho_0}{\partial \mathbf{M}} \right) \\ &= \frac{\gamma}{(1 + \alpha^2) \beta v} \frac{\partial}{\partial M_i} \sum_{jk} \left(\varepsilon_{ijk} M_j \frac{\partial}{\partial M_k} \rho_0 \right) \\ &= \frac{\gamma}{(1 + \alpha^2) \beta v} \sum_{jk} \left(\varepsilon_{ijk} \delta_{ij} \frac{\partial}{\partial M_k} \rho_0 + \varepsilon_{ijk} M_j \frac{\partial}{\partial M_i} \frac{\partial}{\partial M_k} \rho_0 \right) \\ &= \frac{\gamma}{(1 + \alpha^2) \beta v} \left(\sum_k \varepsilon_{ikk} \frac{\partial}{\partial M_k} \rho_0 + \sum_{jk} M_j \varepsilon_{ijk} \frac{\partial}{\partial M_i} \frac{\partial}{\partial M_k} \rho_0 \right) = 0. \end{aligned} \quad (\text{C.5})$$

The second term in Eq. C.5 is identical zero, because the product of a totally antisymmetric tensor with a totally symmetric tensor vanishes. For $\rho = \rho_0$, Eq. C.1 becomes

$$\begin{aligned} \frac{\partial \rho_0}{\partial t} = -\frac{\partial}{\partial \mathbf{M}} \cdot \left[-\frac{\alpha \gamma}{(1 + \alpha^2) M_S \beta v} \mathbf{M} \times \left(\mathbf{M} \times \frac{\partial \rho_0}{\partial \mathbf{M}} \right) \right. \\ \left. + \frac{D \gamma^2 \mu_0^2}{(1 + \alpha^2)} \mathbf{M} \times \left(\mathbf{M} \times \frac{\partial \rho_0}{\partial \mathbf{M}} \right) \right] = 0. \end{aligned} \quad (\text{C.6})$$

This equation is just solvable if

$$\left[-\frac{\alpha \gamma}{(1 + \alpha^2) M_S \beta v} \mathbf{M} \times \left(\mathbf{M} \times \frac{\partial \rho_0}{\partial \mathbf{M}} \right) + \frac{D \gamma^2 \mu_0^2}{(1 + \alpha^2)} \mathbf{M} \times \left(\mathbf{M} \times \frac{\partial \rho_0}{\partial \mathbf{M}} \right) \right] = 0, \quad (\text{C.7})$$

is valid, yielding

$$\frac{\alpha \gamma}{(1 + \alpha^2) M_S \beta v} = \frac{D \gamma^2 \mu_0^2}{(1 + \alpha^2)}. \quad (\text{C.8})$$

The strength of the thermal field (or diffusion constant) thus becomes

$$D = \frac{\alpha}{\gamma \mu_0^2 M_S \beta v}. \quad (\text{C.9})$$

Effective magnetic field

D.1 The continuous system

In a continuous system the effective magnetic field is defined as follows

$$\mathbf{H}_{\text{eff}} = -\frac{1}{\mu_0 M_S} \frac{\delta E_{\text{tot}}[\hat{\mathbf{m}}]}{\delta \hat{\mathbf{m}}}. \quad (\text{D.1})$$

Since the total energy E_{tot} is a functional of the magnetization, $\frac{\delta E_{\text{tot}}}{\delta \hat{\mathbf{m}}}$ is a functional derivative. To execute Eq. D.1 we need to know how to correctly work with functional derivatives.

Lemma 1. *Let V be a Hilbert-Space. Let $L : V \rightarrow \mathbb{R}$ be the linear functional*

$$L[f] = \int F(f(r)) dr.$$

Let $F : \mathbb{R} \rightarrow \mathbb{R}$ be a function, which is at least one time continuously differentiable. Then the functional derivative is

$$\frac{\delta L[f]}{\delta f} = \frac{\partial F(f)}{\partial f} = F'(f).$$

Proof. The derivate of a linear functional $L[f]$ can be expressed with the difference quotient

$$\frac{\delta L[f(r)]}{\delta f(\xi)} = \lim_{\substack{\Delta f \rightarrow 0 \\ \Delta \xi \rightarrow 0}} \frac{L[f(r) + \Delta f h(r; \xi, \Delta \xi)] - L[f(r)]}{\Delta f \Delta \xi}.$$

Since $f(r)$ is a continuous function its deviation around the argument ξ in the difference quotient has to be written with a window function $h(r; \xi, \Delta \xi)$, which is defined as

$$h(r; \xi, \Delta \xi) = \begin{cases} 1, & \text{if } r \text{ is in the interval } \Delta \xi \text{ around } \xi \\ 0, & \text{else.} \end{cases}$$

With these definitions it follows

$$\begin{aligned}
\frac{\delta L[f]}{\delta f} &= \frac{\delta}{\delta f(\xi)} \int F(f(r)) dr = \int \frac{\delta F(f(r))}{\delta f(\xi)} dr = \int \frac{\partial F(f)}{\partial f} \frac{\delta f(r)}{\delta f(\xi)} dr \\
&= \int \frac{\partial F(f)}{\partial f} \lim_{\substack{\Delta f \rightarrow 0 \\ \Delta \xi \rightarrow 0}} \frac{f(r) + \Delta f h(r; \xi, \Delta \xi) - f(r)}{\Delta f \Delta \xi} dr \\
&= \int \frac{\partial F(f)}{\partial f} \lim_{\Delta \xi \rightarrow 0} \frac{h(r; \xi, \Delta \xi)}{\Delta \xi} dr \\
&= \int \frac{\partial F(f)}{\partial f} \delta(r - \xi) dr \\
&= \frac{\partial F(f)}{\partial f} = F'(f).
\end{aligned}$$

□

Lemma 2. Let V be a Hilbert-Space. Let $L : V \rightarrow \mathbb{R}$ be a linear functional and let $f : \mathbb{R} \rightarrow \mathbb{R}$ be a function, which is at least one time continuously differentiable $f'(r) = \partial_r f(r)$. Then the functional derivative of L and ∂_r are permutable and it applies

$$\frac{\delta L[f']}{\delta f} = -\partial_r \frac{\delta L[f']}{\delta f'}.$$

Proof.

$$\begin{aligned}
\frac{\delta L[f']}{\delta f} &= \frac{\delta}{\delta f(\xi)} \int F(f'(r)) dr = \int \frac{\delta F(f'(r))}{\delta f(\xi)} dr = \int \frac{\partial F(f')}{\partial f'} \frac{\delta f'(r)}{\delta f(\xi)} dr \\
&= \int \frac{\partial F(f')}{\partial f'} \lim_{\substack{\Delta f \rightarrow 0 \\ \Delta \xi \rightarrow 0}} \frac{f'(r) + \Delta f h'(r; \xi, \Delta \xi) - f'(r)}{\Delta f \Delta \xi} dr \\
&= \int \frac{\partial F(f')}{\partial f'} \lim_{\Delta \xi \rightarrow 0} \frac{h'(r; \xi, \Delta \xi)}{\Delta \xi} dr \\
&= \int \frac{\partial F(f')}{\partial f'} \frac{\partial}{\partial r} \lim_{\Delta \xi \rightarrow 0} \frac{h(r; \xi, \Delta \xi)}{\Delta \xi} dr \\
&= \int \frac{\partial F(f')}{\partial f'} \frac{\partial}{\partial r} \delta(r - \xi) dr
\end{aligned}$$

After partial integration the derivation of the delta function can be transferred to $\frac{\partial F(f')}{\partial f'}$

$$\begin{aligned}
\int \frac{\partial F(f')}{\partial f'} \frac{\partial}{\partial r} \delta(r - \xi) dr &= \frac{\partial F(f')}{\partial f'} \delta(r - \xi) \Big|_{\partial \Omega} - \int \frac{\partial}{\partial r} \frac{\partial F(f')}{\partial f'} \delta(r - \xi) dr \\
&= \frac{\partial F(f')}{\partial f'} \delta(r - \xi) \Big|_{\partial \Omega} - \frac{\partial}{\partial r} \frac{\partial F(f')}{\partial f'}.
\end{aligned}$$

Since the first term on the right-hand side is zero, if ξ is within the integration limits, the expression $\frac{\delta L[f']}{\delta f}$ can be simplified to

$$\frac{\delta L[f']}{\delta f} = -\frac{\partial}{\partial r} \frac{\partial F(f')}{\partial f'} = -\partial_r \frac{\partial F(f')}{\partial f'}$$

□

In contrast to the original derivation of the effective magnetic field, using the variation of the magnetization \mathbf{M} with the restriction of a constant length of the vector $M^2 = M_S^2$, the functional derivative of the total energy with respect to the magnetization (Eq. D.1) has to be taken without this constraint. This means that the cartesian components of the magnetization (m_x, m_y, m_z) are independent of each other. In the following each contribution of the effective magnetic field is calculated separately.

D.1.1 Exchange field

The x -component of the exchange field is

$$\begin{aligned} H_{\text{exc},x} &= -\frac{\mathcal{J}S^2c}{a\mu_0M_S} \frac{\delta}{\delta m_x} \int \left[(\nabla m_x(\mathbf{r}))^2 + (\nabla m_y(\mathbf{r}))^2 + (\nabla m_z(\mathbf{r}))^2 \right] d^3\mathbf{r} \\ &= -\frac{\mathcal{J}S^2c}{a\mu_0M_S} \frac{\delta}{\delta m_x} \int \left[\left(\frac{\partial}{\partial \mathbf{r}} m_x(\mathbf{r}) \right)^2 \right] d^3\mathbf{r}. \end{aligned} \quad (\text{D.2})$$

According to the previously defined lemmas it simplifies to

$$\begin{aligned} H_{\text{exc},x} &= -\frac{\mathcal{J}S^2c}{a\mu_0M_S} \frac{\delta}{\delta m_x} \int (m'_x)^2 d^3\mathbf{r} \\ &\stackrel{\text{L. 2}}{=} +\frac{\mathcal{J}S^2c}{a\mu_0M_S} \frac{\partial}{\partial \mathbf{r}} \frac{\delta}{\delta m'_x} \int (m'_x)^2 d^3\mathbf{r} \\ &\stackrel{\text{L. 1}}{=} \frac{\mathcal{J}S^2c}{a\mu_0M_S} \frac{\partial}{\partial \mathbf{r}} \frac{\partial}{\partial m'_x} (m'_x)^2 \\ &= \frac{2\mathcal{J}S^2c}{a\mu_0M_S} \frac{\partial}{\partial \mathbf{r}} m'_x = \frac{2\mathcal{J}S^2c}{a\mu_0M_S} \Delta m_x. \end{aligned} \quad (\text{D.3})$$

Thus, the complete exchange field has the compact form

$$\mathbf{H}_{\text{exc}} = \frac{2\mathcal{J}S^2c}{a\mu_0M_S} \Delta \hat{\mathbf{m}}. \quad (\text{D.4})$$

D.1.2 Anisotropy field

By means of Lemma 1 the anisotropy field is trivial to calculate as follows

$$\begin{aligned} \mathbf{H}_{\text{ani}} &= -\frac{K_1}{\mu_0M_S} \frac{\delta}{\delta \hat{\mathbf{m}}} \int \left[1 - (\mathbf{e}_{\text{easy}} \cdot \hat{\mathbf{m}}(\mathbf{r}))^2 \right] d^3\mathbf{r} \\ &\stackrel{\text{L. 1}}{=} -\frac{K_1}{\mu_0M_S} \frac{\partial}{\partial \hat{\mathbf{m}}} \left[1 - (\mathbf{e}_{\text{easy}} \cdot \hat{\mathbf{m}})^2 \right] \\ &= \frac{2K_1}{\mu_0M_S} (\mathbf{e}_{\text{easy}} \cdot \hat{\mathbf{m}}) \cdot \mathbf{e}_{\text{easy}}. \end{aligned} \quad (\text{D.5})$$

D.1.3 Demagnetization field

Lemma 1 can also be used to evaluate the demagnetization field

$$\begin{aligned}
 \mathbf{H}_{\text{demag}} &= \frac{1}{2} \frac{\delta}{\delta \mathbf{M}} \int \mathbf{M}(\mathbf{r}) \cdot \mathbf{H}_{\text{demag}} d^3 \mathbf{r} \\
 &\stackrel{\text{L. 1}}{=} \frac{1}{2} \frac{\partial}{\partial \mathbf{M}} (\mathbf{M} \cdot \mathbf{H}_{\text{demag}}) \\
 &= \frac{1}{2} \mathbf{H}_{\text{demag}} + \frac{1}{2} \mathbf{M} \frac{\partial \mathbf{H}_{\text{demag}}}{\partial \mathbf{M}},
 \end{aligned} \tag{D.6}$$

yielding the following identity after integrating both sides over the whole space

$$\int \mathbf{H}_{\text{demag}} d^3 \mathbf{r} = \int \mathbf{M} \frac{\partial \mathbf{H}_{\text{demag}}}{\partial \mathbf{M}} d^3 \mathbf{r}. \tag{D.7}$$

For convenience the label in the demagnetization field is suppressed from now on. To proof Eq. D.7 the magnetization is replaced by $\mathbf{M} = \frac{\mathbf{B}}{\mu_0} - \mathbf{H}$

$$\begin{aligned}
 \int \mathbf{M} \frac{\partial \mathbf{H}}{\partial \mathbf{M}} d^3 \mathbf{r} &= \int \left(\frac{\mathbf{B}}{\mu_0} - \mathbf{H} \right) \frac{\partial \mathbf{H}}{\partial \mathbf{M}} d^3 \mathbf{r} \\
 &= \frac{1}{\mu_0} \int \mathbf{B} \frac{\partial \mathbf{H}}{\partial \mathbf{M}} d^3 \mathbf{r} - \int \mathbf{H} \frac{\partial \mathbf{H}}{\partial \mathbf{M}} d^3 \mathbf{r} \\
 &= \frac{1}{\mu_0} \frac{\partial}{\partial \mathbf{M}} \int \mathbf{B} \cdot \mathbf{H} d^3 \mathbf{r} - \frac{1}{\mu_0} \int \frac{\partial \mathbf{B}}{\partial \mathbf{M}} \mathbf{H} d^3 \mathbf{r} - \int \mathbf{H} \frac{\partial \mathbf{H}}{\partial \mathbf{M}} d^3 \mathbf{r}.
 \end{aligned} \tag{D.8}$$

The integral $\int \mathbf{B} \cdot \mathbf{H} d^3 \mathbf{r}$ vanishes. This can be shown if the magnetic field is written with the gradient of a scalar potential $\mathbf{H} = -\nabla U$, which is the most general solution of the Maxwell equation $\nabla \times \mathbf{H} = 0$

$$\begin{aligned}
 \int \mathbf{B} \cdot \mathbf{H} d^3 \mathbf{r} &= - \int \mathbf{B} \cdot \nabla U d^3 \mathbf{r} \\
 &= - \int \nabla \cdot (\mathbf{B} U) d^3 \mathbf{r} + \int \nabla \cdot \mathbf{B} U d^3 \mathbf{r} \\
 &= - \oint U \mathbf{B} \cdot \mathbf{n} dS = 0.
 \end{aligned} \tag{D.9}$$

The last integral is an integral over a surface, which contains the whole ferromagnet. Hence, it is possible to increase the surface to infinity without changing the integral. Outside the ferromagnet $\mathbf{B} = \mu_0 \mathbf{H} = -\mu_0 \nabla U$ tends to zero at least as fast as $1/r^2$. So the product $U \mathbf{B}$ tends to zero at least with $1/r^3$. dS just increases with r^2 and so the whole integral vanishes at infinity. We can simplify Eq. D.8 furthermore if we use again

the relation $\mathbf{H} = -\nabla U$ as follows

$$\begin{aligned}
\int M \frac{\partial \mathbf{H}}{\partial M} d^3 \mathbf{r} &= -\frac{1}{\mu_0} \int \frac{\partial \mathbf{B}}{\partial M} \mathbf{H} d^3 \mathbf{r} - \int \mathbf{H} \frac{\partial \mathbf{H}}{\partial M} d^3 \mathbf{r} \\
&= \frac{1}{\mu_0} \int \frac{\partial \mathbf{B}}{\partial M} \nabla U d^3 \mathbf{r} - \int \mathbf{H} \frac{\partial \mathbf{H}}{\partial M} d^3 \mathbf{r} \\
&= \frac{1}{\mu_0} \int \nabla \left(\frac{\partial \mathbf{B}}{\partial M} U \right) d^3 \mathbf{r} - \frac{1}{\mu_0} \int \frac{\partial}{\partial M} (\nabla \cdot \mathbf{B}) U d^3 \mathbf{r} - \int \mathbf{H} \frac{\partial \mathbf{H}}{\partial M} d^3 \mathbf{r} \\
&= \frac{1}{\mu_0} \oint U \frac{\partial \mathbf{B}}{\partial M} \mathbf{n} dS - \int \mathbf{H} \frac{\partial \mathbf{H}}{\partial M} d^3 \mathbf{r} \\
&= - \int \mathbf{H} \frac{\partial \mathbf{H}}{\partial M} d^3 \mathbf{r}.
\end{aligned} \tag{D.10}$$

The surface integral $\oint U \frac{\partial \mathbf{B}}{\partial M} \mathbf{n} dS$ vanishes for the same reason that applies to Eq. D.9. After these calculations we obtain the identity

$$\int M \frac{\partial \mathbf{H}}{\partial M} d^3 \mathbf{r} = - \int \mathbf{H} \frac{\partial \mathbf{H}}{\partial M} d^3 \mathbf{r}. \tag{D.11}$$

The same result follows from

$$\begin{aligned}
\int \frac{\partial M}{\partial M} \mathbf{H} d^3 \mathbf{r} &= \int \frac{\partial}{\partial M} \left(\frac{\mathbf{B}}{\mu_0} - \mathbf{H} \right) \mathbf{H} d^3 \mathbf{r} \\
&= \frac{1}{\mu_0} \int \frac{\partial \mathbf{B}}{\partial M} \mathbf{H} d^3 \mathbf{r} - \int \frac{\partial \mathbf{H}}{\partial M} \mathbf{H} d^3 \mathbf{r},
\end{aligned} \tag{D.12}$$

where the first integral in the last line equals zero as already illustrated in Eq. D.10. Hence, it can be written

$$\int M \frac{\partial \mathbf{H}}{\partial M} d^3 \mathbf{r} = - \int \mathbf{H} \frac{\partial \mathbf{H}}{\partial M} d^3 \mathbf{r} = \int \frac{\partial M}{\partial M} \mathbf{H} d^3 \mathbf{r} = \int \mathbf{H} d^3 \mathbf{r}, \tag{D.13}$$

which was to be proven.

D.2 The discrete system

In a discretized system the normalized magnetization $\hat{\mathbf{m}} = \frac{M}{M_S}$, the demagnetizing field $\mathbf{H}_{\text{demag}}$ and the external field \mathbf{H}_{ext} are supposed to be constant within one mesh cell. Hence, the last three volume integrals in Eq. 4.5 can immediately be executed in each computational cell σ with volume V_σ

$$E_{\text{ani}} = +K_1 V_\sigma \left[1 - (\mathbf{e}_{\text{easy}} \cdot \hat{\mathbf{m}}_\sigma)^2 \right] \tag{D.14}$$

$$E_{\text{demag}} = -\frac{\mu_0 M_S V_\sigma}{2} \hat{\mathbf{m}}_\sigma \cdot \mathbf{H}_{\text{demag},\sigma} \tag{D.15}$$

$$E_{\text{zee}} = -\mu_0 M_S V_\sigma \hat{\mathbf{m}}_\sigma \cdot \mathbf{H}_{\text{ext},\sigma}. \tag{D.16}$$

A similar simplification is not possible for the exchange energy E_{ex} , because it would vanish if only one computational cell is considered. The exchange energy arises, according to its name, from the exchange interaction of neighboring spins. For the derivation

of \mathbf{H}_{exc} it is thus necessary to look at the actual discretization schema of the system, as will be shown in Sec. D.2.1. The effective magnetic field \mathbf{H}_{eff} is computed as the derivative of the total energy with respect to the magnetization within one computational cell

$$\mathbf{H}_{\text{eff},\sigma} = -\frac{1}{\mu_0 M_S V_\sigma} \frac{\partial E_{\text{tot},\sigma}}{\partial \hat{\mathbf{m}}_\sigma}. \quad (\text{D.17})$$

This expression is the counterpart of Eq. D.1 in the discrete system. The evaluation of Eq. D.17 for the individual energy contributions is shown in detail in the next sections.

D.2.1 Exchange field

As already mentioned, the derivation of the exchange field depends on the used discretization schema for

$$E_{\text{exc}} = \frac{\mathcal{J} S^2 c}{a} \int \left[(\nabla m_x)^2 + (\nabla m_y)^2 + (\nabla m_z)^2 \right] dV. \quad (\text{D.18})$$

A finite difference and a finite element approach are considered in the following.

Finite element approach

If the magnetic moment in each direction is replaced with the finite element ansatz

$$m = \sum_i m_i \phi_i(x, y, z), \quad (\text{D.19})$$

Eq. D.18 becomes

$$\begin{aligned} E_{\text{exc}} = \frac{\mathcal{J} S^2 c}{a} \int & \left[\nabla \left(\sum_i m_{i,x} \phi_i(x, y, z) \right) \right]^2 \\ & + \left[\nabla \left(\sum_i m_{i,y} \phi_i(x, y, z) \right) \right]^2 \\ & + \left[\nabla \left(\sum_i m_{i,z} \phi_i(x, y, z) \right) \right]^2 dV. \end{aligned} \quad (\text{D.20})$$

The exchange field in x -direction is

$$\begin{aligned}
H_{\text{exc},\sigma_x} &= -\frac{1}{\mu_0 M_S V_\sigma} \frac{\partial E_{\text{exc}}}{\partial m_{\sigma,x}} \\
&= -\frac{1}{\mu_0 M_S V_\sigma} \frac{\mathcal{J} S^2 c}{a} \int 2\nabla \left(\sum_i m_{i,x} \phi_i(x, y, z) \right) \frac{\partial}{\partial m_{\sigma,x}} \nabla \left(\sum_i m_{i,x} \phi_i(x, y, z) \right) dV \\
&= -\frac{2}{\mu_0 M_S V_\sigma} \frac{\mathcal{J} S^2 c}{a} \int \nabla \left(\sum_i m_{i,x} \phi_i(x, y, z) \right) \nabla \left[\sum_i \delta_{i\sigma} \phi_i(x, y, z) \right] dV \\
&= -\frac{2}{\mu_0 M_S V_\sigma} \frac{\mathcal{J} S^2 c}{a} \int \nabla m_x \nabla \phi_\sigma(x, y, z) dV \\
&= -\frac{2}{\mu_0 M_S V_\sigma} \frac{\mathcal{J} S^2 c}{a} \left\{ \int \nabla \left[\nabla m_x \phi_\sigma(x, y, z) \right] dV - \int \Delta m_x \phi_\sigma(x, y, z) dV \right\} \\
&= -\frac{2}{\mu_0 M_S V_\sigma} \frac{\mathcal{J} S^2 c}{a} \left\{ \oint \frac{\partial m_x}{\partial \mathbf{n}} \phi_\sigma(x, y, z) dS - \int \Delta m_x \phi_\sigma(x, y, z) dV \right\}. \quad (\text{D.21})
\end{aligned}$$

In the first integral on the right-hand side of the last line we use Gauss's integral theorem. Since there exist no sinks and sources of magnetization inside a computational cell the surface integral vanishes, yielding

$$\begin{aligned}
H_{\text{exc},\sigma_x} &= \frac{1}{V_\sigma} \frac{2\mathcal{J} S^2 c}{a\mu_0 M_S} \int \Delta m_x \phi_\sigma(x, y, z) dV \\
&= \frac{1}{V_\sigma} \frac{2\mathcal{J} S^2 c}{a\mu_0 M_S} \Delta m_{\sigma_x} V_\sigma. \quad (\text{D.22})
\end{aligned}$$

In the last step the properties of the test-function $\phi_\sigma(x, y, z)$ are used, which is one at the computational node σ and zero at all other nodes. Thus, $\int \Delta m_x \phi_\sigma(x, y, z) dV$ equals $\Delta m_{\sigma_x} V_\sigma$. Since the result is the same for the other two cartesian components, the total exchange field in one computational cell has the compact form

$$\mathbf{H}_{\text{exc}} = \frac{2\mathcal{J} S^2 c}{a\mu_0 M_S} \Delta \hat{\mathbf{m}}. \quad (\text{D.23})$$

Finite difference approach

Without loss of generality, first of all we evaluate the discretization of the first term on the right-hand side of

$$(\nabla m_x)^2 = \left(\frac{\partial m_x}{\partial x} \right)^2 + \left(\frac{\partial m_x}{\partial y} \right)^2 + \left(\frac{\partial m_x}{\partial z} \right)^2. \quad (\text{D.24})$$

Afterwards it is trivial to extend that result to all other terms in the exchange energy. If the arithmetic mean of one forward and one backward differential quotient is used for the discretization process Eq D.24 becomes

$$\left(\frac{\partial m_x(x, y, z)}{\partial x} \right)^2 = \frac{1}{2} \left(\frac{m_{i+1,j,k} - m_{i,j,k}}{\Delta x} \right)^2 + \frac{1}{2} \left(\frac{m_{i,j,k} - m_{i-1,j,k}}{\Delta x} \right)^2. \quad (\text{D.25})$$

This procedure yields a second order differential quotient. The three indices i, j, k represent the lattice points in the x, y, z -directions of the magnetic moments. To obtain the exchange field, the derivative of the above expression with respect to the magnetic moment has to be taken

$$\begin{aligned}
\int \frac{\partial}{\partial m_x} \left(\frac{\partial m_x}{\partial x} \right)^2 dV &= \sum_{ijk} \frac{\partial}{\partial m_{l,m,n}} \frac{1}{2} \left[\left(\frac{m_{i+1,j,k} - m_{i,j,k}}{\Delta x} \right)^2 + \left(\frac{m_{i,j,k} - m_{i-1,j,k}}{\Delta x} \right)^2 \right] \Delta x \Delta y \Delta z \\
&= \sum_{ijk} \frac{1}{2} \left[2 \left(\frac{m_{i+1,j,k} - m_{i,j,k}}{\Delta x} \right) \left(\frac{\delta_{(i+1)l} - \delta_{il}}{\Delta x} \right) \right. \\
&\quad \left. + 2 \left(\frac{m_{i,j,k} - m_{i-1,j,k}}{\Delta x} \right) \left(\frac{\delta_{il} - \delta_{(i-1)l}}{\Delta x} \right) \right] \delta_{jm} \delta_{kn} \Delta x \Delta y \Delta z \\
&= \frac{1}{\Delta x^2} \left[m_{l,m,n} - \sum_i m_{i,m,n} \delta_{(i+1)l} - m_{l+1,m,n} + m_{l,m,n} + m_{l,m,n} \right. \\
&\quad \left. - \sum_i m_{i,m,n} \delta_{(i-1)l} - m_{l-1,m,n} + m_{l,m,n} \right] \Delta x \Delta y \Delta z \\
&= \frac{1}{\Delta x^2} \left[4m_{l,m,n} - m_{l+1,m,n} - m_{l-1,m,n} \right. \\
&\quad \left. - \sum_{i-1} m_{i-1,m,n} \delta_{(i-1+1)l} - \sum_{i+1} m_{i+1,m,n} \delta_{(i+1-1)l} \right] \Delta x \Delta y \Delta z \\
&= \frac{4m_{l,m,n} - 2m_{l+1,m,n} - 2m_{l-1,m,n}}{\Delta x^2} \Delta x \Delta y \Delta z \\
&= -2V_\sigma \frac{m_{l+1,m,n} - 2m_{l,m,n} + m_{l-1,m,n}}{\Delta x^2}. \tag{D.26}
\end{aligned}$$

We expect the same outcome for $\left(\frac{\partial m_x}{\partial y} \right)^2$ and $\left(\frac{\partial m_x}{\partial z} \right)^2$ if Δx is replaced with Δy and Δz . The sum of all terms calculates to

$$\int \frac{\partial}{\partial m_x} (\nabla m_x)^2 dV = -2V_\sigma \left[\frac{m_{i+1,j,k} - 2m_{i,j,k} + m_{i-1,j,k}}{\Delta x^2} \right. \\
\frac{m_{i+1,j,k} - 2m_{i,j,k} + m_{i-1,j,k}}{\Delta y^2} \\
\left. \frac{m_{i+1,j,k} - 2m_{i,j,k} + m_{i-1,j,k}}{\Delta z^2} \right] = -2\Delta m_x V_\sigma. \tag{D.27}$$

Since the derivation is equivalent for the y - and z -component of the exchange field we finally obtain the following expression for the exchange field

$$\begin{aligned}
\mathbf{H}_{\text{exc}} &= -\frac{1}{\mu_0 M_S V_\sigma} \frac{\partial E_{\text{exc}}}{\partial \hat{\mathbf{m}}} \\
&= \frac{1}{V_\sigma} \frac{2\mathcal{J}S^2 c}{a\mu_0 M_S} \Delta \hat{\mathbf{m}} V_\sigma \\
&= \frac{2\mathcal{J}S^2 c}{a\mu_0 M_S} \Delta \hat{\mathbf{m}}. \tag{D.28}
\end{aligned}$$

From the physical point of view it is not surprising that the exchange field is independent of the discretization schema and that it is also equivalent for continuous and discrete systems (compare Eqs. D.4, D.23 and D.28).

D.2.2 Anisotropy field

The anisotropy field is computed to

$$\begin{aligned}\mathbf{H}_{\text{ani}} &= -\frac{K_1}{\mu_0 M_S} \frac{\partial}{\partial \hat{\mathbf{m}}} \left[1 - (\mathbf{e}_{\text{easy}} \cdot \hat{\mathbf{m}})^2 \right] \\ &= \frac{2K_1}{\mu_0 M_S} (\mathbf{e}_{\text{easy}} \cdot \hat{\mathbf{m}}) \cdot \mathbf{e}_{\text{easy}}.\end{aligned}\quad (\text{D.29})$$

D.2.3 Demagnetization field

Within a homogeneous magnetized particle the demagnetization field $\mathbf{H}_{\text{demag}}$ can be written as

$$\mathbf{H}_{\text{demag}} = -N(\mathbf{r})\mathbf{M} = -\sum_j N_{ij}(\mathbf{r})M_j, \quad (\text{D.30})$$

with the spatial dependent 3×3 tensor $N(\mathbf{r})$, which is fully defined by the geometry of the considered volume. Since the demagnetization tensor $N(\mathbf{r})$ is a fully symmetric tensor independent of the magnetization, Eq. D.15 yields

$$\begin{aligned}\mathbf{H}_{\text{demag}} &= -\frac{1}{\mu_0 M_S V_\sigma} \frac{\partial}{\partial \hat{\mathbf{m}}_\sigma} \left[\frac{\mu_0 M_S^2 V_\sigma}{2} \hat{\mathbf{m}}_\sigma^T \cdot \mathbf{N}_\sigma(\mathbf{r}) \cdot \hat{\mathbf{m}}_\sigma \right] \\ &= -\frac{M_S}{2} \frac{\partial}{\partial m_i} \sum_{kl} (m_k N_{kl}(\mathbf{r}) m_l) \\ &= -\frac{M_S}{2} \sum_{kl} (\delta_{ik} N_{kl}(\mathbf{r}) m_l + m_k N_{kl}(\mathbf{r}) \delta_{il}) \\ &= -\frac{M_S}{2} \left(\sum_l N_{il}(\mathbf{r}) m_l + \sum_k m_k N_{ki}(\mathbf{r}) \right) \\ &= -\frac{M_S}{2} \left(\sum_k N_{ik}(\mathbf{r}) m_k + \sum_k m_k N_{ki}(\mathbf{r}) \right) \\ &= -\sum_k N_{ik}(\mathbf{r}) M_k.\end{aligned}\quad (\text{D.31})$$

Summarized, the total effective magnetic field in both, continuous and discrete systems, reads as

$$\mathbf{H}_{\text{eff}} = \frac{2\mathcal{J}S^2c}{a\mu_0 M_S^2} \Delta \mathbf{M} + \frac{2K_1}{\mu_0 M_S^2} (\mathbf{e}_{\text{easy}} \cdot \mathbf{M}) \cdot \mathbf{e}_{\text{easy}} + \mathbf{H}_{\text{demag}} + \mathbf{H}_{\text{ext}}. \quad (\text{D.32})$$

From LLB to Fokker-Planck

The procedure to obtain the Fokker-Planck equation of the Landau-Lifshitz-Bloch equation (Eq. 5.1) is equivalent to that of Appendix B. We start with the multivariate Langevin equation

$$\frac{dm_i}{dt} = A_i(\mathbf{m}, t) + \sum_k B_{ik}(\mathbf{m}, t)\xi_k(t). \quad (\text{E.1})$$

where $\mathbf{m} = \frac{M}{M_0}$ is the reduced magnetization of the considered particle, with its saturation magnetization at zero temperature M_0 . As proposed by Evans et al. [74] the drift and diffusion terms are

$$\begin{aligned} A_i(\mathbf{m}, t) = & - \gamma' \mu_0 (\mathbf{m} \times \mathbf{H}_{\text{eff}}) - \frac{\alpha_{\perp} \gamma' \mu_0}{m^2} [\mathbf{m} \times (\mathbf{m} \times \mathbf{H}_{\text{eff}})] \\ & + \frac{\alpha_{\parallel} \gamma' \mu_0}{m^2} \mathbf{m} (\mathbf{m} \cdot \mathbf{H}_{\text{eff}}) \end{aligned} \quad (\text{E.2})$$

and

$$\begin{aligned} B_{ik}^{\parallel}(\mathbf{m}, t) & = \delta_{ik} \\ B_{ik}^{\perp}(\mathbf{m}, t) & = \alpha_{\perp} \gamma' \mu_0 \left(\delta_{ik} - \frac{m_i m_k}{m^2} \right), \end{aligned} \quad (\text{E.3})$$

with the reduced electron gyromagnetic ration $\gamma' = \frac{|\gamma_e|}{1+\lambda^2}$. Since there exist a transversal and a perpendicular contribution to the thermal field, we need two different diffusion terms $B_{ik}(\mathbf{m}, t)$. Inserting Eqs. E.2 and E.3 into the Langevin equation yields the desired LLB equation

$$\begin{aligned} \frac{d\mathbf{m}}{dt} = & - \gamma' \mu_0 (\mathbf{m} \times \mathbf{H}_{\text{eff}}) - \frac{\alpha_{\perp} \gamma' \mu_0}{m^2} \{ \mathbf{m} \times [\mathbf{m} \times (\mathbf{H}_{\text{eff}} + \boldsymbol{\xi}_{\perp})] \} \\ & + \frac{\alpha_{\parallel} \gamma' \mu_0}{m^2} \mathbf{m} (\mathbf{m} \cdot \mathbf{H}_{\text{eff}}) + \boldsymbol{\xi}_{\parallel}. \end{aligned} \quad (\text{E.4})$$

To obtain the FP equation we use the formulation of Eq. B.10, which was already derived in Appendix B as follows

$$\frac{\partial \rho}{\partial t} = - \sum_i \frac{\partial}{\partial m_i} \left[\left(A_i - D \sum_k B_{ik} \sum_j \frac{\partial B_{jk}}{\partial m_j} - D \sum_{jk} B_{ik} B_{jk} \frac{\partial}{\partial m_j} \right) \rho \right]. \quad (\text{E.5})$$

Since $B_{ik}(\mathbf{m}, t)$ consists of two components, we calculate the last two contributions on the right-hand side of Eq. E.5 separately and merge them afterwards.

E.1 Transversal part of the FP

The derivate $\sum_j \frac{\partial B_{jk}^\perp}{\partial m_j}$ yields

$$\begin{aligned} \sum_j \frac{\partial B_{jk}^\perp}{\partial m_j} &= \sum_j \frac{\partial}{\partial m_j} \left[\alpha_\perp \gamma' \mu_0 \left(\delta_{jk} - \frac{m_j m_k}{m_l m_l} \right) \right] \\ &= - \sum_j \alpha_\perp \gamma' \mu_0 \frac{(\delta_{jj} m_k + m_j \delta_{jk}) m^2 - 2 m_j m_k \delta_{jl} m_l}{m^4} \\ &= - \alpha_\perp \gamma' \mu_0 \frac{3 m_k + m_k - 2 m_k}{m^2} = - 2 \alpha_\perp \gamma' \mu_0 \frac{m_k}{m^2}. \end{aligned} \quad (\text{E.6})$$

Hence, the second term in Eq. E.5 vanishes

$$\begin{aligned} D_\perp \sum_k B_{ik}^\perp \sum_j \frac{\partial B_{jk}^\perp}{\partial m_j} &= - \sum_k 2 D_\perp \alpha_\perp^2 \gamma'^2 \mu_0^2 \left(\delta_{ik} - \frac{m_i m_k}{m^2} \right) \frac{m_k}{m^2} \\ &= - \sum_k \frac{2 D_\perp \alpha_\perp^2 \gamma'^2 \mu_0^2}{m^2} (\delta_{ik} m_k - m_i) = 0. \end{aligned} \quad (\text{E.7})$$

The sum in the third term on the right-hand side of Eq. E.5 contributes as follows

$$\begin{aligned} D_\perp \sum_{jk} B_{ik}^\perp B_{jk}^\perp \frac{\partial}{\partial m_j} &= \sum_{jk} D_\perp \alpha_\perp^2 \gamma'^2 \mu_0^2 \left(\delta_{ik} - \frac{m_i m_k}{m^2} \right) \left(\delta_{jk} - \frac{m_j m_k}{m^2} \right) \frac{\partial}{\partial m_j} \\ &= \sum_{jk} D_\perp \alpha_\perp^2 \gamma'^2 \mu_0^2 \left(\delta_{ik} \delta_{jk} - \frac{m_i m_k \delta_{jk}}{m^2} - \frac{m_j m_k \delta_{ik}}{m^2} + \frac{m_i m_j m_k m_k}{m^4} \right) \frac{\partial}{\partial m_j} \\ &= \sum_j D_\perp \alpha_\perp^2 \gamma'^2 \mu_0^2 \left(\delta_{ij} - \frac{m_i m_j}{m^2} \right) \frac{\partial}{\partial m_j} \\ &= - \frac{D_\perp \alpha_\perp^2 \gamma'^2 \mu_0^2}{m^2} \left[\mathbf{m} \times \left(\mathbf{m} \times \frac{\partial}{\partial \mathbf{m}} \right) \right]. \end{aligned} \quad (\text{E.8})$$

In the last step the properties of a double cross product are used according to Eq. B.6.

E.2 Longitudinal part of the FP

The manipulations to obtain the longitudinal part of the FP are trivial due to the simple form of B_{ik}^\parallel . Since $\frac{\partial}{\partial m_j} \delta_{jk} = 0$ the second term on the right-hand side of Eq. E.5 again

equals zero and the third term becomes

$$D_{\parallel} \sum_{jk} B_{ik}^{\parallel} B_{jk}^{\parallel} \frac{\partial}{\partial m_j} = D_{\parallel} \frac{\partial}{\partial \mathbf{m}}. \quad (\text{E.9})$$

After combining longitudinal and perpendicular parts the FP equation yields

$$\begin{aligned} \frac{\partial \rho}{\partial t} = -\frac{\partial}{\partial \mathbf{m}} \cdot \left\{ \left[\begin{aligned} & - \frac{\alpha_{\perp} \gamma' \mu_0}{m^2} \mathbf{m} \times (\mathbf{m} \times \mathbf{H}_{\text{eff}}) - \gamma' \mu_0 (\mathbf{m} \times \mathbf{H}_{\text{eff}}) \\ & + \frac{\alpha_{\parallel} \gamma' \mu_0}{m^2} \mathbf{m} (\mathbf{m} \cdot \mathbf{H}_{\text{eff}}) \\ & + \frac{D_{\perp} \alpha_{\perp}^2 \gamma'^2 \mu_0^2}{m^2} \mathbf{m} \times \left(\mathbf{m} \times \frac{\partial}{\partial \mathbf{m}} \right) - D_{\parallel} \frac{\partial}{\partial \mathbf{m}} \end{aligned} \right] \rho \right\}. \quad (\text{E.10}) \end{aligned}$$

Thermal field strength in the LLB

The derivation of the diffusion constants D_{\perp} and D_{\parallel} in the LLB equation is equivalent to the according derivation for the LLG equation presented in Appendix C. We start with the FP equation, which was obtained in Appendix E to

$$\frac{\partial \rho}{\partial t} = -\frac{\partial}{\partial \mathbf{m}} \cdot \left\{ \left[-\frac{\alpha_{\perp} \gamma' \mu_0}{m^2} \mathbf{m} \times (\mathbf{m} \times \mathbf{H}_{\text{eff}}) - \gamma' \mu_0 (\mathbf{m} \times \mathbf{H}_{\text{eff}}) + \frac{\alpha_{\parallel} \gamma' \mu_0}{m^2} \mathbf{m} (\mathbf{m} \cdot \mathbf{H}_{\text{eff}}) + \frac{D_{\perp} \alpha_{\perp}^2 \gamma'^2 \mu_0^2}{m^2} \mathbf{m} \times \left(\mathbf{m} \times \frac{\partial}{\partial \mathbf{m}} \right) - D_{\parallel} \frac{\partial}{\partial \mathbf{m}} \right] \rho \right\}. \quad (\text{F.1})$$

Then we use the relation

$$\frac{\partial \rho_0}{\partial \mathbf{m}} = -\beta \frac{\partial E_{\text{tot}}}{\partial \mathbf{m}} \rho_0 = -\beta (-\mu_0 v M_0 \mathbf{H}_{\text{eff}}) \rho_0 = \mu_0 \beta v M_0 \mathbf{H}_{\text{eff}} \rho_0, \quad (\text{F.2})$$

between the probability distribution in thermal equilibrium ρ_0 and the effective field \mathbf{H}_{eff} according to Eq. C.4. The second term on the right-hand side of Eq. F.1 vanishes (see Eq. C.5), and thus the FP equation yields after using Eq. F.2

$$\frac{\partial \rho_0}{\partial t} = -\frac{\partial}{\partial \mathbf{m}} \cdot \left\{ -\frac{\alpha_{\perp} \gamma'}{m^2} \frac{1}{\beta v M_0} \mathbf{m} \times \left(\mathbf{m} \times \frac{\partial \rho_0}{\partial \mathbf{m}} \right) + \frac{\alpha_{\parallel} \gamma'}{m^2} \frac{1}{\beta v M_0} \mathbf{m} \left(\mathbf{m} \cdot \frac{\partial \rho_0}{\partial \mathbf{m}} \right) + \frac{D_{\perp} \alpha_{\perp}^2 \gamma'^2 \mu_0^2}{m^2} \mathbf{m} \times \left(\mathbf{m} \times \frac{\partial \rho_0}{\partial \mathbf{m}} \right) - D_{\parallel} \frac{\partial \rho_0}{\partial \mathbf{m}} \right\}. \quad (\text{F.3})$$

In thermal equilibrium $\frac{\partial \rho_0}{\partial t} = 0$ is valid. Exploiting the identity

$$\mathbf{a} \times (\mathbf{b} \times \mathbf{c}) = \mathbf{b}(\mathbf{a} \cdot \mathbf{c}) - \mathbf{c}(\mathbf{a} \cdot \mathbf{b}) \quad (\text{F.4})$$

Eq. F.3 becomes

$$0 = -\frac{\partial}{\partial \mathbf{m}} \cdot \left\{ -\frac{\alpha_{\perp} \gamma'}{m^2} \frac{1}{\beta v M_0} \left[\mathbf{m} \left(\mathbf{m} \cdot \frac{\partial \rho_0}{\mathbf{m}} \right) - \frac{\partial \rho_0}{\mathbf{m}} m^2 \right] \right. \\ \left. + \frac{D_{\perp} \alpha_{\perp}^2 \gamma'^2 \mu_0^2}{m^2} \left[\mathbf{m} \left(\mathbf{m} \cdot \frac{\partial \rho_0}{\mathbf{m}} \right) - \frac{\partial \rho_0}{\mathbf{m}} m^2 \right] \right. \\ \left. + \frac{\alpha_{\parallel} \gamma'}{m^2} \frac{1}{\beta v M_0} \mathbf{m} \left(\mathbf{m} \cdot \frac{\partial \rho_0}{\mathbf{m}} \right) - D_{\parallel} \frac{\partial \rho_0}{\partial \mathbf{m}} \right\}. \quad (\text{F.5})$$

The above equation is just solvable if

$$0 = \left(-\frac{\alpha_{\perp} \gamma'}{m^2 \beta v M_0} + \frac{D_{\perp} \alpha_{\perp}^2 \gamma'^2 \mu_0^2}{m^2} + \frac{\alpha_{\parallel} \gamma'}{m^2 \beta v M_0} \right) \mathbf{m} \left(\mathbf{m} \cdot \frac{\partial \rho_0}{\mathbf{m}} \right) \\ + \left(\frac{\alpha_{\perp} \gamma'}{\beta v M_0} - D_{\perp} \alpha_{\perp}^2 \gamma'^2 \mu_0^2 - D_{\parallel} \right) \frac{\partial \rho_0}{\mathbf{m}} \quad (\text{F.6})$$

holds. Thus, by equating coefficients we obtain the final expressions to determine the diffusion constants as follows

$$\alpha_{\parallel} - \alpha_{\perp} + D_{\perp} \alpha_{\perp}^2 \gamma'^2 \mu_0^2 \beta v M_0 = 0 \quad (\text{F.7})$$

$$\frac{\alpha_{\perp} \gamma'}{\beta v M_0} - D_{\perp} \alpha_{\perp}^2 \gamma'^2 \mu_0^2 - D_{\parallel} = 0. \quad (\text{F.8})$$

D_{\perp} and D_{\parallel} finally are

$$D_{\perp} = \frac{\alpha_{\perp} - \alpha_{\parallel}}{\alpha_{\perp}^2 \gamma'^2 \mu_0^2 \beta v M_0} = \frac{(\alpha_{\perp} - \alpha_{\parallel}) (1 + \lambda^2) k_B T}{\alpha_{\perp}^2 \gamma \mu_0^2 v M_0} \quad (\text{F.9})$$

$$D_{\parallel} = \frac{\alpha_{\parallel} \gamma'}{\beta v M_0} = \frac{\alpha_{\parallel} \gamma k_B T}{v M_0 (1 + \lambda^2)}. \quad (\text{F.10})$$

Bibliography

- [1] H. Risken, *The Fokker-Planck equation: methods of solution and applications*. Berlin: Springer, 2nd ed., 1989.
- [2] N. G. van Kampen, *Stochastic processes in physics and chemistry*. Amsterdam: North-Holland, 2nd ed., 1997.
- [3] H. S. Wio, R. R. Deza, and J. M. López, *An introduction to stochastic processes and nonequilibrium statistical physics*. Singapore: World Scientific, 2012.
- [4] P. E. Kloeden and E. Platen, *Numerical solution of stochastic differential equations*. Berlin: Springer, 2nd ed., 1995.
- [5] W. Horsthemke and R. Lefever, *Noise-induced transitions: theory and applications in physics, chemistry and biology*. Berlin: Springer, 1984.
- [6] W. Scholz, T. Schrefl, and J. Fidler, "Micromagnetic simulation of thermally activated switching in fine particles," *J. Magn. Magn. Mater.*, vol. 233, pp. 296–304, Aug. 2001.
- [7] H. Eyring, "The Activated Complex in Chemical Reactions," *J. Chem. Phys.*, vol. 3, pp. 107–115, Feb. 1935.
- [8] M. G. Evans and M. Polanyi, "Some applications of the transition state method to the calculation of reaction velocities, especially in solution," *Trans. Faraday Soc.*, vol. 31, pp. 875–894, Jan. 1935.
- [9] E. Wigner, "The transition state method," *Trans. Faraday Soc.*, vol. 34, pp. 29–41, Jan. 1938.
- [10] P. Hanggi, "Escape from a metastable state," *J. Stat. Phys.*, vol. 42, pp. 105–148, Jan. 1986.
- [11] D. Chandler, *Introduction to Modern Statistical Mechanics*. Oxford: Oxford University Press, 1987.

- [12] H. A. Kramers, "Brownian motion in a field of force and the diffusion model of chemical reactions," *Physica*, vol. 7, pp. 284–304, Apr. 1940.
- [13] P. Hänggi, P. Talkner, and M. Borkovec, "Reaction-rate theory: fifty years after Kramers," *Rev. Mod. Phys.*, vol. 62, pp. 251–341, Apr. 1990.
- [14] V. I. Mel'nikov and S. V. Meshkov, "Theory of activated rate processes: Exact solution of the Kramers problem," *J. Chem. Phys.*, vol. 85, pp. 1018–1027, July 1986.
- [15] P. M. Morse and H. Feshbach, *Methods of Theoretical Physics, Part I*. New York: McGraw-Hill, 1953.
- [16] H. Grabert, "Escape from a Metastable Well: The Kramers Turnover Problem," *Phys. Rev. Lett.*, vol. 61, pp. 1683–1686, Oct. 1988.
- [17] E. Pollak, H. Grabert, and P. Hänggi, "Theory of activated rate processes for arbitrary frequency dependent friction: Solution of the turnover problem," *J. Chem. Phys.*, vol. 91, pp. 4073–4087, Oct. 1989.
- [18] W. F. Brown, "Thermal Fluctuations of a Single-Domain Particle," *Phys. Rev.*, vol. 130, pp. 1677–1686, June 1963.
- [19] W. J. Brown, "Thermal fluctuation of fine ferromagnetic particles," *IEEE Trans. Magn.*, vol. 15, pp. 1196–1208, Sept. 1979.
- [20] D. A. Smith and F. A. De Rozario, "A classical theory of superparamagnetic relaxation," *J. Magn. Magn. Mater.*, vol. 3, pp. 219–233, Sept. 1976.
- [21] I. Klik and L. Gunther, "First-passage-time approach to overbarrier relaxation of magnetization," *J. Stat. Phys.*, vol. 60, pp. 473–484, Aug. 1990.
- [22] W. T. Coffey, D. A. Garanin, and D. J. McCarthy, "Crossover formulas in the kramers theory of thermally activated escape rates—application to spin systems," *Adv. Chem. Phys.*, pp. 483–765, 2001.
- [23] P. M. Déjardin, D. S. F. Crothers, W. T. Coffey, and D. J. McCarthy, "Interpolation formula between very low and intermediate-to-high damping Kramers escape rates for single-domain ferromagnetic particles," *Phys. Rev. E*, vol. 63, p. 021102, Jan. 2001.
- [24] Y. P. Kalmykov, "The relaxation time of the magnetization of uniaxial single-domain ferromagnetic particles in the presence of a uniform magnetic field," *J. Appl. Phys.*, vol. 96, pp. 1138–1145, July 2004.

- [25] W. T. Coffey and Y. P. Kalmykov, "Thermal fluctuations of magnetic nanoparticles: Fifty years after Brown," *J. Appl. Phys.*, vol. 112, p. 121301, Dec. 2012.
- [26] C. Vogler, F. Bruckner, B. Bergmair, T. Huber, D. Suess, and C. Dellago, "Simulating rare switching events of magnetic nanostructures with forward flux sampling," *Phys. Rev. B*, vol. 88, p. 134409, Oct. 2013.
- [27] C. Vogler, F. Bruckner, D. Suess, and C. Dellago, "Calculating thermal stability and attempt frequency of advanced recording structures without free parameters," *arXiv:1412.5057v1 [cond-mat, physics:physics]*, Dec. 2014. arXiv: 1412.5057.
- [28] T. Kawahara, K. Ito, R. Takemura, and H. Ohno, "Spin-transfer torque RAM technology: Review and prospect," *Microelectron. Reliab.*, vol. 52, pp. 613–627, Apr. 2012.
- [29] G. Hrkac, T. G. Woodcock, C. Freeman, A. Goncharov, J. Dean, T. Schrefl, and O. Gutfleisch, "The role of local anisotropy profiles at grain boundaries on the coercivity of Nd₂Fe₁₄B magnets," *Appl. Phys. Lett.*, vol. 97, p. 232511, Dec. 2010.
- [30] D. Suess, L. Breth, J. Lee, M. Fuger, C. Vogler, F. Bruckner, B. Bergmair, T. Huber, J. Fidler, and T. Schrefl, "Calculation of coercivity of magnetic nanostructures at finite temperatures," *Phys. Rev. B*, vol. 84, p. 224421, Dec. 2011.
- [31] H.-B. Braun, "Kramers's rate theory, broken symmetries, and magnetization reversal (invited)," *J. Appl. Phys.*, vol. 76, pp. 6310–6315, Nov. 1994.
- [32] P. N. Loxley and R. L. Stamps, "Theory for nucleation at an interface and magnetization reversal of a two-layer nanowire," *Phys. Rev. B*, vol. 73, p. 024420, Jan. 2006.
- [33] P. B. Visscher and R. Zhu, "Low-dimensionality energy landscapes: Magnetic switching mechanisms and rates," *Physica B*, vol. 407, pp. 1340–1344, May 2012.
- [34] G. Henkelman, B. P. Uberuaga, and H. Jónsson, "A climbing image nudged elastic band method for finding saddle points and minimum energy paths," *J. Chem. Phys.*, vol. 113, pp. 9901–9904, Dec. 2000.
- [35] W. E, W. Ren, and E. Vanden-Eijnden, "String method for the study of rare events," *Phys. Rev. B*, vol. 66, p. 052301, Aug. 2002.
- [36] R. Dittrich, T. Schrefl, D. Suess, W. Scholz, H. Forster, and J. Fidler, "A path method for finding energy barriers and minimum energy paths in complex micromagnetic systems," *J. Magn. Magn. Mater.*, vol. 250, pp. 12–19, Sept. 2002.

- [37] E. Paz, F. Garcia-Sanchez, and O. Chubykalo-Fesenko, "Numerical evaluation of energy barriers in nano-sized magnetic elements with Lagrange multiplier technique," *Physica B*, vol. 403, pp. 330–333, Feb. 2008.
- [38] G. Fiedler, J. Fidler, J. Lee, T. Schrefl, R. L. Stamps, H. B. Braun, and D. Suess, "Direct calculation of the attempt frequency of magnetic structures using the finite element method," *J. Appl. Phys.*, vol. 111, p. 093917, May 2012.
- [39] J. L. García-Palacios and F. J. Lázaro, "Langevin-dynamics study of the dynamical properties of small magnetic particles," *Phys. Rev. B*, vol. 58, pp. 14937–14958, Dec. 1998.
- [40] E. D. Boerner and H. Bertram, "Dynamics of thermally activated reversal in nonuniformly magnetized single particles," *IEEE Trans. Magn.*, vol. 33, pp. 3052–3054, Sept. 1997.
- [41] A. F. Voter, "Hyperdynamics: Accelerated Molecular Dynamics of Infrequent Events," *Phys. Rev. Lett.*, vol. 78, pp. 3908–3911, May 1997.
- [42] J. Xue and R. H. Victora, "Micromagnetic predictions for thermally assisted reversal over long time scales," *J. Appl. Phys.*, vol. 77, pp. 3432–3434, Nov. 2000.
- [43] S. Wang and P. Visscher, "Accelerated LLG Simulation of Magnetic Stability: 'Bounce' Algorithm," *IEEE Trans. Magn.*, vol. 43, pp. 2893–2895, June 2007.
- [44] R. J. Allen, P. B. Warren, and P. R. ten Wolde, "Sampling Rare Switching Events in Biochemical Networks," *Phys. Rev. Lett.*, vol. 94, p. 018104, Jan. 2005.
- [45] R. J. Allen, D. Frenkel, and P. R. t. Wolde, "Simulating rare events in equilibrium or nonequilibrium stochastic systems," *J. Chem. Phys.*, vol. 124, p. 024102, Jan. 2006.
- [46] C. Dellago, P. G. Bolhuis, F. S. Csajka, and D. Chandler, "Transition path sampling and the calculation of rate constants," *J. Chem. Phys.*, vol. 108, pp. 1964–1977, Feb. 1998.
- [47] P. G. Bolhuis, D. Chandler, C. Dellago, and P. L. Geissler, "TRANSITION PATH SAMPLING: Throwing Ropes Over Rough Mountain Passes, in the Dark," *Annu. Rev. Phys. Chem.*, vol. 53, no. 1, pp. 291–318, 2002.
- [48] T. S. v. Erp, D. Moroni, and P. G. Bolhuis, "A novel path sampling method for the calculation of rate constants," *J. Chem. Phys.*, vol. 118, pp. 7762–7774, May 2003.

- [49] V. Tsiantos, T. Schrefl, W. Scholz, H. Forster, D. Suess, R. Dittrich, and J. Fidler, "Thermally activated magnetization rotation in small nanoparticles," *IEEE Trans. Magn.*, vol. 39, pp. 2507–2509, Sept. 2003.
- [50] R. J. Allen, D. Frenkel, and P. R. t. Wolde, "Forward flux sampling-type schemes for simulating rare events: Efficiency analysis," *J. Chem. Phys.*, vol. 124, p. 194111, May 2006.
- [51] E. E. Borrero and F. A. Escobedo, "Optimizing the sampling and staging for simulations of rare events via forward flux sampling schemes," *J. Chem. Phys.*, vol. 129, p. 024115, July 2008.
- [52] D. Suess, "Multilayer exchange spring media for magnetic recording," *Appl. Phys. Lett.*, vol. 89, p. 113105, Sept. 2006.
- [53] D. Suess, J. Fidler, G. Zimanyi, T. Schrefl, and P. Visscher, "Thermal stability of graded exchange spring media under the influence of external fields," *Appl. Phys. Lett.*, vol. 92, p. 173111, Apr. 2008.
- [54] A. Y. Dobin, "Attempt frequency of thermally activated non-coherent switching in nanomagnets," *52nd Annual Conference on Magnetism and Magnetic Materials (MMM)*, 2007.
- [55] C. Vogler, C. Abert, F. Bruckner, and D. Suess, "Landau-Lifshitz-Bloch equation for exchange-coupled grains," *Phys. Rev. B*, vol. 90, p. 214431, Dec. 2014.
- [56] R. Wood, "Future hard disk drive systems," *J. Magn. Magn. Mater.*, vol. 321, pp. 555–561, Mar. 2009.
- [57] M. N. Baibich, J. M. Broto, A. Fert, F. Nguyen Van Dau, F. Petroff, P. Etienne, G. Creuzet, A. Friederich, and J. Chazelas, "Giant Magnetoresistance of (001)Fe/(001)Cr Magnetic Superlattices," *Phys. Rev. Lett.*, vol. 61, pp. 2472–2475, Nov. 1988.
- [58] P. Gruenberg, "Magnetic field sensor with a thin ferromagnetic layer." Patent No. DE3820475, 16 June 1988.
- [59] S. Iwasaki and K. Ouchi, "Co-Cr recording films with perpendicular magnetic anisotropy," *IEEE Trans. Magn.*, vol. 14, pp. 849–851, Sept. 1978.
- [60] S. Iwasaki, "Perpendicular magnetic recording," *IEEE Trans. Magn.*, vol. 16, pp. 71–76, Jan. 1980.

- [61] L. Mayer, "Curie-Point Writing on Magnetic Films," *J. Appl. Phys.*, vol. 29, pp. 1003–1003, June 1958.
- [62] C. Mee and G. Fan, "A proposed beam-addressable memory," *IEEE Trans. Magn.*, vol. 3, pp. 72–76, Mar. 1967.
- [63] J. E. Guisinger and G. W. Lewicki, "Thermomagnetic Recording and Magneto-Optic Playback System." Patent No. US3626114, 10 March 1969.
- [64] H. Kobayashi, M. Tanaka, H. Machida, T. Yano, and U. M. Hwang, "Method and Device for Vertical Thermomagnetic Recording." Patent No. JPS57113402, 5 January 1981.
- [65] R. Rottmayer, S. Batra, D. Buechel, W. Challener, J. Hohlfeld, Y. Kubota, L. Li, B. Lu, C. Mihalcea, K. Mountfield, K. Pelhos, C. Peng, T. Rausch, M. A. Seigler, D. Weller, and X. Yang, "Heat-Assisted Magnetic Recording," *IEEE Trans. Magn.*, vol. 42, pp. 2417–2421, Oct. 2006.
- [66] D. Suess and T. Schrefl, "Breaking the thermally induced write error in heat assisted recording by using low and high T_c materials," *Appl. Phys. Lett.*, vol. 102, p. 162405, Apr. 2013.
- [67] D. A. Garanin, "Fokker-Planck and Landau-Lifshitz-Bloch equations for classical ferromagnets," *Phys. Rev. B*, vol. 55, pp. 3050–3057, Feb. 1997.
- [68] D. A. Garanin and O. Chubykalo-Fesenko, "Thermal fluctuations and longitudinal relaxation of single-domain magnetic particles at elevated temperatures," *Phys. Rev. B*, vol. 70, p. 212409, Dec. 2004.
- [69] O. Chubykalo-Fesenko, U. Nowak, R. W. Chantrell, and D. Garanin, "Dynamic approach for micromagnetics close to the Curie temperature," *Phys. Rev. B*, vol. 74, p. 094436, Sept. 2006.
- [70] U. Atxitia, O. Chubykalo-Fesenko, N. Kazantseva, D. Hinzke, U. Nowak, and R. W. Chantrell, "Micromagnetic modeling of laser-induced magnetization dynamics using the Landau-Lifshitz-Bloch equation," *Appl. Phys. Lett.*, vol. 91, p. 232507, Dec. 2007.
- [71] N. Kazantseva, D. Hinzke, U. Nowak, R. W. Chantrell, U. Atxitia, and O. Chubykalo-Fesenko, "Towards multiscale modeling of magnetic materials: Simulations of FePt," *Phys. Rev. B*, vol. 77, p. 184428, May 2008.

- [72] C. Schieback, D. Hinzke, M. Kläui, U. Nowak, and P. Nielaba, "Temperature dependence of the current-induced domain wall motion from a modified Landau-Lifshitz-Bloch equation," *Phys. Rev. B*, vol. 80, p. 214403, Dec. 2009.
- [73] C. Bunce, J. Wu, G. Ju, B. Lu, D. Hinzke, N. Kazantseva, U. Nowak, and R. W. Chantrell, "Laser-induced magnetization switching in films with perpendicular anisotropy: A comparison between measurements and a multi-macrospin model," *Phys. Rev. B*, vol. 81, p. 174428, May 2010.
- [74] R. F. L. Evans, D. Hinzke, U. Atxitia, U. Nowak, R. W. Chantrell, and O. Chubykalo-Fesenko, "Stochastic form of the Landau-Lifshitz-Bloch equation," *Phys. Rev. B*, vol. 85, p. 014433, Jan. 2012.
- [75] T. W. McDaniel, "Application of Landau-Lifshitz-Bloch dynamics to grain switching in heat-assisted magnetic recording," *J. Appl. Phys.*, vol. 112, p. 013914, July 2012.
- [76] S. Greaves, Y. Kanai, and H. Muraoka, "Magnetization switching in energy assisted recording," *IEEE Trans. Magn.*, vol. 48, pp. 1794–1800, May 2012.
- [77] J. Mendil, P. C. Nieves, O. Chubykalo-Fesenko, J. Walowski, M. Münzenberg, T. Santos, and S. Pisana, "Speed limit of FePt spin dynamics on femtosecond timescales," *arXiv:1306.3112 [cond-mat.mtrl-sci]*, 2013. arXiv: 1306.3112.
- [78] R. F. L. Evans, W. J. Fan, P. Chureemart, T. A. Ostler, M. O. A. Ellis, and R. W. Chantrell, "Atomistic spin model simulations of magnetic nanomaterials," *J. Phys.: Condens. Matter*, vol. 26, p. 103202, Mar. 2014.
- [79] D. Hinzke, N. Kazantseva, U. Nowak, O. N. Mryasov, P. Asselin, and R. W. Chantrell, "Domain wall properties of FePt: From Bloch to linear walls," *Phys. Rev. B*, vol. 77, p. 094407, Mar. 2008.
- [80] U. Atxitia, D. Hinzke, O. Chubykalo-Fesenko, U. Nowak, H. Kachkachi, O. N. Mryasov, R. F. Evans, and R. W. Chantrell, "Multiscale modeling of magnetic materials: Temperature dependence of the exchange stiffness," *Phys. Rev. B*, vol. 82, p. 134440, Oct. 2010.
- [81] W. Bailey, P. Kabos, F. Mancoff, and S. Russek, "Control of magnetization dynamics in Ni₈₁Fe₁₉ thin films through the use of rare-earth dopants," *IEEE Trans. Magn.*, vol. 37, pp. 1749–1754, July 2001.

- [82] H. J. Richter, A. Lyberatos, U. Nowak, R. F. L. Evans, and R. W. Chantrell, "The thermodynamic limits of magnetic recording," *J. Appl. Phys.*, vol. 111, p. 033909, Feb. 2012.
- [83] N. B. Becker, R. J. Allen, and P. R. t. Wolde, "Non-stationary forward flux sampling," *J. Phys. Chem.*, vol. 136, p. 174118, May 2012.
- [84] N. B. Becker and P. R. t. Wolde, "Rare switching events in non-stationary systems," *J. Chem. Phys.*, vol. 136, p. 174119, May 2012.

Acknowledgements

In favor of a more accurate expression of my thanks this section is written in German.

An vorderster Stelle möchte ich meinem Betreuer Dieter Süss danken, der während der Jahre der Zusammenarbeit nicht nur Mentor, sondern vor allem ein Freund war, der jederzeit ein offenes Ohr für mich hatte und der immer eine Quelle an Ideen und Inspiration war.

Ebenso wichtig für die Motivation und das Durchhaltevermögen, die notwendig waren um meine Dissertation erfolgreich abschließen zu können, waren auch alle meine Kollegen und Freunde, die mich an schlechten Tagen mit den richtigen Worten und Ratschlägen wieder aufgebaut haben und die mit mir an guten Tagen gefeiert haben. Da jeder in seiner eigenen Art und Weise wichtig für mich war und gleichermaßen zu meinem Erfolg beigetragen hat, möchte ich mich in alphabetischer Reihenfolge herzlichst bedanken: Vielen Dank Claas, Corinna, Bernhard, Florian, Hannes, Hansjörg, Lukas, Markus, Raphael, Roman und Thomas.

Einen speziellen Dank möchte ich natürlich auch meinen Eltern aussprechen, auf deren bedingungslose Unterstützung ich mich zu jedem Zeitpunkt verlassen konnte, sowohl in finanzieller Hinsicht, aber auch und vor allem in moralischer und sozialer Hinsicht. Vielen Dank dafür!

Zu guter Letzt möchte ich meiner großen Liebe Anja danken. Es würde den Rahmen sprengen auf alle Einzelheiten einzugehen, wofür ich ihr zu Dank verpflichtet bin, aber die wichtigsten Punkte möchte ich dennoch explizit anführen. Ich danke dir dafür, dass du mich zu einem besseren Menschen machst und mir das Gefühl gibst am richtigen Fleck zu sein. Du bist einfach die zweite Hälfte meines Kugelmenschen!

This dissertation was funded by the WWTF project MA09-029 and the FWF project SFB ViCoM, F4112-N13. The computational results presented have been achieved using the Vienna Scientific Cluster (VSC).

List of Publications

2014

- C. Vogler, F. Bruckner, D. Suess and C. Dellago, “Calculating thermal stability and attempt frequency of advanced recording structures without free parameters”, submitted for publication in *Journal of Applied Physics*, manuscript published in *arXiv:1412.5057v1 [physics.comp-ph]*.
- C. Vogler, C. Abert, F. Bruckner and D. Suess, “Landau-Lifshitz-Bloch equation for exchange-coupled grains”, *Physical Review B* **90**, 214431.
- C. Abert, F. Bruckner, C. Vogler, R. Windl, R. Thanhoffer and D. Suess “A full-fledged micromagnetic code in less than 70 lines of NumPy”, *arXiv:1411.7188v2 [physics.comp-ph]*.
- D. Suess, C. Vogler, C. Abert, F. Bruckner, R. Windl and L. Breth “Fundamental limits in heat assisted magnetic recording and methods to overcome it with exchange spring structures”, *arXiv:1411.3052v1 [cond-mat.mes-hall]*.
- C. Abert, M. Ruggeri, F. Bruckner, C. Vogler, G. Hrkac, D. Praetorius and D. Suess “Self-consistent micromagnetic simulations including spin-diffusion effects”, *arXiv:1410.6067v1 [physics.comp-ph]*.
- T. Huber, B. Bergmair, C. Vogler, F. Bruckner, L. Breth, W. Hetaba, G. Hrkac and D. Suess, “Ultra-Low-Cost RFID Based on Soft Magnetic Ribbons”, *IEEE Transactions on Magnetics* **50**, 4004905.
- B. Bergmair, T. Huber, F. Bruckner, C. Vogler, M. Fuger and D. Suess, “Fully coupled, dynamic model of a magnetostrictive amorphous ribbon and its validation”, *Journal of Applied Physics* **115**, 023905.

2013

- C. Vogler, F. Bruckner, B. Bergmair, T. Huber, D. Suess, and C. Dellago, “Simulating rare switching events of magnetic nanostructures with forward flux sampling”, *Physical Review B* **88**, 134409.
- F. Bruckner, C. Vogler, B. Bergmair, T. Huber, M. Fuger, D. Suess, M. Feischl, T. Fuehrer, M. Page and D. Praetorius, “Combining micromagnetism and magnetostatic Maxwell equations for multiscale magnetic simulations”, *Journal of Magnetism and Magnetic Materials* **343**, 163.

2012

- B. Bergmair, T. Huber, F. Bruckner, C. Vogler and D. Suess, “Removal of earth’s magnetic field effect on magnetoelastic resonance sensors by an antisymmetric bias field”, *Sensors and Actuators A: Physical* **183**, 11.
- T. Huber, B. Bergmair, C- Vogler, F. Bruckner, G. Hrkac and D. Suess, “Magnetoelastic resonance sensor for remote strain measurements”, *Applied Physics Letters* **101**, 042402.
- L. Breth, D. Suess, C. Vogler, B. Bergmair, M. Fuger, R. Heer, and H. Brueckl, “Thermal switching field distribution of a single domain particle for field-dependent attempt frequency”, *Journal of Applied Physics* **112**, 023903.
- F. Bruckner, C. Vogler, M. Feischl, D. Praetorius, B. Bergmair, T. Huber, M. Fuger, and D. Suess, “3D FEM–BEM-coupling method to solve magnetostatic Maxwell equations”, *Journal of Magnetism and Magnetic Materials* **324**, 1862.

2011

- D. Suess, L. Breth, J. Lee, M. Fuger, C. Vogler, F. Bruckner, B. Bergmair, T. Huber, J. Fidler and T. Schrel, “Calculation of coercivity of magnetic nanostructures at finite temperatures”, *Physical Review B* **84**, 224421.
- L. Breth, D. Suess, C. Vogler, B. Bergmair, M. Fuger, R. Heer and H. Brueckl, “Fundamental switching field distribution of a single domain particle derived from the Néel-Brown model”, *arXiv:1110.6883v1 [cond-mat.mes-hall]*.

- C. Vogler, F. Bruckner, M. Fuger, B. Bergmair, T. Huber, J. Fidler and D. Suess, "Three-dimensional magneto-resistive random access memory devices based on resonant spin-polarized alternating currents", *Journal of Applied Physics* **109**, 123901.

Curriculum Vitae

Name: Christoph VOGLER
Date of birth: 09.04.1985 in Gmünd NÖ, Austria
Nationality: Austria

Education

2011 – 2015 Vienna University of Technology, Austria
Doktoratsstudium der technischen Wissenschaften
(Doctoral Program in Engineering Sciences)

2004 – 2010 Vienna University of Technology, Austria
Technische Physik, Dipl.-Ing.
(Physics, M.Sc.)
Thesis: *Spin Transfer Torque Switching*

1999 – 2003 Senior High School: Bundesrealgymnasium Gmünd NÖ

1995 – 1999 Junior High School: Bundesrealgymnasium Gmünd NÖ

1991 – 1995 Elementary School: Volksschule Gmünd NÖ

Wer aufhört, besser zu werden, hat aufgehört, gut zu sein.

Philip Rosenthal